

UNIVERSITY OF CRETE
Department of Materials Science and Technology

FOUNDATION FOR RESEARCH AND TECHNOLOGY
Institute of Electronic Structure and Lasers



“Direct Laser Writing of 3D photonic structures with tunable optical properties”

A DISSERTATION
*submitted in partial fulfillment of
the requirements for the degree of
DOCTOR OF PHILOSOPHY*

by

Kampouraki Asimina-Eleni

July 2019

Abstract

DLW by multiphoton polymerization (MPP) has become a powerful tool for the fabrication of fully three-dimensional micro- and nano-structures for microfluidic, biomedical, metamaterial, and photonic applications. In DLW, the beam of an ultrafast laser is tightly focused into the volume of a photosensitive material, initiating multiphoton polymerization within the focused beam volume (namely, voxel). By moving the focus of the beam in the three-dimensions, arbitrary 3D, high-resolution structures can be written into the volume of the material. By simply immersing the sample in an appropriate solvent, the non-polymerized area can be dissolved, revealing the 3D structure.

The materials developed in this work are photostructurable organic-inorganic hybrid materials, prepared using the sol-gel process. This versatile technique has been exploited for the incorporation of inorganic networks into polymer matrices, using as monomers molecules that carry an inorganic part (which serves as the precursor to the inorganic network) and a polymerizable organic group (which acts as the precursor to the organic polymer). For the fabrication of 3D structures by DLW, it is often necessary to add a photoinitiator, that is a molecule which, upon multiphoton absorption, generates the active species which initiate the polymerization process.

In this work, we present for the first time the fabrication of excellent quality 3D structures by photoinitiator-free multiphoton polymerization. The process relies on the synthesis of a novel vanadium-based hybrid material, containing vanadium (V) triisopropoxide oxide, which self-generates radicals via a light-induced redox reaction. In particular, upon multiphoton absorption the composite generate radicals by the photoinduced reduction of vanadium (V) to vanadium (IV). We exploit this material for the fabrication of fully 3D structures by multiphoton polymerization with 200 nm resolution, employing a femtosecond laser operating at 800 nm, in the absence of a photoinitiator. Nonlinear absorption measurements indicate that the use of a 800 nm laser initiates the photopolymerization due to a three-photon absorption of the vanadium alkoxide. The laser power required to induce this three-photon process is comparable to that required for inducing two-photon polymerization in materials using standard two-photon absorbers, most likely due to the high content of vanadium in the final composite (up to 50% mole).

In the second part of the present study hybrid organic-inorganic materials were modified by the addition of a quantum dot precursor molecule, which becomes chemically attached onto the fabricated 3D structures during the photo-polymerization process. Next, the 3D structures are reacted with sodium sulfide (Na_2S) to form CdS quantum dots within the structures. Such semiconductor nanoparticles enrich the fabricated structures with third order non-linear properties. 3D printed active photonic devices, of a woodpile geometry with an inlayer periodicity as low as 500 nm, are successfully fabricated at high resolution and exhibit clear photonic stop bands in the visible spectral region, while for the first time, evidence of ultrafast dynamic tuning of the photonic band gap properties in the visible, is also demonstrated.

In the final part of this thesis, pre-synthesized highly fluorescent CdSe-CdS quantum dots, bearing appropriate functionalities, were permanently bound onto the surface of 3D photonic crystal structures, following chemical functionalization of the surface of the particles or the surface of the 3D structures. Woodpile 3D photonic crystal structures, with an inlayer periodicity of 550 nm, were fabricated, using the Direct Laser Writing technique, exhibiting photonic stopgaps at visible wavelengths. Next, the structures were coated with the synthesized quantum dots that can act as a gain medium. Near the band edge of these gaps, the group velocity, v_g , of photons localized in the structure, approaches zero and photons undergoing multiple reflections in the lattice experience longer interaction with the gain material, thus resulting in an enhanced effective gain. By matching the photoluminescence of the nanoparticles with the bandedges of the photonic crystals a functional device that can act as a nanolaser was developed.

Abbreviations & Notations

m	meters
mm	Milimeters = 10^{-3} m
μm	Micrometers = 10^{-6} m
nm	Nanometers = 10^{-9} m
s	second
fs	Femtosecond = 10^{-15} s
K	Kelvin
CdSe	Cadmium Selenide
CdTe	Cadmium Telluride
ZnSe	Zinc Selenide
ZnS	Zinc Sulfide
CdS	Cadmium Sulfide
InP	Indium Phosphide
MPP	Multiphoton polymerization
TPA	Two-photon absorption
UV	Ultraviolet
1D	One dimensional
2D	Two dimensional
3D	Three dimensional
2PP	Two-photon polymerization
QDs	Quantum dots
NCs	Nanocrystals
E_g	Energy bandgap
α_B	Exciton Bohr radius
FIB	Focused ion beam
MBE	Molecular beam epitaxy
QY	Quantum yield
CS	Core-shell
FWHM	Full width half maximum
PC	Photonic crystal
FCC	Face centered cubic
VUV	Vacuum ultraviolet
TE	Transverse electric
TM	Transverse magnetic

Table of Contents

Preface.....	11
CHAPTER 1: Theoretical Background.....	15
1.1 Sol-Gel.....	16
1.1.1 Hydrolysis	17
1.1.2 Condensation	21
1.2 Multi-photon polymerization.....	24
1.2.1 Two photon absorption.....	24
1.2.2 Mechanism of Two Photon Polymerization	25
1.2.3 Applications of 2-Photon Polymerization	27
1.3 Quantum Dots.....	29
1.3.1 How quantum dots work	29
1.3.2 Synthesis of quantum dots.....	32
1.3.3 Optical properties of quantum dots	36
1.4 Photonic crystals.....	43
1.4.1 Basic concepts	44
1.4.2 1D photonic crystals: Photonic bandgaps and photonic bandstructure	47
1.4.3 2D photonic crystals.....	49
1.4.4 3D photonic crystals.....	53
1.4.5 Applications of photonic crystals.....	58
CHAPTER 2: Redox Multiphoton Polymerization for 3D Nanofabrication	61
2.1 Introduction	61
2.2 Materials and methods.....	62
2.2.1 Material Synthesis	62
2.2.3 Sample preparation.....	65
2.2.4 Characterization of the vanadium composite material	65
2.2.5 3D Structure fabrication	69

2.3	Results and Discussion	70
2.4	Conclusions	77
	CHAPTER 3: Active three-dimensional woodpile photonic crystal structures tuned for the visible light	79
3.1	Introduction	79
3.2	Experimental.....	81
3.2.1	Material synthesis.....	81
3.2.2	Sample preparation.....	84
3.2.3	Characterization of the CdS quantum dot hybrid material and the 3D structures .	85
3.2.4	3D Microfabrication.....	87
3.2.5	Theoretical Calculations.....	87
3.3	Results and discussion.....	88
3.4	Conclusions.....	102
	CHAPTER 4: 3D photonic structures for photonic crystal lasing applications	105
4.1	Introduction	105
4.2	Experimental.....	107
4.2.1	Material synthesis.....	107
4.2.2	Sample preparation.....	111
4.2.3	Fabrication of the 3D photonic structures	113
4.2.4	Characterization of the CdSe-CdS Quantum Dots and the 3D structures	114
4.3	Results and discussion.....	115
4.4	Conclusions	132
	Conclusions and future perspectives	133
	References	137
	Aknowledgements.....	153

Preface

Shaping matter from the atomic scale to the macroscopic level – in the three dimensions – has been attracting great scientific and technological interest for many decades. While bottom-up self-assembly approaches have long been expected to eventually surpass top-down lithography, the latter remains dominant in many important areas such as computer-chip or photonic-circuitry fabrication. Abbe's famous resolution formula states that the achievable resolution in far-field optical lithography, as well as in microscopy, is proportional to the wavelength of the (light) wave used. This has led to ultraviolet (UV), deep UV (DUV) or even extreme UV (EUV) planar optical lithography that are used in today's and tomorrow's computer-chip fabrication lines, respectively. The corresponding mask masters are fabricated using electron-beam lithography, which takes advantage of the yet smaller de Broglie wavelength of accelerated electrons. In principle, optical near-field effects can overcome Abbe's barrier in lithography.

While interesting demonstrations have been published indeed, such approaches do have fundamental limitations in that the near-field-writing head inherently needs to be in close proximity to the photoresist to be exposed. Moreover, these approaches are intrinsically limited to the surface, i.e., to planar lithography. The beauty of far-field optics is that it also allows for three-dimensional (3D) lithography, often referred to as 3D direct laser writing (3D DLW). In 3D DLW, a (pulsed) laser is tightly focused to a diffraction-limited spot within the volume of a thick-film photoresist. By exploiting two-photon absorption and/or other nonlinearities (e.g., brought about by the photoresist itself), the effectively exposed volume can be restricted to the focal region leading to a volume element, the "voxel", in analogy to the picture element commonly referred to as pixel.

The technique originated from nonlinear microscopy, providing 3D confined recording inside UV-sensitive polymers. Now it is emerging as the most precise and true 3D printing technology in both scientific and industrial fields. Three-dimensional (3D) laser structuring of materials is widely used in photopolymer prototyping applications including micro-optical elements, parts of optically actuated micromachines in microfluidics, scaffolds for cell growth, templates for plasmonic and metamaterials, and photonic crystals (PhCs).

The scope of the current thesis is the exploitation of DLW, by the multiphoton polymerization technique, for the development and fabrication of 3D photonic crystal devices for applications in photonics. Although, DLW comprises one of the most powerful techniques in the 3D realization of complex microstructures of any given shape, the fabrication of such exotic structures are out of the scope of this thesis. The current work is focused mostly on the development of new materials that are applied to this technique. This thesis aims to prove that tuning the chemistry, by means of synthesizing new materials, and/or modifying/functionalizing existing ones, can lead in the realization of devices with totally different characteristics and properties for use in various applications. We will present the synthesis of a new material which can be structured accurately by DLW, without the addition of a photoinitiator, via three-photon absorption, and the modification of an existing material to introduce Kerr nonlinearity in the fabricated 3D structures. Finally, we will functionalize 3D photonic crystals with a gain medium via the chemical binding of an emitting material.

The fabricated structures by DLW were in all cases woodpile photonic crystals formed from materials with new functionalities. The optical properties of the novel materials and the fabricated structures will be studied for the development of 3D photonic systems.

This PhD thesis is organized as follows:

In Chapter 1 we will introduce the theoretical background involved in this work. The sol-gel technique employed to fabricate ceramic networks within the hybrid photosensitive materials is discussed, the principles of multi-photon polymerization will be analyzed, the theory of quantum dots, the active material used in the 3D structures, is explained and finally, a short introduction on photonic crystals is given.

Chapter 2 is the experimental part, describing the synthesis of novel organic–inorganic composite materials, incorporating a vanadium metallo-organic complex, initiates the polymerization, bypassing the need of photoinitiator addition. The initiation process is based on a redox reaction, leading to a redox multi-photon polymerization, which is presented for the first time in literature.

Chapter 3 describes the fabrication of active 3D printed photonic devices by combining Direct Laser Writing (DLW) with two-photon absorption, and the in situ synthesis of the cadmium sulfide (CdS) nanoparticles within the 3D polymeric matrix. We will see how these nanoparticles alter the optical properties of the material by inducing an intensity dependent refractive index which was measured using the z-

scantechnique. Moreover, the novel active 3D photonic structures that were fabricated are characterized by time-resolved pump-probe spectroscopy, where evidence of the dynamic response of these structures are presented.

Finally, in chapter 4 the fabrication of 3D photonic devices functionalized with a gain material is reported. The under consideration structure is a 3D photonic crystal following the woodpile geometry with inlayer periodicity of 550 nm, while the gain medium consists of CdSe-CdS core-shell QDs. We will meet the synthetic route followed for the synthesis of the gain medium and its optical characterization in terms of absorption, photoluminescence and emission efficiency. Next, altering the surface chemistry of these particles led to their successful immobilization on the surface of the 3D structures leading to the fabrication of a device that could act as a nanolaser.

CHAPTER 1: Theoretical Background

In this Chapter, a short introduction is given, on the theoretical background of the synthetic and structuring techniques used throughout this thesis. Additionally, we introduce the basic principles of photonic crystals and quantum dots.

First, the *sol-gel* technique, used for the preparation of the hybrid photosensitive materials, is explained in terms of its definition and the materials used. The two basic reactions, hydrolysis and condensation, are explained and the influence of the pH and the presence of catalysts on the reaction rate and the products obtained are explained.

Next, we will discuss the principles of multi-photon polymerization, one of most versatile techniques for the fabrication of 3D structures. The theory of the simplest case, two-photon absorption, is explained along with the mechanisms of two-photon polymerization. The section finally concludes with the applications of multi-photon polymerization spanning from photonics to tissue engineering.

In the following section we discuss the theory of quantum dots, the active material of the devices fabricated during this thesis. The definition and characteristics of the nanoparticles are given as well as the synthetic approaches employed for their synthesis, followed by their exotic optical properties which involve the size dependent photoluminescence and intensity dependent refractive index.

Finally, the chapter concludes with a brief introduction on photonic crystals. Basic concepts, such as the characteristics of these periodic structures and the propagation of the electromagnetic radiation through their lattice are discussed. The simplest case, 1D photonic crystals, is explained along with the origin of bandgaps and bandstructures, followed by higher dimensions 2D and 3D photonic crystals and the effect of increasing dimensionality on the bandgaps and bandstructures. The chapter will conclude with some photonic crystal applications.

1.1 Sol-Gel

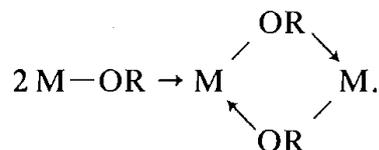
Sol-gel is the process involved in the preparation of ceramic materials (or organically modified materials) by which a sol undergoes gelation to form a gel. The sol comprises inorganic or hybrid precursor molecules which in the initial steps, before gelation, can form loose or dense oxide or hybrid particles and clusters.

As the name implies, the *sol-gel* process involves the evolution of a *sol* via gelation to form an inorganic network. The *sol* is a colloidal suspension of solid particles in a liquid. In this *colloid* system gravitational forces are negligible and interparticle interactions are dominated by short-range forces, such as van der Waals attractions and electrostatic repulsion.

The precursor molecules employed to synthesize these colloids comprise a metal or metalloid element surrounded by appropriate reactive ligands. Common precursors include inorganic salts e.g. $\text{Al}(\text{NO}_3)_3$ and metal alkoxides such as $\text{Al}(\text{OC}_4\text{H}_9)_3$, widely used in sol-gel research. Metal alkoxides are members of the family of metalorganic compounds which possess an organic ligand attached to a metal or metalloid atom. They are commonly confused with the organometallic compounds which are defined as having direct metal-carbon bonds, not metal-oxygen-carbon (M-O-R) linkages as in metal alkoxides. Thus metal alkoxides are not organometallic compounds, although this term is frequently used in the literature.

Transition metal alkoxides (MOR) are very popular precursors because they react readily with water. In general metal alkoxides are very reactive due to the presence of highly electronegative OR groups (hard- π donors) that stabilize the metal (M) in its highest oxidation state and render M very susceptible to nucleophilic attack. The lower electronegativity of the transition metals causes them to be more electrophilic and thus less stable towards hydrolysis, condensation and other nucleophilic reactions. Transition metals often exhibit several stable coordination numbers, and when coordinatively unsaturated, they are able to expand their coordination number via *ol*ation, *ox*olation, alkoxy bridging, or other nucleophilic association mechanisms. *O*lation is a condensation process in which a hydroxy bridge (“*ol*” bridge) is formed between two metal centers. *Ox*olation is a condensation reaction in which an oxo bridge (-O-) is formed between two metal centers. When metal alkoxides are dissolved in non-

polar solvents, they form oligomers via alkoxy bridging, a nucleophilic addition (A_N) mechanism similar to olation :



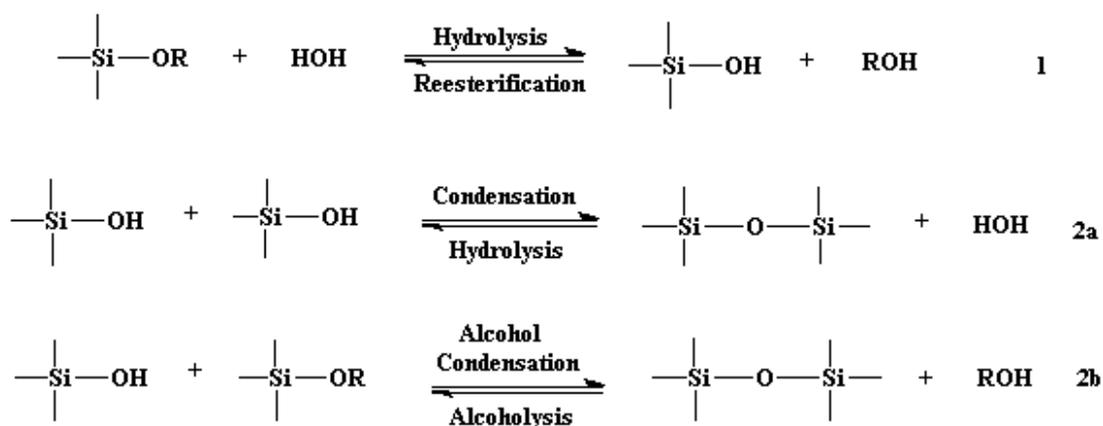
The generally rapid kinetics of the nucleophilic reactions has attracted fundamental studies on the hydrolysis and condensation of transition metal alkoxides.

Generally the sol-gel process involves two main reactions:

1. Hydrolysis and
2. Condensation

However, the characteristics and properties of every particular sol-gel inorganic network are related to a number of factors that affect the rate of hydrolysis and condensation reactions, such as, pH, temperature and time of reaction, reagent concentrations, catalyst nature and concentration, aging temperature and time, and the drying process. Of the factors listed above, pH, the nature and concentration of the catalyst and the temperature have been identified as the most important.

The general reaction scheme can be seen in below [1]



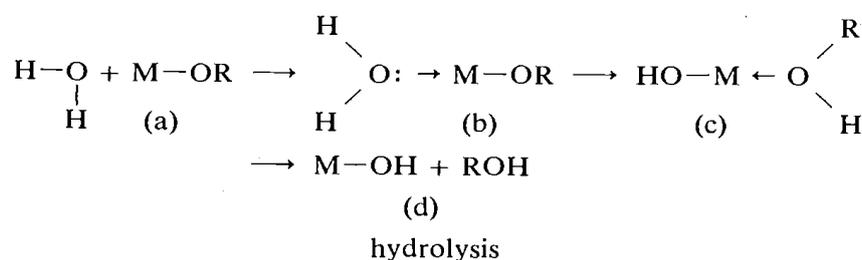
1.1.1 Hydrolysis

The reaction is called hydrolysis, because a hydroxyl ion becomes attached to the metal atom as in the following reaction:



where, R represents an alkyl group and ROH is an alcohol. For coordinatively saturated metals in the absence of catalyst, hydrolysis and condensation, both occur by nucleophilic substitution (S_N) mechanisms. Nucleophilic substitution is a fundamental class of substitution reactions in which an “electron rich” nucleophile selectively bonds with or attacks the positive or partially positive charge of an atom attached to a group or an atom called the leaving group or atom. There are two main mechanisms, the S_{N1} reaction and the S_{N2} reaction. S stands for chemical substitution, N stands for nucleophilic, and the number represents the kinetic order of the reaction. In the S_{N2} reaction, the addition of the nucleophile and the elimination of the leaving group take place simultaneously. S_{N2} occurs when the central atom is easily accessible to the nucleophile. By contrast the S_{N1} reaction involves two steps. S_{N1} reactions tend to be important when the central atom of the substrate is surrounded by bulky groups, because such groups interfere sterically with the S_{N2} reaction. The nucleophilic addition reaction is an addition reaction in which a nucleophile is added to, followed by the removal of the leaving group and the creation of two new covalent bonds.

The reaction taking place is shown below:



Depending on the amount of water and catalyst present, hydrolysis may go to completion, so that all of the OR groups are replaced by OH, or stop when the metal is only partially hydrolyzed, e.g. $\text{Si}(\text{OR})_{4-n}(\text{OH})_n$. The thermodynamics of hydrolysis, are governed by the strength of the entering nucleophile, the electrophilicity of the metal, and the partial charge and stability of the leaving group.

Solution pH

As mentioned above, hydrolysis is affected by the solution pH. The process is divided into three pH domains: below pH 2, pH 2-7 and above pH 7. However, regardless of the pH, hydrolysis occurs by the nucleophilic attack of the oxygen contained in water to the metal atom.

Figure 0.1 shows the effect of the pH on the hydrolysis rate.

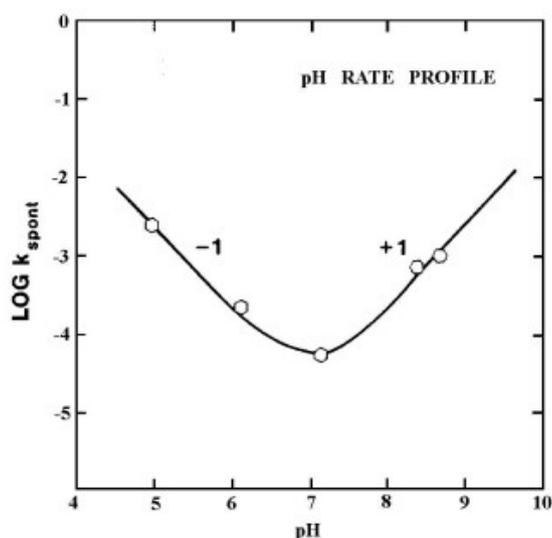


Figure 0.1. pH rate profile of the hydrolysis reaction

Role of the catalyst

Although hydrolysis can occur without the addition of an external catalyst, it is more rapid and complete when a catalyst employed. The nature of the catalyst may be acidic or basic. The most generally used catalysts are mineral acids (HCl) and ammonia. Some others are acetic acid, KOH, amines, KF, and HF. It has been observed that the rate and extent of the hydrolysis reaction is mostly influenced by the strength and concentration of the acidic or basic catalyst.

a. Acid-Catalyzed Mechanism

All strong acids behave similarly, although weaker acids require longer reaction times to achieve the same extent of reaction. Acids serve to protonate the negatively charged alkoxide groups, enhancing the reaction kinetics by producing good leaving groups, and eliminating the requirement for proton transfer within the transition state. Alkoxide groups are protonated in a rapid first step. In this way, the electron density is withdrawn from the metal atom, rendering it more electrophilic and thus more susceptible to attack by water. This results in the formation of a penta coordinate transition state with significant S_N2 type character as shown in figure 1. 2.

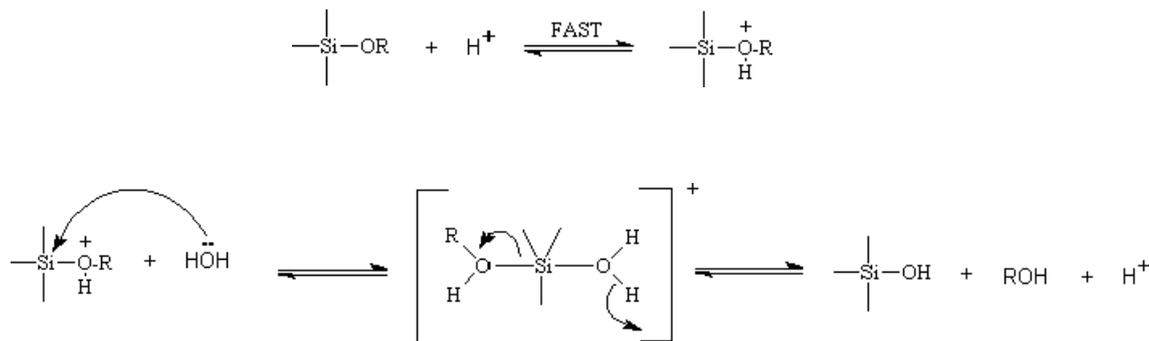
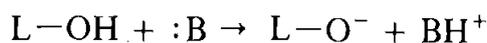


Figure 1.2. Acid-Catalyzed Hydrolysis

The hydrolysis goes to completion when sufficient water is added.

b. Base Catalyzed Mechanism

Base catalyzed hydrolysis proceeds much more slowly than the acid catalyzed process, at an equivalent catalyst concentration. Alkaline conditions produce strong nucleophiles via deprotonation of the hydroxo ligands:



where, L = M and B = OH⁻ or NH₃. Basic alkoxide oxygens tend to repel the nucleophile, OH⁻. However, once an initial hydrolysis has occurred, the following reactions proceed stepwise, with each subsequent alkoxide group removed more easily from the monomer than the previous one. Although hydrolysis in alkaline environments is slow, it still tends to be complete and irreversible. Thus, under these conditions it is more likely that water dissociates to produce hydroxyl ions in a rapid first step. The hydroxyl anion then attacks the metal atom. Again, an S_N2 nucleophilic reaction has been proposed in which the hydroxyl group displaces the -OR group, as seen in figure 1.3.

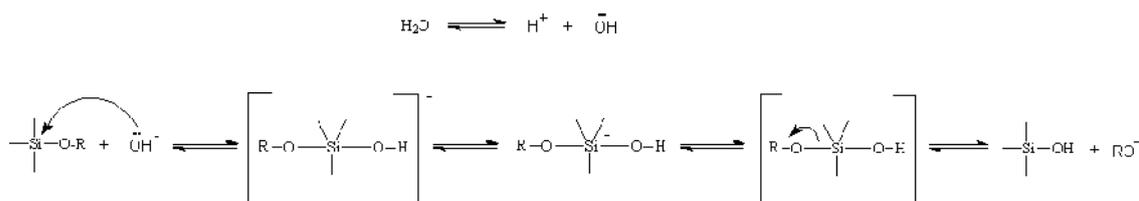
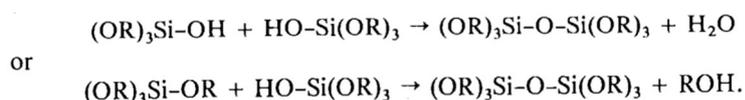


Figure 1.3. Base-Catalyzed Hydrolysis

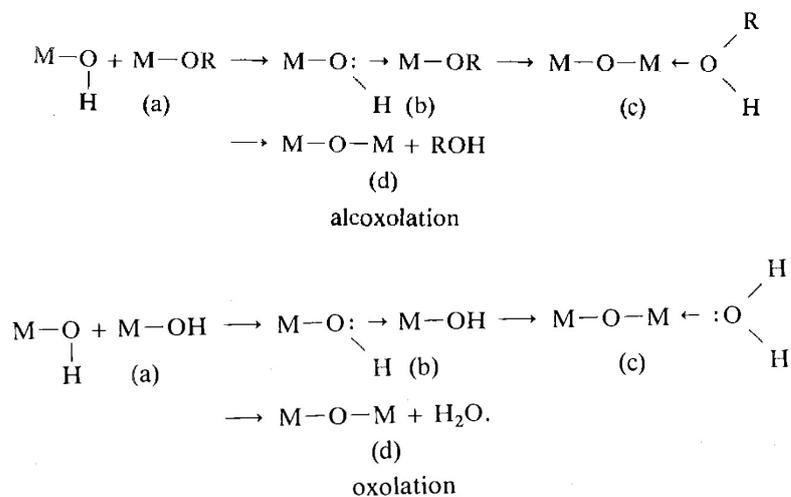
1.1.2 Condensation

Two partially hydrolyzed molecules are linked together, in a process called condensation reaction. By definition, condensation liberates a small molecule, such as water or alcohol:

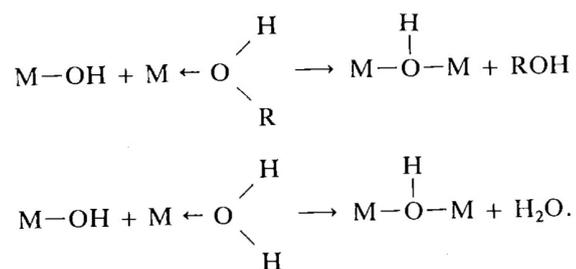


This type of reaction can continue to build larger and larger metal containing molecules. As the number of metal bonds increases, the individual molecules are bridged and jointly aggregate in the sol. When the sol particles aggregate, or inter-knit into a network, a gel is formed. Upon drying, trapped volatiles, such as water, alcohol etc, are driven off and the network shrinks as further condensation can occur.

More specifically, during condensation, nucleophilic mechanisms such as S_N and A_N take place, followed by proton transfer from the attacking molecule to an alkoxide or hydroxo-ligand within the transition state and removal of the protonated species as either alcohol (alcoxolation) or water (oxolation):



There is also a possibility that condensation can occur by olation:



The thermodynamics of alkoxolation, oxolation and ololation depend on the same factors mentioned above for the hydrolysis reaction, among which are: the strength of the entering nucleophile and the electrophilicity of the metal.

Under most conditions, condensation commences before hydrolysis is complete. However, conditions such as, pH and catalyst can force completion of hydrolysis before condensation begins.

Solution pH

When condensation takes place at pH below 2, the rates are proportional to the $[H^+]$ concentration. It is generally agreed that between pH 2 and 6 condensation rates are proportional to $[OH^-]$ concentration. Condensation preferentially occurs between more highly condensed species and those less highly condensed. This suggests that the rate of dimerization is low, however, once dimers form, they react preferentially with monomers to form trimers, which in turn react with monomers to form tetramers. Above pH 7, condensation occurs as in the pH 2 to 6 range. However, at this pH range, condensed species are ionized and therefore, mutually repulsive. Growth occurs primarily through the addition of monomers to the more highly condensed particles rather than by particle aggregation. Growth stops when the difference in solubility between the smallest and the largest particles becomes indistinguishable. Additionally, in this pH range, the growth rate depends upon the particle size distribution. The dissolution rate and relative gel time as a function of pH can be seen in figure 1.4.

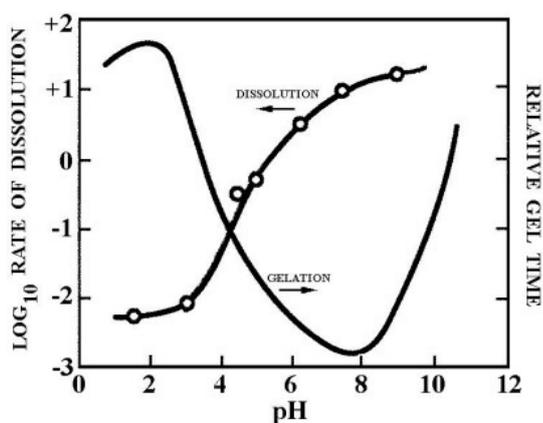


Figure 1.4. Dissolution rate and gel time as a function of pH

Role of the Catalyst

Similar to the hydrolysis reaction, condensation can proceed without catalyst, however its use accelerates the reaction. Furthermore, similar catalysts are employed for the two reactions: acidic or basic compounds. Acid or base catalysts can influence the condensation rate and the structure of the condensed product. It has been shown that condensation reactions are acid or base specific. In addition, under strongly basic conditions gel times have been shown to increase.

a. Acid-Catalyzed Mechanism

Acids serve to protonate negatively charged alkoxide groups. The relative ease of protonation of different alkoxide ligands can influence the condensation pathway. Acid-catalyzed condensation is directed preferentially toward the ends rather than the middle of the chains, resulting in more extended, less branched polymers. High acid concentrations severely retard the condensation kinetics.

b. Base-Catalyzed Mechanism

Condensation kinetics are systematically enhanced under basic conditions. The mechanism for the base-catalyzed condensation is shown below:



Base-catalyzed condensation, leads to more compact, highly branched species.

1.2 Multi-photon polymerization

Multi-photon polymerization (MPP) induced by a femtosecond laser, has emerged as a new microscale fabrication technology. In particular, MPP is a very attractive three dimensional rapid microstructuring technology. Photopolymerization refers to the process of using light as an energy source to induce the conversion of small unsaturated molecules to macromolecules through polymerization reactions [2]. MPP has many advantages as a technique for the fabrication of complex 3D structures on a scale of several microns, which are difficult to obtain using conventional miniaturization technologies. It is known that when a femtosecond laser pulse is focused into the volume of a photosensitive material, this pulse initiates two photon polymerization via a two photon absorption (TPA) process.

1.2.1 Two photon absorption

The simplest case of multi-photon absorption refers to two-photon absorption. The probability of n-photon absorption is proportional to the n^{th} power of the photon flux density. Thus, high photon flux densities are required in order to observe this phenomenon. These high intensities are only provided by a laser source. The general idea is that an atom can absorb two or more photons simultaneously, allowing electron transition to higher energy states.

The theory of two photon absorption (TPA) was first developed by Maria Coppert-Mayer in 1931 and was experimentally observed for the first time in 1961 with the invention of lasers. TPA is a multiple photon excitation approach used in the initiation of photochemical changes. Most photosensitive resins that polymerize under UV (λ) exposure can undergo similar reactions when two photons (2λ) are absorbed, provided that the light intensity is high enough.

Two mechanisms have been reported for TPA (see Figure 1.5) [3]:

- (a) stepwise excitation and
- (b) simultaneous two photon excitation

The former relies on the existence of a real intermediate state, from which an excited electron is further pumped to a higher energy level by absorbing photons of the same

energy as that at the ground state. Such a process is termed stepwise TPA. Compared to simultaneous TPA, stepwise TPA doesn't require coherence of the incident light, and can be considered as two sequential single photon absorption phenomena.

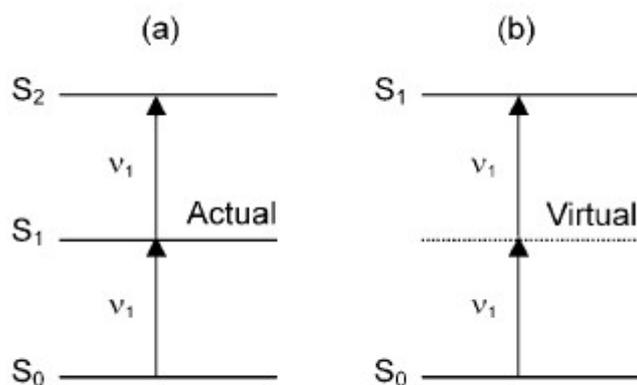


Figure 1.5. Mechanism of TPA

In simultaneous TPA, there is no real intermediate state, but a virtual intermediate state is created by the interaction of the absorbing species with the first photon. In this case, two photons each with half the energy of the gap between the two energy levels, induce the electron transition. Only if the second photon arrives within the virtual state lifetime, about 10^{-15} sec, can it be absorbed. Thus, it is apparent that higher intensities are required for the simultaneous TPA, which usually requires femtosecond lasers. For femtosecond laser micro-fabrication, simultaneous TPA is more relevant. For this reason, in the below any reference to TPA will refer to simultaneous TPA.

1.2.2 Mechanism of Two Photon Polymerization

TPA can be utilized for inducing photopolymerization. Two-photon polymerization was experimentally reported for the first time in 1965 by Pao and Rentzepis as the first example of multiphoton excitation-induced photochemical reactions. The difference between one photon and two photon polymerization lies in how the energy is provided. In single-photon polymerization, there is a linear response of the material to the light intensity. However, if the material response is proportional to the square of the photon density, the integrated material response is greatly enhanced at the focal point, as illustrated in figure 1.6 [4].

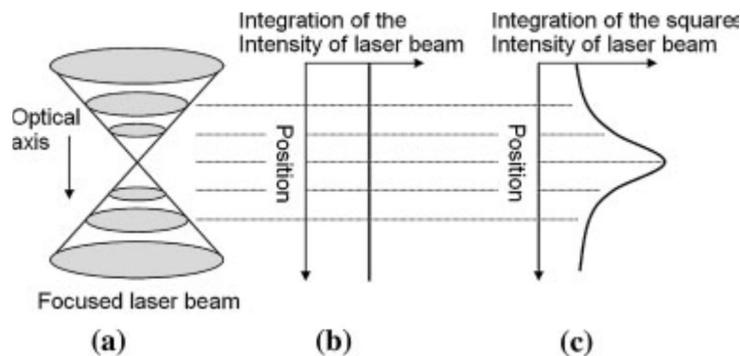


Figure 1.6. Comparison of TPA and two single-photon absorption generated by a tightly focused laser beam.

The two photon transition rate is extremely small, so a very high spatial resolution can be obtained (figure 1.7)

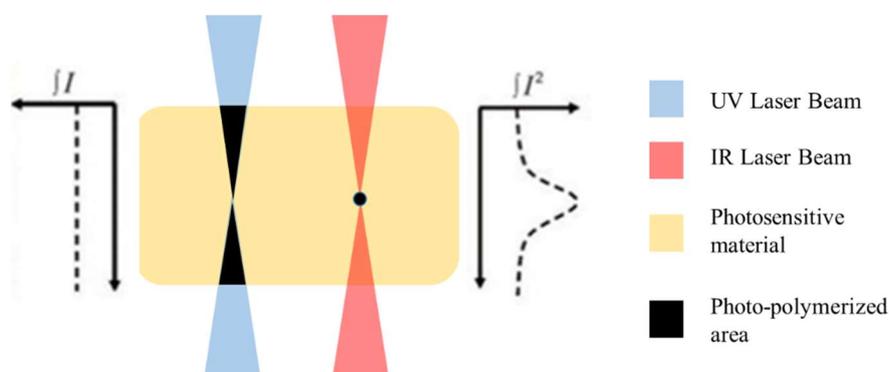


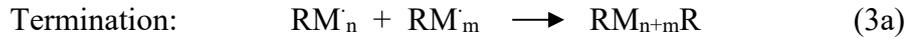
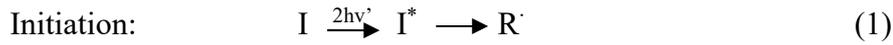
Figure 1.7. The laser beam in single-photon polymerization (left), and two photon polymerization (right)

The intensity distribution of the laser beam, which is assumed to be Gaussian (figure 1.6(c)), is expressed by the following equation:

$$I(r_0,0) = I_0 \exp(-2r_0^2/\omega_0^2)$$

where, r_0 , I_0 , and ω_0 are the radius of the beam, the beam intensity at the central axis in the focus plane, and the radius of the focused beam spot, respectively.

When a laser beam of high intensity is focused into the volume of a liquid photosensitive material that is transparent to NIR light, the photoinitiator that is used to enhance two photon activation is excited by the simultaneous absorption of two photons, and results in the generation of free radicals (initiation). This is the beginning of a free radical polymerization process. The radicals formed react with monomers, producing monomer radicals which participate in a chain reaction (propagation). This reaction will continue until the monomers are consumed, or until two growing radicals meet (termination). This procedure is depicted in the following scheme [5].



or



Where $\nu' \sim \nu/2$ denotes photon frequency in the two photon excitation beam, I is the initiator, R \cdot the free radical and M the monomer unit. I * represents an excited state of the photoinitiator after absorbing the photon energy, respectively.

The density of radicals (ρ) produced by femtosecond laser pulses in the polymerization process varies with the square of the beam intensity:

$$\partial\rho/\partial t = (\rho_0 - \rho) \delta I^2$$

where, δ is the effective two photon cross-section for the generation of radicals.

1.2.3 Applications of 2-Photon Polymerization

Despite the fact that 2PP is a relatively new technology its application fields have been rapidly expanding in the recent years. Because of the high optical quality that can be achieved with 2PP, many of the applications demonstrated to date have been in the field of photonics [6]. Photonic structures include waveguides, couplers, interferometers, microlenses and even microlasers [7], [8]. Apart from that, 2PP is also used for the fabrication of micromechanical systems, microfluidic devices, biomedical devices and scaffolds for tissue engineering [9], [10], [11].

Two Photon Polymerization is a novel technique for processing hybrid organic-inorganic materials. This innovative method for 3D structuring of structural and functional materials, using fs-pulsed NIR lasers, has distinct benefits. First of all, the achievable feature resolution of about 100 nm is about one order of magnitude better than other methods such as μ -stereolithography. Furthermore, due to the non-linear process it is possible to directly write inside a given volume (“real” 3D writing), since the polymerization only takes place in the focus of the laser beam. Therefore, complex 3D structures can be inscribed into a suitable matrix material and/or a resin which is selectively cured. These advantages perfectly fulfill the demands for various future applications requiring three dimensional structures with resolutions in the

(sub)micrometer range, such as different mechanical, electronic and optical micro-devices, polymer based optical waveguides on integrated circuit boards and bio-inspired architectures.

One of the first and most thoroughly studied applications of 2PP is the fabrication of 3D photonic crystals (see figure 1.8) [12]. A photonic crystal is an artificial structure exhibiting periodic variation of the dielectric constant of the material. Such a structure has a similar effect on the propagation of photons, as the periodic variation of electric potential in regular crystals on propagating electrons, hence the name photonic crystal.

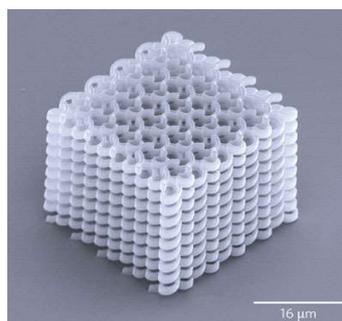


Figure 1.8. Spiral photonic crystal.

One of the most popular approaches of 2PP in tissue engineering is the fabrication of 3D scaffolds whose function is to guide and support cell proliferation in the three dimensions [13]. The ability to produce arbitrary 3D scaffolds is therefore very appealing. The 2PP technique can also be applied for the fabrication of implants and prostheses. The materials used for these purposes must demonstrate appropriate biological compatibility, stability and stiffness. The versatility of the 2PP technology and the large number of applicable materials have contributed to the wide range of applications of this technology which are rapidly growing.

Great interest has been focused recently to 3D micrometer-sized luminescent devices [14]. These devices can be fabricated by 2PP from semiconductor-polymer composites. The semiconductor nanoparticles in the materials show unique tunable light emission properties, arising from the quantum size effects.

1.3 Quantum Dots

The term “quantum dots” (QDs) refers to colloidal semiconductor crystals (NCs). These colloidal particles are composed by an inorganic core of a few tens to a few hundred atoms surrounded by an organic outer layer of surfactant molecules, the so called “ligands”. The fact that these particles are very small in size and are considered zero dimensional relative to the bulk, gives rise in an observable quantum confinement effect which is defined by an increasing bandgap accompanied by the quantization of the energy levels to discrete values. The fact that their optical properties are size-dependent, has attracted great research interest over the past few decades. Nevertheless, their nanometer size, results in a very high surface to volume ratio. Figure 1.9 [15] gives the band energies, of semiconductor nanocrystals, calculated according to ref. [16], which are most commonly used in QD synthesis.

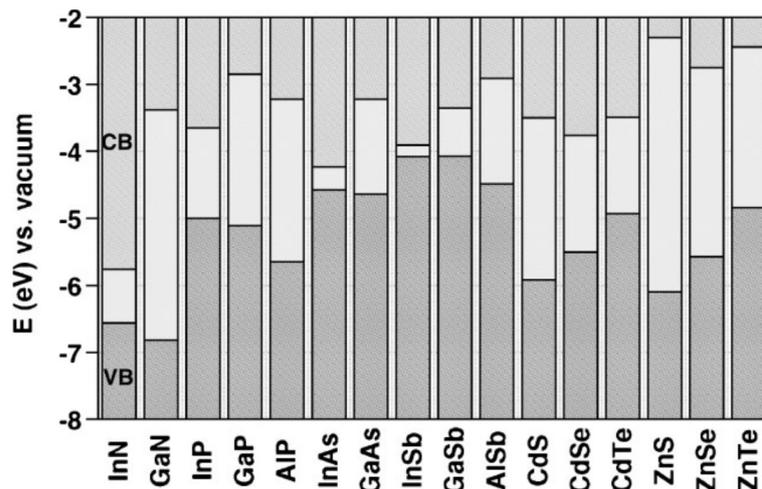


Figure 1.9. Electronic energy levels of selected III–V and II–VI semiconductors

1.3.1 How quantum dots work

In order to understand how quantum dots work, bulk semiconductors should be first understood. In bulk semiconductors the energy levels, that the electrons occupy, are very close to each other and they can be described as continuous. That means that there is almost no energy difference between them. There is also a region of forbidden electron energies that is called the energy bandgap (E_g). This energy bandgap is different for each bulk material. The energy levels below the bandgap are called valence bands and the energy levels above the bandgap are called conduction bands. Figure 1.10

shows the differences in energy levels between metals, semiconductors and insulators [17]. A very small amount of electrons occupy the conduction band and the majority of them occupy the valence band, filling it almost completely.

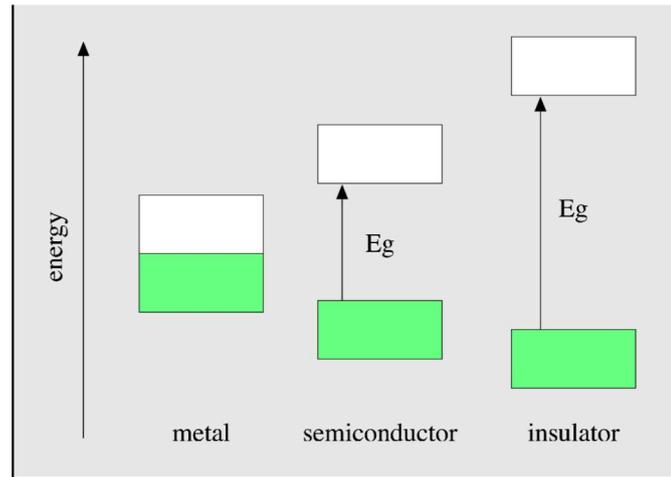


Figure 1.10. Simplified energy level diagram for metals, semiconductors and insulators at 0 K. The green boxes represent the valence band, which is fully occupied by electrons, while the white boxes represent the almost empty conduction band.

There is a possibility that an electron can jump to the conduction band, if it acquires enough energy to cross the band gap. This can be accomplished by applying a stimulus such as heat, voltage or photon flux. When an electron “jumps” to the conduction band, a vacation is created at the valence band. This vacation is referred as a hole, since it leaves a temporary “hole” in the valence band electron structure. This hole is positively charged due to the absence of the electron. The raised electron and the hole, taken as a pair are called an exciton. There is a physical separation between the electron and the hole, which is called exciton Bohr radius (α_B) and is described by the following equation [18] (SI units):

$$\alpha_B = 4\pi\epsilon_0 \frac{\epsilon \hbar^2}{\mu_{eh} e^2}$$

where, ϵ_0 is the dielectric permittivity of vacuum, ϵ the relative dielectric permittivity, \hbar the reduced Plank’s constant, μ_{eh} the electron-hole reduced effective mass and e the electron’s charge.

When an electron falls down across the bandgap to the valence band, electromagnetic radiation is emitted with wavelength that corresponds to the energy it loses. Because the energy bandgap of the bulk semiconductors is fixed, the emission frequencies of the

electron transitions are also fixed. Quantum dots offer the unnatural ability to tune the bandgap and as a result the emission wavelength [19]

In quantum dots, the electrons have a range of energies. This distance is different in each material. The dimensions of bulk semiconductors are much larger than the Exciton Bohr Radius. When the size of the quantum dots approaches the size of the Exciton Bohr Radius, then upon creation of the exciton, the physical dimensions of the particle confine the exciton in a manner similar to the particle-in-a-box problem of quantum mechanics. Therefore, quantum effects, such as quantization of energy levels, can be observed in principle. Alternatively, one can think of the nanoparticle as having an electronic structure intermediate between bands and bonds. One consequence of this intermediate character is that E_g is correlated with size: as the dimensions of the particle decrease, E_g increases (figure 1.11) [20].

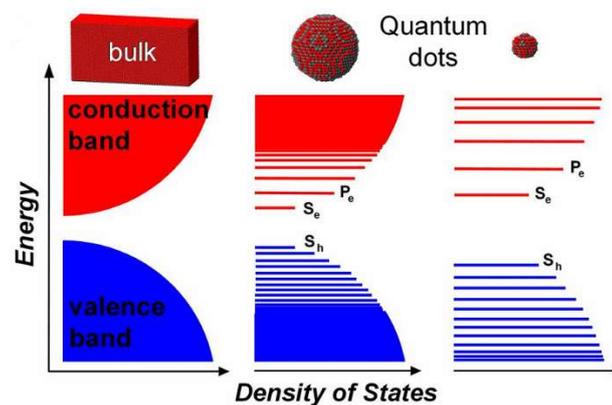


Figure 1.11. Energy level diagram of semiconductors from bulk material to quantum dots of different size.

This situation of discrete energy levels is called quantum confinement. The addition or subtraction of just a few atoms in the quantum dot can alter the boundaries of the bandgap. L.E Brus [21], [22] developed an effective mass model which relates the size with the E_g of semiconductor QDs. Brus's model makes a few approximations of the system:

1. The particle is spherical, with a radius R .
2. The interior of the particle is a uniform medium; there are no point charges or occupied spaces other than the excited electron and hole (i.e., nuclei or bound electrons).

3. The potential energy outside the nanocrystal is infinite; thus the electron and hole are always found within the nanocrystal (i.e., the surface of the nanocrystal defines the walls of a “box”).

Making these assumptions Brus concluded to the following equation:

$$E_g(\text{quantum dot}) = E_g(\text{bulk}) + \left(\frac{\hbar^2}{8R^2}\right) \left(\frac{1}{m_e} + \frac{1}{m_h}\right) - \frac{1,8e^2}{4\pi\epsilon_0\epsilon R}$$

where, where E_g is the bandgap energy of the quantum dot or bulk material, R is the radius of the quantum dot, m_e is the effective mass of the electron in the solid, m_h is the effective mass of the hole in the solid, and ϵ is the dielectric constant of the solid. The middle term on the right-hand side of the equation is a particle-in-a-box-like term for the exciton, while the third term on the right-hand side of the equation represents the electron–hole pair Coulombic attraction, mediated by the solid.

The Brus model correlates E_g with the size of the nanoparticle quite well for bigger particles, but its predictions do not match experiment well for very small particle sizes.

1.3.2 Synthesis of quantum dots

Since their discovery in glass matrices by Alexey Ekimov in 1981 [23] QDs have gained tremendous research interest. In the past years, several routes have been proposed to synthesize QDs. These involve two major approaches; the top-down and bottom-up.

In the top-down approaches, a bulk semiconductor is thinned to form the QDs. Electron beam lithography, reactive-ion etching and/or wet chemical etching are commonly used to achieve QDs of diameter ~ 30 nm. Controlled shapes and sizes with the desired packing geometries are achievable for systematic experiments on quantum confinement effect. Alternatively, focused ion or laser beams have also been used to fabricate arrays of zero-dimension dots. Major drawbacks with these processes include the incorporation of impurities into the QDs and structural imperfections by patterning. One precise top-down technique is the focused ion beam (FIB) which offers the possibility of fabricating QDs with extremely high lateral precision. Highly focused beams from a molten metal source (e.g., Ga, Au/Si, Au/Si/Be, or Pd/As/B) may be used

directly to sputter the surface of the semiconductor substrate. The shape, size and inter-particle distance of the QDs depend on the size of the ion beam, but a minimum beam diameter of 8–20 nm has been reported for both lab and commercial systems, allowing to etch the QDs to dimensions <100 nm [24]. However this is a slow, low throughput process employing expensive equipment that results in residual surface damage.

The bottom-up approaches involves a number of different self-assembly techniques, and they may be broadly subdivided into wet-chemical and vapor-phase methods. Microemulsion [25]–[27], sol-gel [28]–[30] and hot-solution decomposition [31], generally fall in the category of wet-chemical methods. Self-assembly of nanostructures in materials grown by molecular beam epitaxy (MBE) [32]–[36], sputtering [37], liquid metal ion sources, or aggregation of gaseous monomers [38] are generally categorized under vapor-phase methods.

Among the different bottom-up approaches, the most versatile and commonly used one is the hot solution method. In this scheme, that was first proposed by *Bawendi* and co-workers [31] in 1993, the main advantage is that it uses injection and growth temperature to control the QD particle size. To-date, the hot solution synthesis methods have been widely adopted to synthesize QDs, such as, CdSe, CdTe, ZnSe, ZnS and CdS. Additionally, the near infrared (NIR) QDs, such as, InP and other lead chalcogenides, have also been synthesized by pairing the colloidal method with hot injection [39], [40]. Precursors, such as alkyl [31], acetate [41], carbonate [41] and oxides [41], [42] of Group II elements, are mixed with Group VI phosphine or bis(trimethyl-silyl) precursors. A typical procedure involves first degassing and drying trioctyl-phosphine oxide (TOPO, a coordinating solvent) at 200–350 °C under vacuum in a three-neck round flask in a dry box. A mixture of Cd-precursor and tri-*n*-octyl-phosphine (TOP) selenide is prepared in a dry box and injected with vigorous stirring into the flask at a temperature of ~300 °C. The simultaneous injection of precursors into the flask, along with TOPO, results in homogeneous nucleation to form QDs upon subsequent growth through ‘*Ostwald ripening*’ being relatively slow. In *Ostwald ripening*, the higher free energy of smaller QDs makes them lose mass to large size QDs, eventually disappearing. The net result is a slow increase of the size of the QDs at the reaction temperature of ~230–250 °C (depending on precursor, coordinating agents and solvents). The coordinating TOPO solvent stabilizes the QD dispersion, improves the passivation of the surface, and provides an adsorption barrier to slow the growth of the QDs. The final size of the QDs is mainly controlled by the reaction time

and temperature. Aliquots may be removed from the flask at regular intervals during the first few hours, and the optical absorption edge can be used to achieve the desired particle size. This method has been extensively used to synthesize II-VI [43]–[46], IV-VI [47] and III-V QDs [48]. The size, shape, and control over the overall reaction depends not only on process parameters and precursors, solvents and coordinating agents, but also on the purity of the coordinating solvent, TOPO. It has been reported that technical grade TOPO (90% pure) is better for synthesizing uniform QDs than pure TOPO [41], [49]. An advantage of this synthesis route is that it provides sufficient thermal energy to anneal defects and results in monodispersed QDs (typically standard deviation about the average size of 5%). Since growth of the particles in this process is relatively slow and can be controlled by modulating the temperature, a series of QD sizes can be prepared from the same precursor bath. Using this process, large quantities of QDs [50] and alloying process [51] have been demonstrated. Some of the disadvantages of this method include higher costs, due to the use of high temperature, toxicity of some of the organometallic precursors, and generally poor dispersions in water.

QDs can also be synthesized using an aqueous route [52] but often end up with increased hydrodynamic radius (due to aggregation) and lower quantum yields (QYs) [53], [54] than QDs prepared by the colloidal routes. Typically, QD synthesis by the aqueous route involves the reflux of respective salts for longer durations, up to ~24h, and this enhances the tendency of aggregation [55]. Aggregation of QDs leads to a decrease in absorption intensity, red shift, peak broadening and a decreased PL [52]. However, researchers have improved the QY by capping the core, enabling a high QY in core-shell QDs [56]–[58].

Solvent is another major component to be considered in colloidal synthetic routes. Solvents, such as, n-octadecane and olive oil were used as the dissolution medium to avoid the formation of unsaturated compounds and to enhance reusability [59]. Polymers like poly(acrylic acid) and poly(hexyl thiophene) derivatives conferred stability and allowed for the controlled growth of QDs [60], [61]. Apart from this, the polarity of solvent used for the precipitation of the QDs or their purification also plays an important role in retaining the QD structure [62].

Likewise, certain physical parameters (i.e., temperature) can also influence the QD properties, such as, PL intensity [63].

By applying the above mentioned synthetic routes, nanometer-sized semiconductor cores of various chemical compositions can be realized. These cores are stabilized by organic ligands with an anchoring headgroup tethered to the NC surface and a hydrocarbon tail directed away from it. The set of ligands attached to a NC forms a ‘capping’ layer that saturates dangling bonds, screens the particle from its environment, and controls nucleation and growth kinetics during synthesis [64]. Nevertheless, a significant fraction of these organically passivated core NCs typically exhibit surface related trap states acting as fast non-radiative de-excitation channels for photogenerated charge carriers, thereby reducing the fluorescence QY. The most widely used route to improve NCs’ surface passivation is their overgrowth with a shell of a second semiconductor, resulting in core-shell (CS) systems. In this manner, the fluorescence efficiency and stability against photo-oxidation of various types of semiconductor NCs have been significantly improved. Furthermore, by the appropriate choice of the core and shell materials, it is possible to tune the emission wavelength in a larger spectral window than with both materials alone.

The shell is used to passivate the surface of the core with the goal to improve its optical properties. The shell of the NC physically separates the surface of the optically active core from its surrounding medium. Consequently, the sensitivity of the optical properties to changes in the local environment of the NCs’ surface, induced, for example, by the presence of oxygen or water molecules, is reduced. With respect to core NCs, core-shell systems exhibit generally enhanced stability against photodegradation. At the same time, shell growth reduces the number of surface dangling bonds, which can act as trap states for charge carriers and thereby reduce the fluorescence QY.

A general requirement for the synthesis of core-shell NCs, with satisfactory optical properties, is epitaxial-type shell growth. Therefore, an appropriate band alignment is not the sole criterion for the choice of materials, but rather the core and shell materials should crystallize in the same structure and exhibit a small lattice mismatch. In the opposite case, the growth of the shell results in strain and the formation of defect states at the core-shell interface or within the shell. These can act as trap states for photogenerated charge carriers and diminish the fluorescence QY [65].

The control of the shell thickness is a delicate point in the fabrication of core-shell NCs and deserves special attention. If the shell is too thin, the passivation of the core NCs is inefficient, resulting in reduced photostability. In the opposite case, the optical

properties of the resulting CS core-shell NCs generally deteriorate as a consequence of strain induced by the lattice mismatch of the core and shell materials, accompanied by the generation of defect states.

Core-shell nanocrystals are in most cases fabricated in a two-step procedure: initial synthesis of core particles, followed by a purification step, and the subsequent shell growth reaction. During this final step, a small number of monolayers (typically 1–5) of the shell material are deposited on the cores. In order to prevent nucleation of the shell material and uncontrolled ripening of the core NCs, the temperature for the shell growth is generally lower than the one used for the core NC synthesis. Furthermore, the shell precursors are slowly added, for example, by means of a syringe pump. A major advantage, over the so-called one-pot approach, without an intermediate purification step, is the fact that unreacted precursors or side products can be eliminated before the shell growth. The core NCs are purified by precipitation and redispersion cycles, and finally dissolved in the solvent used for the shell growth. In order to calculate the required amount of shell precursor to obtain the desired shell thickness, it is necessary to know the concentration of the core NCs.

One of the most commonly used techniques for the growth of the shell is the SILAR (successive ion layer adsorption and reaction) method [66]. It is based on the formation of one monolayer at a time by alternating the injections of cationic and anionic precursors.

1.3.3 Optical properties of quantum dots

QDs have gained great interest from the scientific community, because they exhibit very interesting optical properties. Unlike solid state crystals and small-molecule chromophores and fluorophores, quantum confined semiconductor structures exhibit unique optical properties dictated by their structure and size. After their excitation with an external stimulus, e.g., photon for photoluminescence, electric field for electroluminescence, primary electron for cathodoluminescence *etc.*, electron and hole possess high energies due to the transition of the electron from the valence band (ground state) to the conduction band (excited state). The energies associated with such optical absorptions are directly determined by the electronic structure of the material. The excited electron and hole may form an exciton, as discussed above. The electron may recombine with the hole and relax to a lower energy state, ultimately reaching the

ground state. The excess energy resulting from recombination and relaxation may be either radiative (emits photon) or non-radiative (emits phonons or *Auger* electrons). Radiative relaxation results in spontaneous luminescence from QDs. The most common radiative relaxation processes in intrinsic semiconductors and insulators are band-edge and near band-edge (exciton) emission. The recombination of an excited electron in the conduction band with a hole in the valence band is called band-edge emission. Radiative recombination of an exciton leads to near band-edge emission at energies slightly lower than the band-gap. The emission properties of semiconductor nanocrystals can be characterized by four fundamental parameters, which are the brightness, the emission color, the color purity, and the stability of the emission. Due to quantum size effects, the band gap of nanocrystal QDs increases as their size decreases, and thus the emission color of the band-edge PL of the nanocrystals shifts continuously from red to blue as the size of the nanocrystals decreases. Figure 1.12 depicts characteristic absorption and emission spectra from nanoparticle QDs. Since the emission color of semiconductor nanocrystals is strongly dependent on their size and shape, the color purity of the emission becomes dependent on the size and shape distribution of a nanocrystal sample.

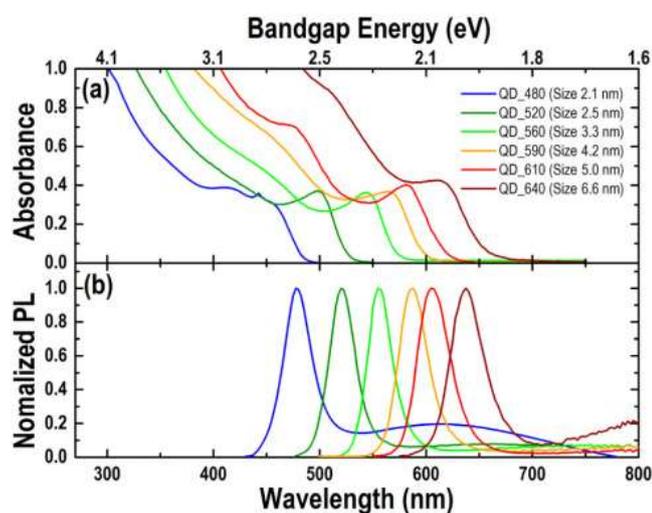


Figure 1.12. Absorption (a) and emission (b) spectra of a colloidal solution of CdSe QDs dispersed in toluene [67]

In essence, QDs may be tuned to emit light across the visible spectrum by changing their size. The narrow FWHM (full width at half maximum) of quantum dots can result in saturated color emission. The broadly tunable, saturated color emission over the

entire visible spectrum of a single material system is unmatched by any class of organic chromophores. QDs have a number of advantages over organic dyes such as, better photostability, wide absorption edges, and narrow, tunable emission.

Radiative emission from QDs also comes from localized impurity and/or activator quantum states in the band-gap. Defect states lie inside the bands themselves [68]. Depending on the type of defect or impurity, the state can act as a donor (has excess electrons) or an acceptor (has a deficit of electrons). Electrons or holes are attracted to these sites of deficient or excess local charge due to Coulombic attraction. Defect states are expected at the surface of a QD despite the use of various passivation methods, because of the large surface-to-volume ratio, discussed above. The concentration of surface states on the QDs is a function of the synthesis and passivation processes. These surface states act as traps for charge carriers and excitons, which generally degrade the optical and electrical properties by increasing the rate of non-radiative recombination. However, in some cases, the surface states can also lead to radiative transitions [69], [70].

Another very interesting property that QDs exhibit, is that of third order optical nonlinearity. There are two major categories that fall into this order of nonlinearity: frequency mixing (e.g. Third-Harmonic Generation) or intensity dependent refractive index [71]. The later provides a basis for all optical processing of information, which could result in tremendous gain in speed and is the subject of study in this thesis.

When light propagates through a medium, the applied electric field of light polarizes the molecules of the medium, displacing them from their equilibrium positions and induces a dipole moment μ_{ind} given by

$$\mu_{\text{ind}} = -er$$

where, e is the electronic charge and r is the field induced displacement. The polarization of the medium due to this induced dipole is given by

$$P = -Ner$$

where, N is the electron density in the medium. This polarization opposes the externally applied field and results to a lower electric field inside the material. The polarization is often expressed in terms of susceptibility $\chi^{(n)}$ as

$$P = \chi^{(1)} \cdot E + \chi^{(2)}:EE + \chi^{(3)}:EEE + \dots$$

or

$$P = \chi_{\text{eff}} E$$

The coefficient $\chi^{(1)}$ is the linear susceptibility whereas the coefficient $\chi^{(2)}$, relating the polarization to the square of the electric field strength E , is called the second order nonlinear susceptibility of the medium and its magnitude describes the strength of second order processes. The $\chi^{(3)}$ term is referred to as second nonlinear susceptibility describing third-order processes. Similarly, higher order terms describe higher order processes. For most materials, these higher order effects are very difficult to observe, so we limit our discussion up to and including third order effects. The second expression of polarization is analogous to the first, except that χ_{eff} is now dependent on the field strength.

The interaction of light with a medium is fully described by Maxwell's equation. The wave equation describing the propagation of an electromagnetic wave is

$$\nabla^2 E = -\frac{\epsilon}{c^2} \frac{\partial^2 E}{\partial t^2}$$

where, c is the speed of light, ϵ is the dielectric constant and ∇^2 is the Laplace operator which is defined as

$$\nabla^2 = \frac{\partial^2}{\partial x^2} + \frac{\partial^2}{\partial y^2} + \frac{\partial^2}{\partial z^2}$$

The above equation relates the time and space variations of the electric field of light through the materials response, specified by the dielectric constant ϵ , and is of fundamental importance in understanding the interaction of field with the medium. An example, is light propagating as a plane wave in the z direction. Then the Maxwell's equation simplifies to

$$\frac{\partial^2 E}{\partial z^2} = -\frac{\epsilon}{c^2} \frac{\partial^2 E}{\partial t^2}$$

A solution for the above equation, is a sinusoidal oscillation

$$E(z, t) = E^{(0)} \cos(\omega t - kz)$$

with

$$k^2 = \frac{\epsilon \omega^2}{c^2}$$

and with $E^{(0)}$ defining the amplitude of the field. The term k is the propagation constant in the material and is equal to 2π times the number of waves per unit length

$$k = \frac{2\pi}{\lambda}$$

The quantity k is a vector called propagation vector. It characterizes the phase of the optical wave with respect to a reference point ($z = 0$, for instance) and kz describes the relative phase of the wave.

Substituting the solution of the Maxwell's equation into the polarization expansion equation gives

$$P = \chi^{(1)}E_0 \cos(\omega t - kz) + \chi^{(2)}E_0^2 \cos^2(\omega t - kz) + \chi^{(3)}E_0^3 \cos^3(\omega t - kz)$$

Using the appropriate trigonometric identities for $\cos^2 \theta$ and $\cos^3 \theta$ gives

$$P = \chi^{(1)}E_0 \cos(\omega t - kz) + \frac{1}{2}\chi^{(2)}E_0^2 [1 + \cos(2\omega t - 2kz)] \\ + \chi^{(3)}E_0^3 \left[\frac{3}{4}\cos(\omega t - kz) + \frac{1}{4}\cos(3\omega t - 3kz) \right]$$

The above equation shows the presence of new frequency components due to the non linear polarization. The second order term gives a frequency independent contribution, as well as one at 2ω , and corresponds to the second-harmonic generation. The third term indicates a frequency response at the frequency of the optical field ω , as well as at 3ω , which refers to the third-harmonic generation.

Another manifestation of nonlinear optics is the so-called nonlinear index of refraction of the medium. The refraction index (n) is another way of representing the optical response of a medium. For an isotropic medium

$$n^2 = 1 + 4\pi\chi_{eff}$$

When a medium is subjected to a dc electric field, which we designate as $E(0)$, and an optical field $E(\omega)$, the total field of the medium is

$$E = E(0) + E(\omega) = E(0) + E_0 \cos(\omega t - kz)$$

Substituting to the polarization expansion equation gives

$$P = \chi^{(1)}[E(0) + E_0 \cos(\omega t - kz)] + \chi^{(2)}[E(0) + E_0 \cos(\omega t - kz)]^2 \\ + \chi^{(3)}[E(0) + E_0 \cos(\omega t - kz)]^3 + \dots$$

Expanding these terms, applying the appropriate trigonometric identities, and collecting terms that describe oscillation ω gives

$$P(\omega) = \chi^{(1)}E_0 \cos(\omega t - kz) + 2\chi^{(2)}E(0)E_0 \cos(\omega t - kz) \\ + 3\chi^{(3)}E_0^2 E(0) \cos(\omega t - kz) + \frac{3}{4}\chi^{(3)}E_0^3 \cos(\omega t - kz) \\ = \chi_{eff} E(0) \cos(\omega t - kz)$$

Substituting χ_{eff} to the refraction index equation, results in:

$$n^2 = 1 + 4\pi[\chi^{(1)} + 2\chi^{(2)}E(0) + 3\chi^{(3)}E^2(0) + \frac{3}{4}\chi^{(3)}E_0^2]$$

By replacing $n_0^2 = 1 + 4\pi\chi^{(1)}$, which corresponds to the linear index of refraction, gives

$$n = n_0 + \frac{4\pi\chi^{(2)}}{n_0}E(0) + \frac{6\pi\chi^{(3)}}{n_0}E(0)^2 + \frac{3\pi}{2n_0}\chi^{(3)}E_0^2$$

The definition of the light intensity in cgs units is:

$$E_0^2 = \frac{8\pi}{cn}I(\omega)$$

which when substituted to the above equation of the index of refraction gives

$$n = n_0 + \frac{4\pi\chi^{(2)}}{n_0}E(0) + \frac{6\pi\chi^{(3)}}{n_0}E(0)^2 + \frac{12\pi^2}{cn_0^2}\chi^{(3)}I$$

where,

$$\frac{4\pi\chi^{(2)}}{n_0} = n_1$$

$$\frac{6\pi\chi^{(3)}}{n_0} = n_2(0)$$

$$\frac{12\pi^2}{cn_0^2}\chi^{(3)} = n_2(\omega)$$

and correspond to the linear electrooptic effect, the quadratic electrooptic effect, and the optical Kerr effect, respectively. The later corresponds to the light intensity-dependent refractive index.

When light passes through a semiconductor, the material absorption creates excitations, the so called excitons, which are electron-hole pairs. The concentration of excitons will depend on light intensity. The refractive index of the material is dependent on the concentration of the optically generated excitations. Consequently, the refractive index will depend on intensity [72]. This population effect describes a $\chi^{(3)}$ process, which is a measure of the intensity dependent refractive index. Such a process though, cannot contribute to third-harmonic generation and thus constitutes a fundamentally different type of effect. This resonant $\chi^{(3)}$ is sometimes called dynamic nonlinearity or incoherent nonlinearity, because it depends on the excited state population, and its response time

is determined by the dynamics of the population decay. If the absorption of a material to an excited state is intensity dependent, the change in absorption $\Delta\alpha$, as a function of intensity gives rise to a change in refractive index Δn by the Kramers-Kroening relation as follows

$$\Delta n(\omega) = \frac{c}{\pi} p. v. \int_0^{\infty} \frac{d\omega' \Delta\alpha(\omega')}{\omega'^2 - \omega^2}$$

This equation is often used for the calculation of Δn and $\chi^{(3)}$. The mechanisms that give rise to the intensity dependence of absorption are the following:

Saturable Absorption. Materials processing strong electronic absorptions can behave as saturable absorbers as long as the rate of populating the excited states exceeds the rate of return to the ground state. As the excited states are populated, there is a corresponding depletion of the ground state population, which leads to a decrease in the absorption involving transition from the ground state. Consequently, the absorption saturates at higher intensities. The result is an intensity dependent absorption.

Phase-Space Filling. This is a special case of saturation of ground state absorption, originally proposed for multiple-quantum well semiconductors. In these systems, the lowest energy excitation produces excitons, which are correlated electron-hole pairs. These excitons have a certain geometric size corresponding to the average separation between the electron and hole. At low excitation densities, the excitons behave like bosons (neutral particles). At higher excitation densities, the excitonic separation approaches the geometric size of excitons. At this excitation density, excitons no longer behave like bosons, and the fermion nature (charged particle repulsion) of electron-hole pair now becomes manifested in blocking further photogeneration of excitons. This is called the space filling of excitons, which results to the reduction of the absorption length. The result is an intensity dependent absorption, which, according to Kramers-Kroening relation, leads to an intensity dependent refractive index and hence $\chi^{(3)}$.

This intensity dependent refractive index leads to a special case of processes, the so called self-action effects. It is called self-action effect since the nonlinear polarization created by an incident beam affects the propagation and other properties of the same beam, through an intensity dependent refractive index. These types of effects are:

Self-focusing, which occurs as a combined result of positive n_2 , and a spatial variation of the laser intensity, in which the beam is more intense in the center than at the edges.

The result is that the refractive index of the nonlinear medium in the center of the beam is larger than at the edges and the medium acts as a positive lens focusing the beam.

Self-defocusing, which results when n_2 is negative. In this case the spatial variation of the laser intensity creates a negative lens resulting in defocusing of the beam.

Self-phase modulation, which is associated with the temporal behavior of the induced refractive index change, $\Delta n(t) = n_2 I(t)$, and is important only when the optical pulse is of the order of a picosecond or less. The result is broadening of the frequency profile.

1.4 Photonic crystals

Photonic crystals are periodically structured electromagnetic media, generally possessing photonic band-gaps: “ranges of frequency where no light propagation is allowed through the structure [73]”. The periodicity of such structures is proportional to the wavelength of light in the band-gap. Photonic crystals can be treated as the electromagnetic analogue of a crystalline atomic lattice that acts on the electron wavefunction to produce the familiar energy band gaps. For example semiconductors have a complete band-gap between the conduction and the valence energy bands. The optical analogue is the photonic crystal, in which the atoms or molecules are replaced by macroscopic media with different dielectric constants and the periodic potential is replaced by a periodic dielectric function or, equivalently, a periodic index of refraction [74].

The field of photonic crystals is a marriage of solid state physics and electromagnetism. They are called “crystals” because of their periodicity, and “photonic” because they act on light. In order to understand how they work, imagine shining a light through a large block of glass with a single bubble of air in it. When light strikes the bubble, some of it will reflect and some of it will continue forward at a slightly different angle (be refracted) [75]. As you look through the glass, this scattered light allows you to see the bubble. Picture now a second bubble in the glass, just like the first one, but at a different place. As before, the light will reflect and refract, this time from both bubbles. Next, suppose that we fill the glass with millions of bubbles, all identical and arranged in a perfect periodic lattice extending in all directions. If someone would look carefully enough, he/she would discover that all of these reflections and refractions cancel one another before reaching our eyes, and the light passes through the crystal unimpeded.

This is no accident, but a general consequence of the periodicity of the structure. Light waves, like all waves, can interfere and even cancel if they superimpose. At this part, it is helpful to mention Bloch's or Floquet's theorem, which says that, in a periodic medium, waves can be found that propagate without scattering, and this is equally true whether the waves consist of electrons or of light beams or sound or... . This theorem leads to many other curious phenomena, if the above bubbles (the scatterers) have period in the order of the wavelength of light and if they have the right shape. It is thus possible that all of those reflections and refractions will cancel not only the light scattered sideways, but the light moving forward as well. Then because the light has to go somewhere (energy is conserved), it has no choice but to go back, it is forbidden from entering the photonic crystal. This happens no matter what direction the light is coming from, in a certain range of wavelengths called the *photonic band-gap* [76].

Once you have such a medium, impervious to light, you can manipulate photons in many interesting ways. By carving a tunnel through the material, you have an optical wire from which no light can deviate. By making a cavity in the center of the crystal, you have an optical "cage" in which a beam of light could be caught and held. These kinds of abilities to trap and guide light have many potential applications in optical communications and computing, where we would like to make tiny optical "circuits" to help manage the ever-increasing traffic through the world's optical communication networks. Other potential devices that can be fabricated from this control over light are: more efficient lasers and LED light sources and cellular phones that don't pump half of their signal power into our head.

1.4.1 Basic concepts

A PC is defined as a periodic dielectric structure with an index of refraction periodicity of the order of the wavelength of light being localized. These structures were first described by Yablonovitch [77] and John [78] in 1987. Since then the number of publications related to PCs has been explosive. Schematic pictures of one-, two- and three-dimensional (1D, 2D and 3D) PCs are presented in figure 1.13 where the high- and low-index materials are shown in different colors.

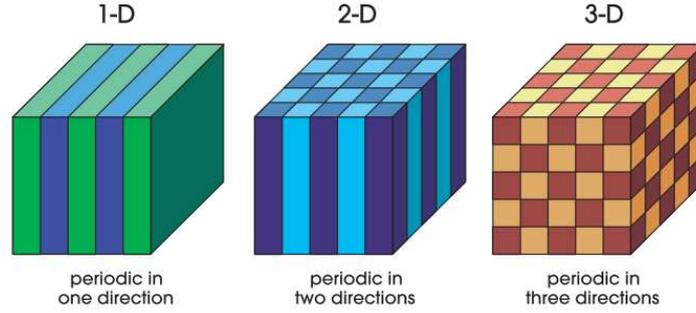


Figure 1.13. Schematic representation of 1D, 2D and 3D photonic crystals.

The electric permittivity varies along one, two or three dimensions respectively. Adapted from ref. [76]

PC properties are not based on absorption or emission transitions. Instead they are determined entirely by the index of refraction periodicity which can be scaled from submicron dimensions (to control UV/VUV light) to the centimeter scale (to control microwaves). PCs are beginning to have a profound effect on the development of nanoscale devices because they can significantly enhance the interactions between light and matter

The interaction of light with materials as well as the propagation of light within a material, are described by the macroscopic Maxwell's equations:

$$\begin{aligned}\nabla \cdot \mathbf{B} &= \mathbf{0} \\ \nabla \cdot \mathbf{D} &= \rho \\ \nabla \times \mathbf{E} + \frac{\partial \mathbf{B}}{\partial t} &= \mathbf{0} \\ \nabla \times \mathbf{H} - \frac{\partial \mathbf{D}}{\partial t} &= \mathbf{j}\end{aligned}$$

together with the constituent materials equations

$$\begin{aligned}\mathbf{D} &= \epsilon_0 \mathbf{E} + \mathbf{P} \\ \mathbf{B} &= \mu_0 (\mathbf{H} + \mathbf{M})\end{aligned}$$

Where, \mathbf{D} is the electric displacement, \mathbf{B} the magnetic induction, \mathbf{E} the electric field, \mathbf{H} the magnetic field, ρ is the free charge density and \mathbf{j} the free current density, \mathbf{P} the polarization and \mathbf{M} the magnetization. For simplification only linear optics and isotropic materials will be assumed so that the latter two equations reduce to:

$$\begin{aligned}\mathbf{D} &= \epsilon_0 \epsilon \mathbf{E} \\ \mathbf{B} &= \mu_0 \mu \mathbf{H}\end{aligned}$$

From this set of equations the master equation can be derived, which describes the propagation of electric and magnetic fields. Moreover, it will be assumed that there are no free charges and no free currents present in the materials under consideration, that is $\mathbf{r} = 0$ and $\mathbf{j} = 0$. This is valid for all the dielectric materials that will be mentioned and in the above described case of linear-optics.

Combining all the above equations provides us with the master equation for the propagation of the magnetic field

$$\frac{1}{\mu} \nabla \times \left(\frac{1}{\epsilon} \nabla \times \mathbf{H} \right) = \frac{\omega^2}{c^2} \mathbf{H}$$

It is assumed that the magnetic field can be written in the following form:

$$\mathbf{H} = \mathbf{H}(\mathbf{r}, t) = \mathbf{H}(\mathbf{r}) e^{-i\omega t}$$

For all known natural materials the magnetic permeability μ is unity at optical frequencies, reducing this equation to the following form of an eigenvalue equation:

$$\nabla \times \left(\frac{1}{\epsilon} \nabla \times \mathbf{H} \right) = \frac{\omega^2}{c^2} \mathbf{H}$$

The optical properties of the photonic crystal and its dispersion relation are given by the eigenvalues on the right hand side. For homogeneous and isotropic materials (e.g., a solid block of glass) the permittivity ϵ does not depend on the spatial coordinates and, hence, the dispersion is solely described by the materials properties alone (in this case we can move ϵ to the right hand side of the equation, giving us the well-known wave equation).

If we now introduce through periodic ordering a spatial dependence of the materials properties (see Fig. 1.14), we can control the eigenvalues and hence the optical properties of the material through the distribution of the material. We control the operator acting on the magnetic field on the left-hand side, giving us the desired eigenvalues on the right-hand side. Considering periodically arranged materials, i.e., imposing translational symmetry into the structure,

$$\epsilon(\mathbf{r}) = \epsilon(\mathbf{r} + \mathbf{R})$$

with \mathbf{R} being a lattice-translation vector, solutions of the master equation will have the following form, well known from solid-state physics:

$$\mathbf{H}(\mathbf{r}) = \mathbf{h}_k(\mathbf{r}) e^{i\mathbf{k}\mathbf{r}}$$

$$\mathbf{h}_k(\mathbf{r}) = \mathbf{h}_k(\mathbf{r} + \mathbf{R})$$

This solution is known as the Bloch function. This ansatz solves the master equation. As there are no analytically closed solutions, this task is usually accomplished via numerical methods, e.g., with the plane-wave expansion method.

1.4.2 1D photonic crystals: Photonic bandgaps and photonic bandstructure

To discuss the essential properties of periodically structured materials, we start with an intuitive approach to 1D systems, which we gradually expand to higher dimensions.

For the beginning, we assume light propagating in a homogeneous, isotropic material with an index of refraction of n . The index of refraction and the permittivity are related via $n = \sqrt{\epsilon}$. The optical properties of this material are described by the dispersion relation:

$$\omega = \frac{c}{n} |k|$$

with the vacuum speed of light c , wave vector $|k| = k = \frac{2\pi}{\lambda}$ and λ being the vacuum wavelength of light. The energy of the photons is given by $E = \hbar\omega$. Plotting the dispersion relation for forward propagation (positive k -values), results in a straight line. For backward propagation (negative k -values) we get the same dispersion properties (blue lines starting at the origin in Fig. 1.14).

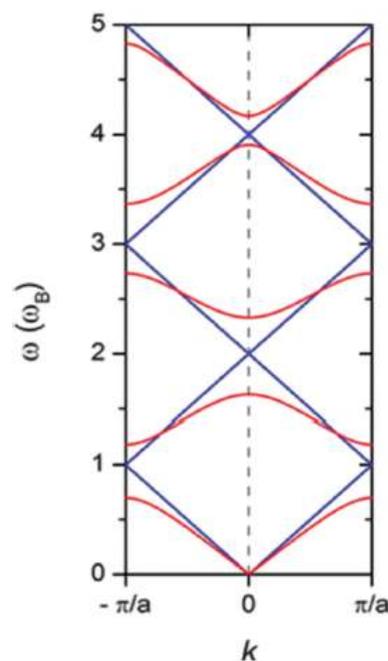


Figure 1.14. Light lines and the formation of a band gap. For the calculation material slabs of thickness 200 nm and refractive indices of 1.0 and 3.5 have been assumed. The blue lines show the dispersion relation in an isotropic medium with artificial periodicity.

The physics of our material will not change if we compose it in a hypothetical experiment from slabs with certain thickness a , glued seamlessly together. This introduces a periodic structure with a lattice constant a . As each unit cell has absolutely the same properties as every other unit cell of our material, we can limit our discussion to just one single unit cell, the primitive cell, sufficient to construct the whole structure. The lattice vectors \mathbf{R} in real space, in which we construct our sample and the ones of the reciprocal space (\mathbf{G}), in which we draw our dispersion relation, are closely related:

$$\mathbf{R} \cdot \mathbf{G} = n2\pi$$

with m being a positive integer.

Hence, real-space periodicity results in periodicity in our dispersion relation: This leads to several branches of the original dispersion relation running through our primitive unit cell in reciprocal space, called the 1st Brillouin zone, extending from $k = -\pi/\alpha$ to $k = +\pi/\alpha$. We also can construct the exact same picture, if we back-fold the dispersion bands starting at the origin every time they hit the boundary of the Brillouin-zone. This leads to the picture shown in Fig. 1.14 with the solid blue lines. Interestingly, the crossing points of the dispersion lines of the forward and backward propagating waves are located at the frequency:

$$\omega = \frac{c\pi}{\sqrt{\epsilon}\alpha}$$

This is nothing else but the Bragg-condition known from X-ray diffraction, but at optical wavelengths. Things become more interesting, if we introduce different materials. Let us first assume that each slab is now divided into two materials with different permittivity, keeping the overall periodicity exactly the same.

A forward propagating wave is now partially reflected at every interface between the two materials, leading to forward and backward travelling waves at the same time. The interference of forward and backward propagating waves leads to the formation of a standing wave for frequencies fulfilling the Bragg-condition, i.e., right at the edge of the Brillouin-zone. Where will the nodes and antinodes of these standing waves be located? Due to symmetry considerations, there are just two possible solutions: The nodes and antinodes are either situated in the low-refractive index and in the high-

refractive index material or the other way round. In-between-positions are forbidden, as the physics has to stay the same under sample-rotations in the laboratory. These two standing waves experience different effective refractive indices: The electric field for the standing wave with the nodes in the low index material experiences mainly the high-index material, resulting in lower photon energy according to the above equation. The other standing wave experiences a reduced effective index and will thus be found at higher photon energies. This leads to the opening of a gap in the dispersion relation, the photonic band gap. The energetic lower band is called the “dielectric band”, as its corresponding electric field is mainly concentrated in the high-index material, e.g., silicon. The higher energetic band is, hence, called the “air band”, as its electric field is mainly concentrated in the low index material, most of the time air. The resulting dispersion relation or band structure is depicted by the red curves in Fig. 1.14. For photons with energies inside the band gap, no propagation inside the photonic crystal is allowed. As can be seen directly from Fig. 1.14, we do not only get the fundamental band gap, but also higher order gaps, at least for one dimensional systems. The center position of the gap is still perfectly described by the Bragg-condition. From the above equation we directly conclude that we can shift the band gap position by either changing the lattice constant or the materials properties or both. Changing the high dielectric constant material mainly influences the dielectric band while changing the low index material mainly shifts the air band. Increasing the contrast between the two materials’ dielectric functions widens the width of the band gap.

1.4.3 2D photonic crystals

2D PhCs are periodic in two directions and homogenous in the third. By symmetry, an electromagnetic wave propagating, for example, in the xy -plane of a 2D PhC can be classified as transverse electric (TE) or transverse magnetic (TM) depending on their reflection symmetry through the xy -plane. TE modes have their H -vector perpendicular to the plane in the z -direction and their E -vector in the xy -plane. Conversely, TM modes have their E -vector perpendicular to the plane and the H -vector in the xy -plane. 2D PhCs are more complicated than 1D structures because their photonic responses are different for these two different polarizations. They can reflect light however from any direction in the plane unlike 1D PhCs which only reflect light at normal incidence.

Highly symmetrical 2D PhC geometries are usually either square or hexagonal [79]. It is common to label the direction of light propagation in a photonic band structure diagram according to the following standard reciprocal space notation for the irreducible Brillouin zones of square and hexagonal lattices having periodicity, a , respectively. All other points in reciprocal space are related to these positions by rotational symmetry in the plane. Although the relationship between a square lattice and its Brillouin zone is straightforward, it is less so for a hexagonal lattice and its reciprocal primitive cell. Therefore this is shown diagrammatically in figure 1.15.

Analysis shows that for square column array of high-index dielectric islands a photonic band gap will open between the first (dielectric) band and the second (air) band for the TM modes but not for the TE modes (figure 1.16). Physically, this happens because the lowest TM mode is localized in the high dielectric regions while most of the electromagnetic power of the air band is found in the low- ϵ regions.

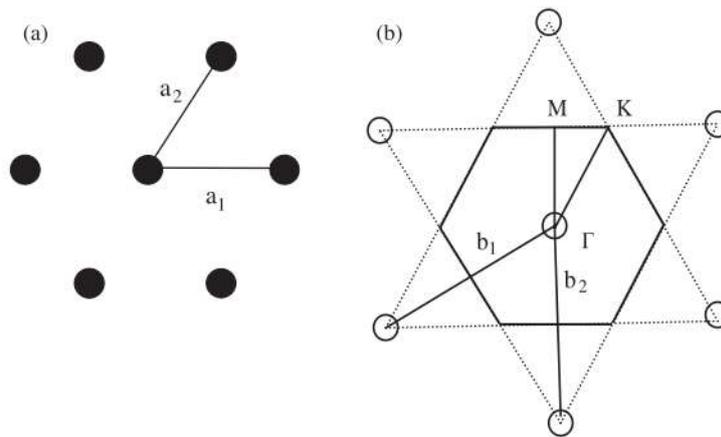


Figure 1.15. (a) A hexagonal lattice with crystal lattice $a_1 = a_2 = a$. (b) The reciprocal lattice of (a) with unit lattice $b_1 = b_2 = \frac{4\pi}{\sqrt{3}a}$. The connected dashed lines indicate how the first Brillouin zone can be constructed. The irreducible Brillouin zone is the triangular wedge bound by points Γ , M and K . Picture adapted from ref. [73]

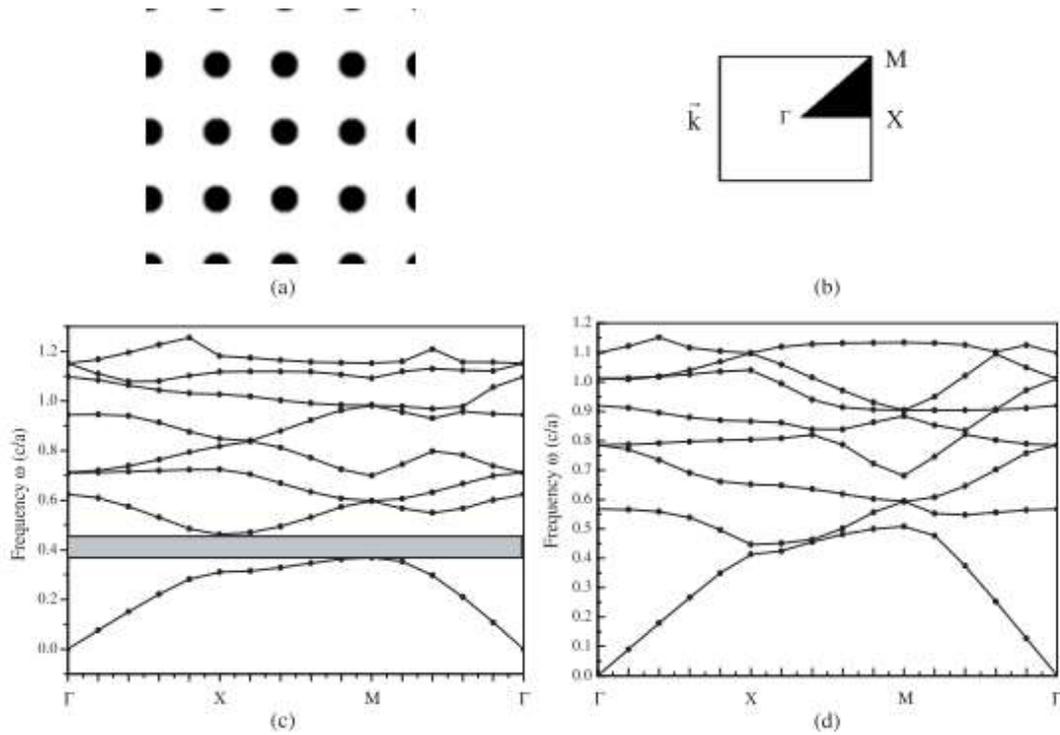


Figure 1.16. (a) A two-dimensional rod lattice with $r/a = 0.2$ ($r =$ radius of each rod) and $\epsilon_{\text{high}}/\epsilon_{\text{low}} = 12$. (b) The first Brillouin zone. The filled-in triangle is the irreducible Brillouin zone. (c) Photonic band diagram for the TM modes. The grey box indicates the photonic band gap (d) Photonic band diagram for the TE modes which do not exhibit a photonic band gap. Picture adapted from ref. [73]

A ‘compromise’ lattice of a high dielectric material can be created that is nearly isolated yet also connected (figure 1.17(a)) [80]. Specifically, a hexagonal lattice of air holes placed inside the high-index material creates an array of triangular high ϵ -spots connected by narrow veins. Figure 1.17(b) shows the resultant photonic band diagram calculated for a structure with a dielectric contrast = 6.7. A photonic band gap and hence complete reflection is found for both the TE and TM modes. Conversely, a hexagonal array of isolated high-index columns exhibits a band gap for the TM modes only.

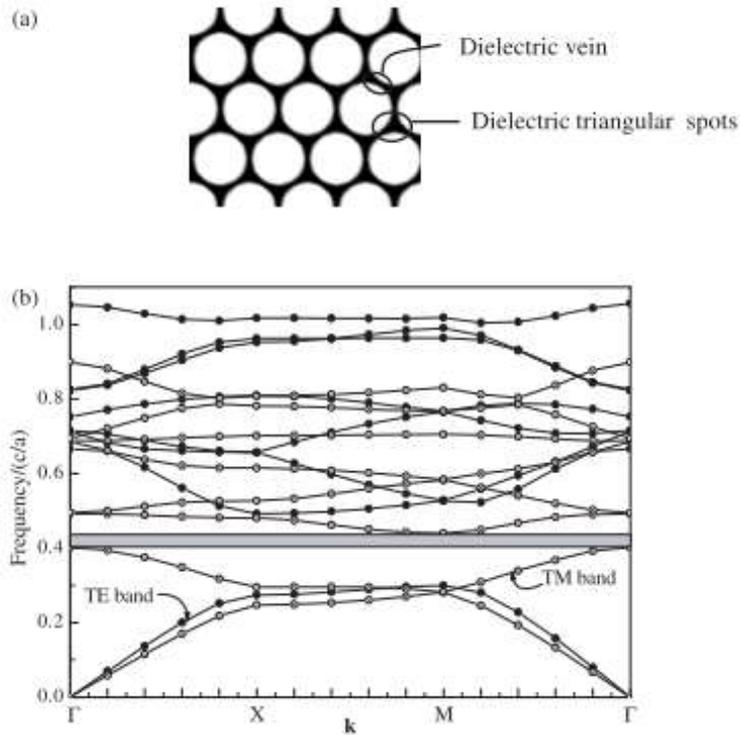


Figure 1.17. (a) A 2D triangular photonic crystal with a complete band gap for both TE and TM modes. The structure is a column array of air holes ($\epsilon_{\text{low}}=1$) in a dielectric substrate ($\epsilon_{\text{high}}=2.7$) with $r/a = 0.45$. A dielectric triangular spot and vein are indicated. (b) Photonic band diagram for the structure shown in (a). The open circles correspond to TM modes while the closed circles to TE modes. The grey box shows the photonic band gap. Picture adapted from ref. [73]

The size of the photonic band gap can be characterized by the gap–midgap ratio which is defined $\frac{\Delta\omega}{\omega_0}$, where $\Delta\omega$ is the gap frequency width and ω_0 is the frequency at the middle of the gap. This parameter which is typically of the order of 0.2 is more meaningful than $\Delta\omega$ alone as a measure of the size of the band gap since it is invariant to size scaling.

The size of the band gap is affected by many parameters including the structural symmetry of the crystal, the dielectric constant ratio, the air-filling ratio and so on. Although it is difficult to provide a quantitative formula to describe the relationships between these parameters, the size of the gap can be calculated provided the structure is symmetrical. For example, it can be shown that the photonic band gap disappears for the structure shown in figure 1.17(a) when the dielectric constant ratio equals to 4. While the band gap can be increased to $\sim 5.2\%$ when the dielectric constant ratio

reaches 12:1 (Si/air), its value will be zero when the ratio $r/a = 0.2$ even when the dielectric constant ratio equals to 12.

1.4.4 3D photonic crystals

The optical analogue of an ordinary crystal is a three-dimensional photonic crystal: a dielectric structure that is periodic along three different axes. Three-dimensional photonic crystals can have all the novel properties of the above discussed 1D and 2D photonic crystals.

Although there are an infinite number of possible geometries for a three-dimensional photonic crystal, we are especially interested in those geometries that promote the existence of photonic band gaps. So, generally, we want a network of dielectric channels running along all the directions in which the electric field can point. It turns out that the choice of the lattice and how it is connected is critical in determining how easily we obtain a band gap.

Figure 1.18 is a schematic representation of several three-dimensional lattices of spheres in a cubic cell. The simplest lattice is formed by the blue spheres at the corners of the cube, with primitive lattice vectors αx , αy , and αz . This is the simple cubic lattice. If we add the dark red spheres at the centers of the faces, we obtain a face-centered cubic (or fcc) lattice. The fcc lattice vectors are $(x + y)\alpha/2$, $(y + z)\alpha/2$, and $(x + z)\alpha/2$. For the fcc lattice, the smallest repeating unit (the primitive cell) is not the cubic cell shown in figure 1. Rather, the primitive cell is a rhombohedron (with volume $\alpha^3/4$) whose edges are the three lattice vectors. The cubic cell contains four copies of this primitive cell, and is an example of a supercell. Finally, if we add the pink spheres, which represent another fcc lattice that is shifted by $(\alpha/4, \alpha/4, \alpha/4)$ relative to the blue spheres, then we obtain a diamond lattice. The periodicity in this case is the same as for the fcc lattice, but there are two “atoms” per rhombohedral primitive cell.

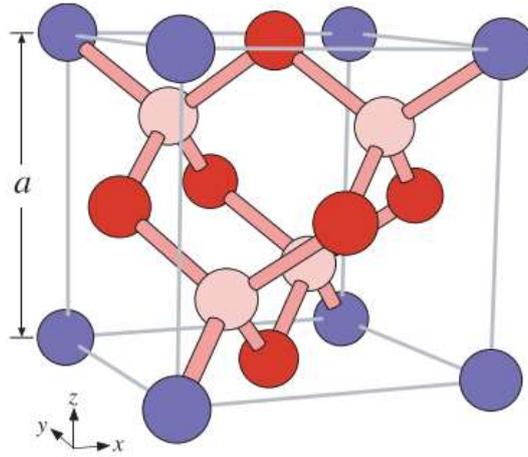


Figure 1.18. Ball-and-stick (“atomic”) representation of several three-dimensional lattices in a cubic supercell, with a lattice constant a . The blue balls alone form a simple cubic lattice. Adding the dark red balls produces a face-centered cubic (fcc) lattice. Adding the pink balls as well produces a diamond lattice, with stick “bonds” (four bonds per ball). Picture adapted from ref. [76].

A 3D photonic crystal is created if we replace the “atoms” and “bonds” with a higher- ϵ material and a lower- ϵ material respectively. The ratio of the two dielectric constants matters most ($\frac{\epsilon_{\text{high}}}{\epsilon_{\text{low}}}$) and not their individual values. Bandgaps tend to appear in structures with a high dielectric contrast. The more significant the scattering of light, the more likely a gap will open up.

For three-dimensional crystals, complete photonic band gaps are rare. The gap must smoother the entire three-dimensional Brillouin zone, not just any one plane or line. For example, in figure 1.19 we show the band structure for a face-centered cubic (fcc) lattice of close-packed (tangent) high-dielectric spheres ($\epsilon = 13$) in air. Although the dielectric contrast is very large, there is no complete photonic bandgap.

Nevertheless, a number of three-dimensional crystals have been discovered that do yield sizable complete photonic band gaps. In most of the theoretical studies of these structures undertaken to date, the results are as follows. For a given crystal lattice, there is no photonic band gap until the dielectric contrast is increased to some threshold value. Above this nonzero threshold, the gap opens up and its width usually increases monotonically with the dielectric contrast, assuming optimal parameters are chosen. These optimal structural parameters (e.g., the radius of the tubes or spheres), which maximize the width of the band gap, vary with the dielectric contrast.

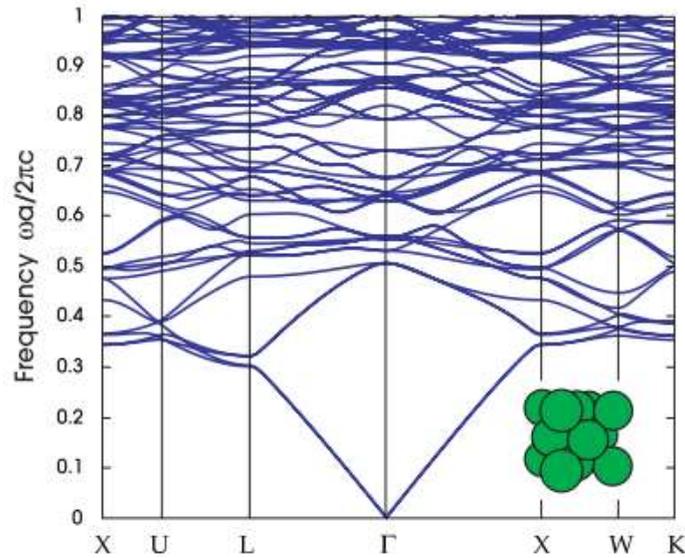


Figure 1.20. Photonic band structure for the lowest-frequency electromagnetic modes of a face-centered cubic (fcc) lattice of close-packed dielectric spheres ($\epsilon=13$) in air (inset). Picture adapted from ref. [76]

The possibility of three-dimensional photonic band gaps in periodic structures was first suggested by Yablonovitch in 1987, exactly one century after Lord Rayleigh (1887) described one-dimensional band gaps. It took three more years, however, before a specific dielectric structure was correctly predicted to have a complete band gap in three dimensions, by Ho et al. (1990) [81]. Subsequently, a large number of systems with band gaps have been proposed based on theoretical calculations, and in many cases these structures have been fabricated and characterized at wavelengths ranging from the microwave regime to the infrared regime.

As mentioned above, the first experimental realization of a 3D PhC was achieved by Yablonovitch et al. who fabricated a face centred cubic (fcc or opal-like) crystal in a low-loss dielectric medium, with a band gap operating in the microwave, by mechanically drilling tens of thousands of holes with radii slightly larger than close packing so that the voids joined up to form a connected network [82]. That system is known as the three cylinder structure or simply Yablonovite in recognition of this achievement. The drilling angles along the three equivalent (110) directions used to generate Yablonovite are shown in figure 1.20(a) [83]. Both Yablonovite and its inverse structures are found to possess a complete band gap in three dimensions as seen in figure 1.20(c). The micron-scale Yablonovite crystal shown in figure 1.20(b) was made

by chemically assisted ion beam etching through a triangular hole array mask, defined by e-beam lithography on GaAs.

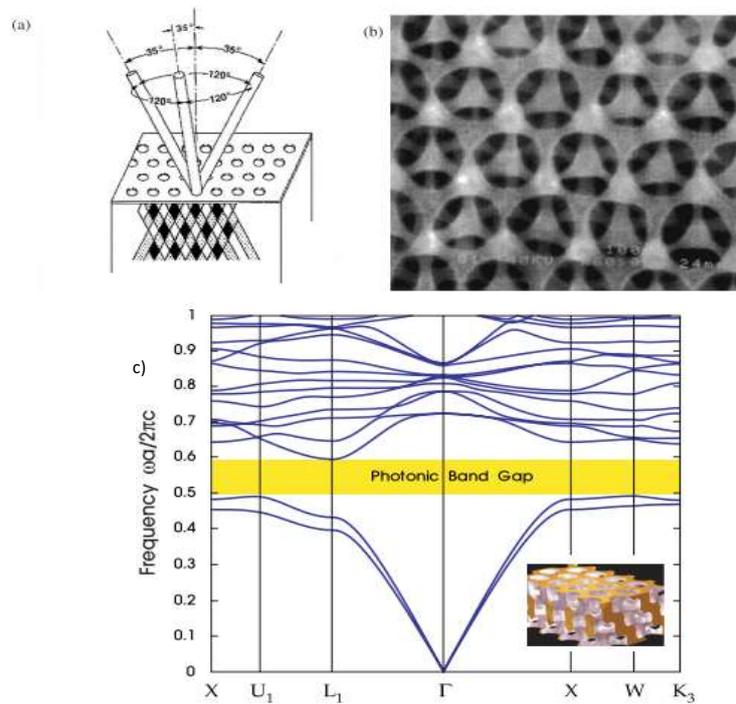


Figure 1.20. (a) Drilling angles used to make Yablonovite, (b) Yablonovite fabricated by e-beam lithography [83], (c) The photonic band structure for the lowest bands of Yablonovite [76]

One structure which is predicted to have a large complete band gap is a 3D diamond lattice of spheres [81]. Band gaps have been found for other structures including the simple cubic [84] and the rhombohedral A7 lattice [85]. It was shown that the largest gap–midgap ratio (0.46) can be achieved for an inverse diamond lattice of overlapping air holes in a dielectric with a filling fraction of 0.81. An example is shown in figure 1.21. Physically, this corresponds to 3D PhC made essentially of air voids with an ultrathin dielectric skeleton framework. Coupled with the fact that visible reflections require submicron periodicities, it is hardly surprising that fabrication of this lattice for operation at these high frequencies continues to be extremely challenging.

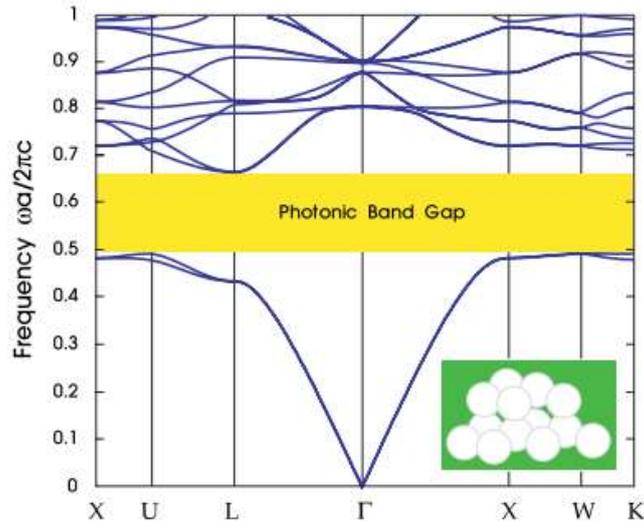


Figure 1.21. The photonic band structure for the lowest bands of a diamond lattice of air spheres in a high dielectric ($\epsilon=13$) material (inset). A complete photonic band gap is shown in yellow [76].

The first three-dimensional photonic crystal with a complete gap to be fabricated on micron scales, for light at infrared wavelengths, was the crystal shown in figure 1.22(b). This structure was proposed independently by Ho et al. (1994) [86] and Sözüer and Dowling (1994) [87], and was dubbed a woodpile structure by the latter authors. It consists of layers of one dimensional rods with a stacking sequence that repeats itself every four layers. The distance between four adjacent layers is “a” and within each layer, the axes of the rods are parallel to each other with a distance “d” between them. The adjacent layers are rotated by 90° . Between every other layer, the rods are shifted relative to each other by “d/2”. If the ratio a/d is equal $\sqrt{2}$ an fcc lattice is obtained (figure 1.22(a)).

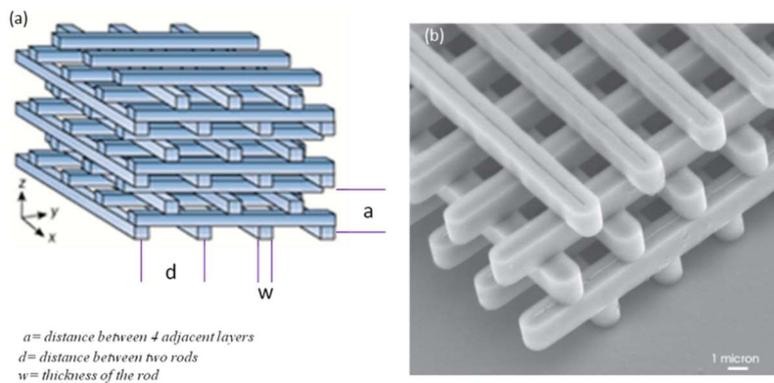


Figure 1.22. (a) Geometry of the woodpile structure (b) Electron-microscope image of a “woodpile” photonic crystal. The crystal is made of silicon and has a complete band gap

centered at a wavelength of approximately 12 microns (Lin et al., 1998b). The dielectric “logs” form an fcc lattice.

The band diagram of this structure, for a dielectric contrast of 13:1, is shown in figure 1.23. It exhibits a 19.5% complete photonic band gap between the second and third bands. In fact, the woodpile crystal, like Yablonovite, can also be understood as a distorted from the diamond lattice (with lower symmetry). If we imagine taking the diamond of figure 1.18 and flattening the bonds so that they lie parallel to the xy plane, then we obtain a woodpile stacking.

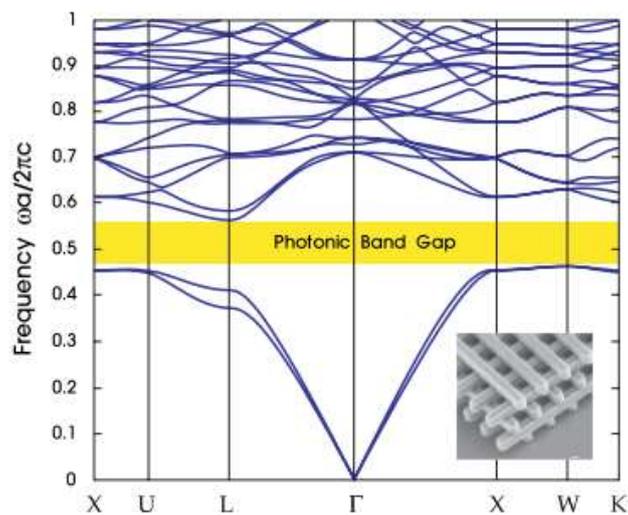


Figure 1.23. The photonic band structure for the lowest bands of the woodpile structure with $\epsilon=13$ logs in air [76].

1.4.5 Applications of photonic crystals

In addressing this question for photonic crystals two main classes of materials have been investigated: (i) passive photonic crystals with the capacity to diffract, guide, localize, transmit and amplify light and (ii) active photonic crystals whose refractive index and/or dimensions and hence diffracted color can be altered by chemical or physical stimuli.

Passive versions of bottom-up photonic crystals have been explored for silicon and dye sensitized solar cells to improve their light trapping efficacy and performance, light emitting diodes to enhance their light extraction efficiency, dye and polymer lasers to improve their stability, versatility and performance, colorful coatings and formulations

for a variety of purposes such as mobile phone and computer packaging, military camouflage, heat management in buildings, fabrics, cosmetics, paints and sunscreens. Besides exploitation of their unique optical properties as outlined above, bottom-up photonic crystals have also been used as macroporous high surface area supports, for example as a transparent conducting oxide electrode for housing electroluminescent and photoactive materials in displays and solar cells, as a gold-titania electrode for sensing hydrogen peroxide in the electrocatalysis of horseradish peroxidase, as a platinum electrode for the electro-oxidation of methanol, and as silicon, carbon and sulphur based electrodes for enhanced performance lithium ion batteries and supercapacitors.

In the chemical arena, active photonic crystal refractive index and/or dimensionally induced color changes have been used for label-free chemical and biochemical sensing, probing chiral recognition, monitoring DNA hybridization, watching enzyme activity, detecting bacteria and following silver antibacterial and chemical oscillators in action, checking food and water quality, viewing ion-exchange, enabling high resolution chromatographic separation, controlling surface wettability, and detecting heavy metals. In addition, slow photon amplification in photonic crystal materials has been shown to speed up the rates of photo-oxidation and photo-isomerization reactions, relative to the same material, devoid of the attributes of the photonic lattice.

The ability to tune the structural color of photonic crystals through physically induced changes in their refractive indices and/or dimensions has been achieved through electrical, magnetic, optical, electro-optical, thermal and mechanical stimuli enabling demonstrations of full color displays, color tunable photonic paper and ink, color fingerprinting, thermal printing, color coded battery state-of-charge, user interactive bank notes, credit card and passport anti-counterfeit systems and optical switching.

CHAPTER 2: Redox Multiphoton Polymerization for 3D Nanofabrication

In this chapter, we will present the synthesis of a novel organic–inorganic composite material, in which one of the components, a vanadium metallo-organic complex, initiates the polymerization, bypassing the need for use of a photoinitiator. The initiation process is based on a redox reaction, leading to a redox multi-photon polymerization, which is presented for the first time in literature. The composite employs multiphoton absorption to self-generate radicals by photoinduced reduction of the metal species from vanadium (V) to vanadium (IV). We exploit this material for the fabrication of fully 3D structures by multiphoton polymerization with 200 nm resolution, employing a femtosecond laser operating at 800 nm, in the absence of a photoinitiator. Nonlinear absorption measurements indicate that the use of an 800 nm laser initiates the photopolymerization due to three-photon absorption of the vanadium alkoxide. Moreover, the laser power required to induce this three-photon polymerization is comparable to that required for inducing two-photon polymerization in materials using standard two-photon absorbers, most likely due to the high content of vanadium in the composite (up to 50% mole).

2.1 Introduction

Direct laser writing (DLW) based on multiphoton polymerization has attracted the attention of the research community the past decades, as it possesses the ability to fabricate real 3D micro- and nanosized objects with complicated geometries [88], [89]. In DLW, the beam of an ultrafast laser is tightly focused into the volume of a photosensitive material transparent to the laser wavelength. Multiphoton-induced absorption inside the focused laser beam voxel initiates a polymerization process. By moving the sample or the laser beam focus in the three-dimensions, high-resolution structures can be written into the volume of the material.

The materials suitable for this technology might be purely organic, usually organic vinyl monomers or oligomers, or hybrid, consisting of an inorganic network chemically attached to an organic backbone [90]. The latter have attracted particular interest due

to their enhanced mechanical strength, resistance to shrinkage, and combination of the dissimilar properties of their constituents [91]. The precursor molecules required for the synthesis of these materials are metallo-organic compounds and hybrid organic–inorganic monomers bearing polymerizable vinyl groups and metal alkoxides. For the fabrication of 3D structures by DLW, it is also necessary to add a photoinitiator, a molecule which, upon multiphoton absorption, generates the active species that initiate the polymerization process [92]. In the current study, we circumvent the need for a photoinitiator by employing an metallo-organic compound, vanadium (V) triisopropoxide oxide (VOTIP), which acts simultaneously as an inorganic network forming molecule and a radical supplier. The process relies in the self-generation of radicals via a light-induced intramolecular redox reaction of the vanadium complex. Aliwi et al. have previously reported the photochemical properties of vanadium (V) chelates carrying alkyloxy groups at 365 nm, and they used these molecules to photoinitiate a free-radical polymerization with the simultaneous transition from vanadium (V) to vanadium (IV) species [93].

Herein, we demonstrate for the first time, that such a redox process is also possible using an irradiation wavelength of 800 nm, to induce multiphoton absorption of the vanadium complex. We further employ this redox reaction to fabricate high-resolution 3D structures and show, using the z-scan technique, that photopolymerization is most likely due to the three-photon absorption of the vanadium alkoxide. The efficiency of the three-photon polymerization reaction can be boosted and made comparable to that of the two-photon polymerization process of other, standard materials, by increasing the vanadium alkoxide content of the material.

2.2 Materials and methods

2.2.1 Material Synthesis

The materials investigated in this work, are hybrid photosensitive materials, containing organic and inorganic moieties. Such materials have the advantage of combining the dissimilar properties of the two components, in one system. For the preparation of the materials, the sol-gel process was used. The inorganic part of these composites is derived from metal alkoxides, which upon hydrolysis and condensation, form an inorganic network. The organic part comprises monomer units which carry

photopolymerizable functional groups that are attached to the inorganic network. All materials undergo a four step process [94]:

1. Hydrolysis and condensation of the metal alkoxides or monomers, to form a porous interconnected cluster structure. These reactions are catalyzed by the presence of HCl.
2. Gelation of the material, during which any solvent present in the system, is removed by heating at low temperature. During this step, hydrolysis and condensation also occurs leading to a significant volume loss.
3. The third step involves photopolymerization. Due to the presence of vinyl monomers, a free radical polymerization occurs only in the irradiated area where the radicals are present. This process results in the formation of the polymer backbone and the 3D structure fabrication.
4. The fourth and final step is the material development. At this step the material is immersed in an appropriate solvent and any unpolymersized resins are removed.

The material was produced by the addition of vanadium (V) triisopropoxide oxide [VO(OiPr)₃], (VOTIP,96% Alfa Aesar) and methacryloxypropyl trimethoxysilane (MAPTMS, Sigma-Aldrich). As shown in this work, VOTIP also initiates the photopolymerization, circumventing the need of photoinitiator addition. All chemicals were used without further purification.

The synthesis of the novel composite, as mentioned above, was carried out by a sol-gel process, which has been widely employed earlier for the preparation of vanadium oxide gels upon hydrolysis and condensation of various vanadium alkoxides [95], [96]. In our case, the inorganic network is formed by the condensation of the vanadium and silicon alkoxide groups present at the VOTIP and the methacryloxypropyl trimethoxysilane (MAPTMS) monomer, respectively. Figure 2.1 shows the chemical formulas of the above molecules.

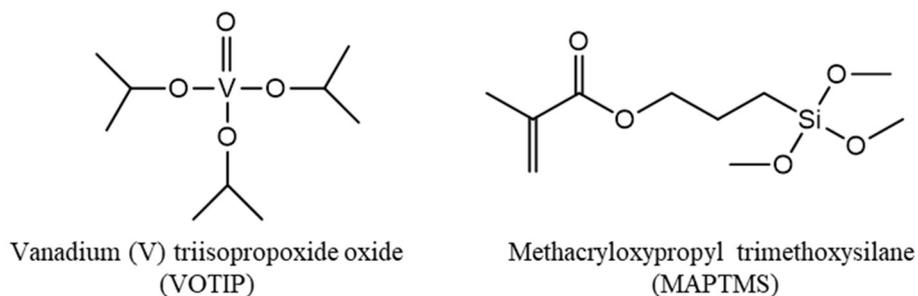


Figure 2.1. Chemical formulas of the precursor molecules used for the synthesis of the material

MAPTMS was first hydrolyzed using an HCl solution (0.1 M) at a 1:0.1 mol ratio. Next, VOTIP was added to the hydrolyzed MAPTMS at a 1:10 to 1:1 molar ratio. The mixture was left stirring overnight and was then filtered using the 0.22 μm syringe filter. The reactions taking place are shown in figure 2.2.

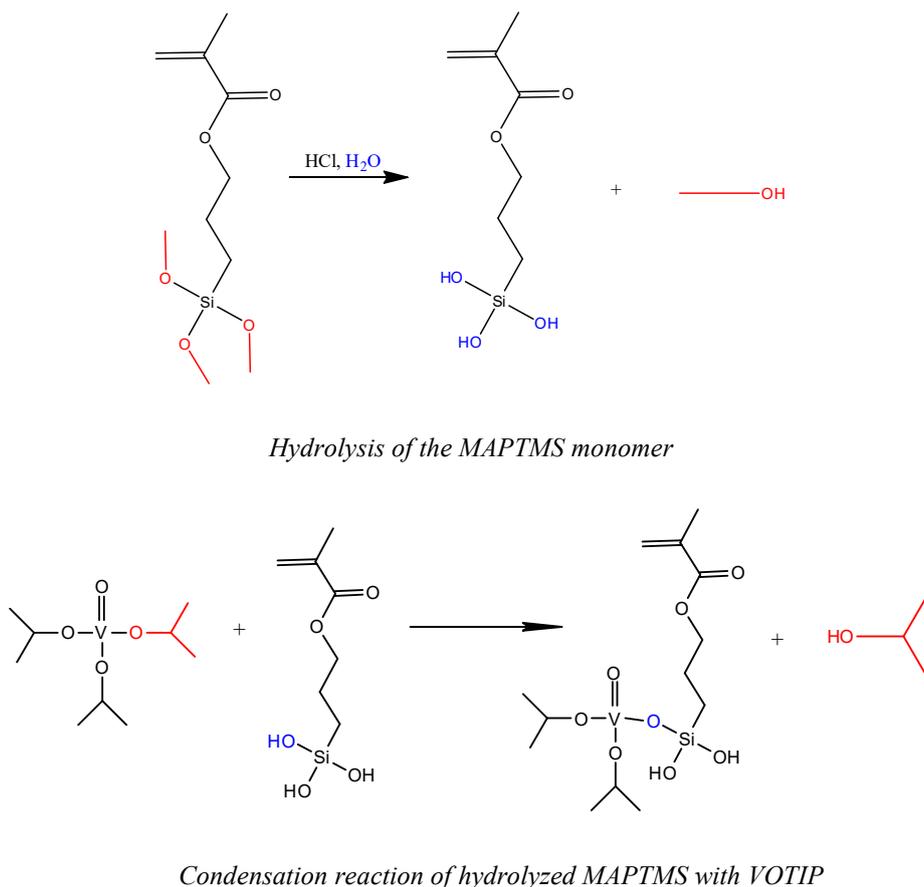


Figure 2.2. The two main reactions of the sol-gel process resulting to the synthesis of the vanadium hybrid material. First the hydrolysis reaction of the MAPTMS monomer and second the condensation of the hydrolyzed MAPTMS with the VOTIP resulting in the formation of the inorganic network.

2.2.3 Sample preparation

The samples were prepared by spin coating a thin film of the material onto silanized square microscope glass substrates for the characterization of the polymerized material, or by drop casting the hybrid material onto 100 μm -thick round silanized glass substrates for the 3D microfabrication. The resultant films/drops were dried in vacuum at 30 °C for 15 min before the photopolymerization. The drying process led to the condensation of the alkoxide groups and the formation of the inorganic network and to any volume loss of the material due to evaporation of possible solvent traces that remained after the condensation process. Next, the samples were exposed to UV (360 nm) or laser (800 nm) irradiation for the formation of the material films and 3D structures, respectively. After the irradiation process, the samples were immersed for 20 minutes in a 50:50 solution of 1-propanol and 2-propanol for development and were further rinsed with 2-propanol.

For the silanization of the glass substrates a two-step procedure was followed. First, a mixture of ammonium hydroxide (NH_4OH) solution 28% w/w with hydrogen peroxide (H_2O_2) solution 35% w/w in a 3:1 volume ratio was prepared. Then, the glass substrates were immersed in the $\text{NH}_4\text{OH}/\text{H}_2\text{O}_2$ solution with both sides facing the liquid mixture. Subsequently, the solution was heated to 75 °C for half an hour. This process leads to the intensive cleaning of the surface of the substrates from any organic residue (dirt) and to the increase of the surface density of the silanol groups on the glass substrate. Finally, the substrates are rinsed thoroughly with deionized water and dried under nitrogen flow. In the second step, the clean substrates are immersed in a mixture of toluene and MAPTMS in a 0,2% volume ratio, with both sides exposed to the mixture. The substrates are left immersed overnight for the formation of a self-assembled layer of MAPTMS by the reaction of the previously created silanol groups with the methoxysilane groups of MAPTMS.

2.2.4 Characterization of the vanadium composite material

Material thin films were prepared onto microscope glass substrates as described in section 2.2.3. The thin films were characterized by UV-Visible spectroscopy, X-Ray diffraction (XRD) spectroscopy, Fourier Transform Infrared (FTIR) spectroscopy and the z-scan technique.

Spectral characterization: the absorption spectra of thin films of the material were recorded in the 250-820 nm spectral range using a Perking Elmer UV-VIS spectrometer.

XRD spectroscopy: X-ray diffraction studies were carried out on thin films prepared as described above. A Rigaku RINT 2000 Series wide-angle diffractometer was used for the measurements.

FTIR spectroscopy: The Attenuated Total Reflection (ATR)-FTIR spectra were recorded on a Thermo-Electron Nicolet 6700 FTIR optical spectrometer with a DTGS KBr detector at a resolution of 2 cm^{-1} .

Nonlinear Optical Measurements with the z-scan Technique: In this method a single beam is used for measuring optical nonlinearities, which offers simplicity as well as high sensitivity [97]. The z-scan experimental set up is shown in figure 2.3. Using this set up the transmittance of a nonlinear medium is measured through a finite aperture in the far field as a function of the sample position z measured with respect to the focal plane.

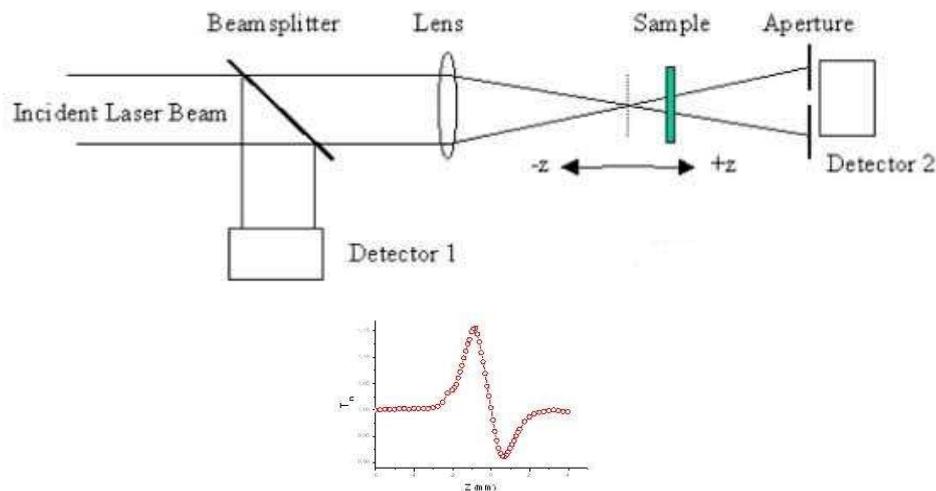


Figure 2.3. The z-scan method

As an example, assume a material with a negative nonlinear refractive index and a thickness smaller than the diffraction length of the focused beam (thin medium). This can be regarded as a thin lens of variable focal length. Starting the scan from a distance far away from the focus (negative z), the beam irradiance is low and negligible nonlinear refraction occurs, hence, the transmittance ($D2/D1$, see figure 2.3) remains relatively constant. As the sample is brought closer to the focus, the beam irradiance

increases, leading to self-lensing in the sample. A negative self-lensing prior to focus will tend to collimate the beam, causing a beam narrowing at the aperture which results in an increase in the measured transmittance. As the scan in z continues and the sample passes the focal plane to the right (positive z), the same self defocusing increases the beam divergence, leading to beam broadening at the aperture, and thus a decrease in transmittance. This suggests that there is a null as the sample crosses the focal plane. This is analogous to placing a thin lens, at or near the focus, resulting in a minimal change of the far field pattern of the beam. The z -scan is completed as the sample is moved away from focus (positive z) such that the transmittance becomes linear since the irradiance is again low [98].

A prefocal transmittance maximum (peak) followed by a postfocal transmittance minimum (valley) is, therefore, the z -scan signature of a negative refractive nonlinearity. Positive nonlinear refraction, following the same analogy, gives rise to an opposite valley-peak configuration.

In a z -scan experiment the laser beam must be Gaussian (TEM₀₀). Then the intensity profile of the beam will have a Gaussian distribution

$$I(r, t) = I_0 \frac{w_0^2}{w(z)^2} e^{-\frac{2r^2}{w(z)^2}} \quad (2.1)$$

where, $w(z)^2 = w_0^2(1 + \frac{z^2}{z_0^2})$, is the beam radius, $z_0 = k \frac{w_0^2}{2}$, is the diffraction length of the beam, $r = \sqrt{x^2 + y^2}$ is the distance of the point to the center of the beam, $k = \frac{2\pi}{\lambda}$ the wave vector and λ is the laser wavelength.

There is a phase change due to nonlinear refractive index. This phase shift which follows the radial variation of the incident irradiance at a given position of the sample z , is given by

$$\Delta\varphi(r, z, t) = \frac{\Delta\varphi_0(t)}{1 + \frac{z^2}{z_0^2}} \exp[-\frac{2r^2}{w(z)^2}] \quad (2.2)$$

with

$$\Delta\varphi_0(t) = \frac{2\pi}{\lambda} \Delta n_o(t) \frac{1 - e^{-\alpha L}}{\alpha} \quad (2.3)$$

where, L is the sample length, α the linear absorption coefficient and $\Delta n_o = n_2 I_o(t)$, with $I_o(t)$ being the on axis irradiance (i.e., $z = 0$). The phase change of the optical wave inside the medium is proportional to the refractive index. With some reasonable

approximations (such as thin sample, small phase distortion), one can derive the normalized transmittance of the closed-aperture z-scan:

$$T(z, \Delta\varphi_o) \cong 1 - \frac{4\Delta\varphi_o x}{(x^2+9)(x^2+1)} \quad (2.4)$$

where, $x = \frac{z}{z_o}$

In the above figure describing the z-scan, one must bear in mind that a purely refractive nonlinearity was considered assuming that no absorptive nonlinearities (such as multiphoton or saturation absorption) are present. Qualitatively, multiphoton absorption suppresses the peak and enhances the valley, while saturation produces the opposite effect. The sensitivity to nonlinear refraction is entirely due to the aperture, and removal of the aperture eliminates the effect. Nonlinear absorption coefficients can be extracted from such “open” aperture experiments. If this is the case, the nonlinear refraction can be also measured in the presence of a nonlinear absorption. This can be done by a simple division of the curves obtained from the two open and closed aperture z-scans. This gives a curve that closely approximates what would be obtained with a closed aperture z-scan on a material having the same Δn but with zero nonlinear absorption. This greatly simplifies determining Δn .

The nonlinear absorption of vanadium propoxide was investigated using the z-scan technique. The laser source used is a regenerative Ti:Sapphire amplifier (Tsunami, Spectra-Physics), operating at 800 nm, with <250 fs pulses and repetition rate 1 kHz. The laser beam was focused with a 10 mm lens into 3:7 molar VOTIP/MAPTMS solution (0.5 M in 1-propanol) in a 1 mm cuvette. The sample was moved with motorized stages along the beam propagation axis, and the light transmittance was measured with a photodetector (DET100A, Thorlabs). The same photodetector was installed before the sample, and a part of the beam was reflected to it with the beam splitter; it was used as a reference photodetector in order to minimize the effect of laser output fluctuations. Sample movement, correction of laser energy fluctuations, and data collection were automated using a custom-made LabVIEW software.

2.2.5 3D Structure fabrication

The experimental setup used for the fabrication of the 3D microstructures by multi-photon polymerization is shown in Figure 2.4.

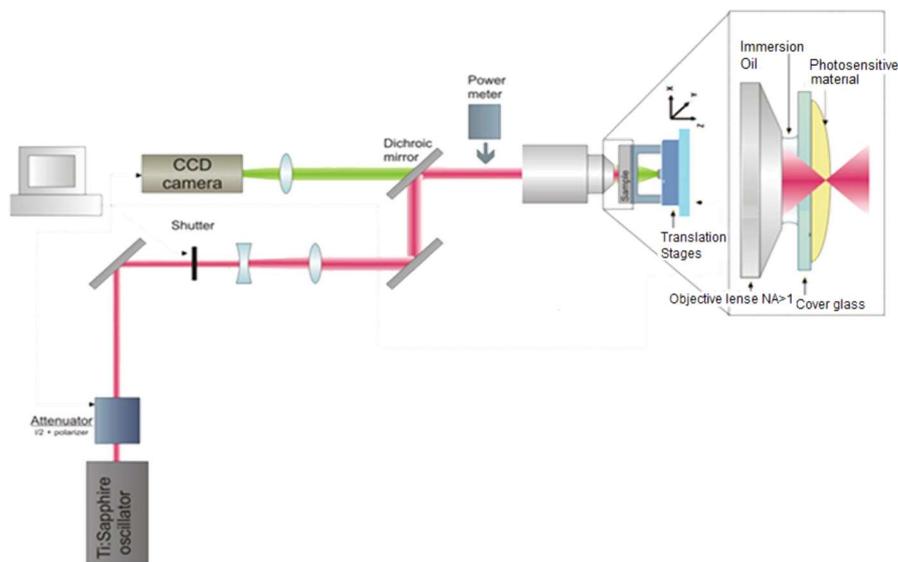


Figure 2.4. Experimental set-up for 2PP

The laser source was a Ti:Sapphire femtosecond oscillator operating at 800 nm. The laser pulse length was less than 20 fs with a repetition rate of 50-80 MHz. A 100X, 1.4 N.A, microscope objective lens was used to focus the laser beam into the volume of the photosensitive material. The photopolymerized structure was generated in a layer by layer process, using x-y-z piezoelectric stages (PI), controlled by 3Dpoli software. Large scale movement was achieved using a high resolution linear stage. Beam control was achieved by using a fast mechanical shutter, while beam intensity control was achieved using a combination of neutral density filters and a motorized polarizer analyser system (Altechna) waveplate. The online monitoring of the photopolymerization was achieved with a CCD camera, mounted behind a dichroic mirror. As the refractive index of the material changes during polymerization, the illuminated structure becomes visible during the fabrication process.

The average power needed for the fabrication of high quality 3D structures was 1–5 mW, measured before the objective, and the scanning velocity was 20 $\mu\text{m}/\text{s}$.

The 3D structures fabricated are woodpile photonic crystals and are described in detail in section 1.4.4, figure 1.22.

2.3 Results and Discussion

In the current study, a hybrid material containing vanadium (V) triisopropoxide oxide [VO(Oi-Pr)₃] has been synthesized via the sol-gel process that has the ability of accurate structuring without the addition of a photoinitiator. The process relies on the self-generation of radicals by light induced intramolecular redox initiation. Aliwi *et al.* has reported that vanadium(V) chelates that carry alkyloxy groups show photochemical activity at wavelength of 365 nm in the photoinitiation of free radical polymerization[93]. Alkyl orthovanadates [VO(OR)₃] are also photochemically decomposed via homolytic scission of the V-OR bond when exposed to UV light [99], [100]. The above processes resulted in the formation of “alkyloxy” radicals that act as the initiators of the polymerization accompanied by reduction of vanadium(V) to vanadium(IV) species. The same principle that is valid for one photon ($\lambda=365$ nm) photodecomposition, is also valid here for the two-photon ($\lambda=800$ nm) process (figure 2.5).

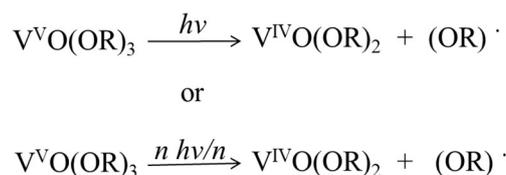


Figure 2.5. Photodecomposition scheme of alkyl vanadates by single or multi-photon absorption

During the condensation step of the sol-gel process, not all the alkyloxy groups of the vanadium complex condense to form the network leading to polymeric alkoxo-oxides, but a number of alkoxy ligands remain bound to the oxide network [101]. When these groups are present, gels tend to obtain an orange color, which is characteristic of these polymeric alkoxo-oxides. After light irradiation, where vanadium (V) is reduced to vanadium(IV) these gels turn green, a characteristic color of vanadium (IV) species [102]. Figure 2.5 shows thin films of the synthesized hybrid material before and after polymerization. It is apparent that the material before polymerization has an orange color, which indicates the existence of alkyloxy groups in the material, which upon UV irradiation can create free radicals. After polymerization the material's color turns green indicating the elimination of these groups from the vanadium atom and its reduction to vanadium (IV).

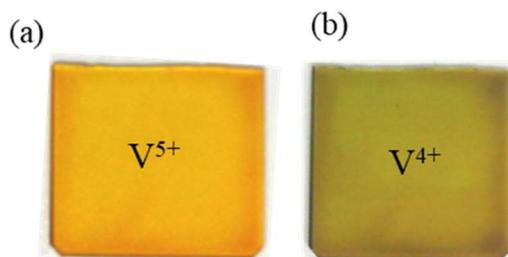


Figure 2.5. Thin films of the vanadium hybrid material (a) before and (b) after the single photon (360 nm) polymerization process.

The vanadium triisopropoxide oxide precursor, used for the synthesis of our material, is widely used for the synthesis of vanadium pentoxide (V₂O₅) inorganic gels. Vanadium pentoxide gels, become crystalline by following the appropriate synthetic route. It is a fact though, that when the alkyloxy ligands are not totally removed during the formation of the gel, the resultant material becomes amorphous [102]. In order to investigate if the vanadium inorganic network formed in our hybrid material exhibits crystalline or amorphous structure, XRD measurements were carried out on thin films of the material before the polymerization process. Figure 2.6 shows the XRD spectrum recorded. A broad peak is located between 15 and 37 2θ degrees, characteristic of an amorphous material. This result, confirmed the existence of the alkyloxy groups in our material.

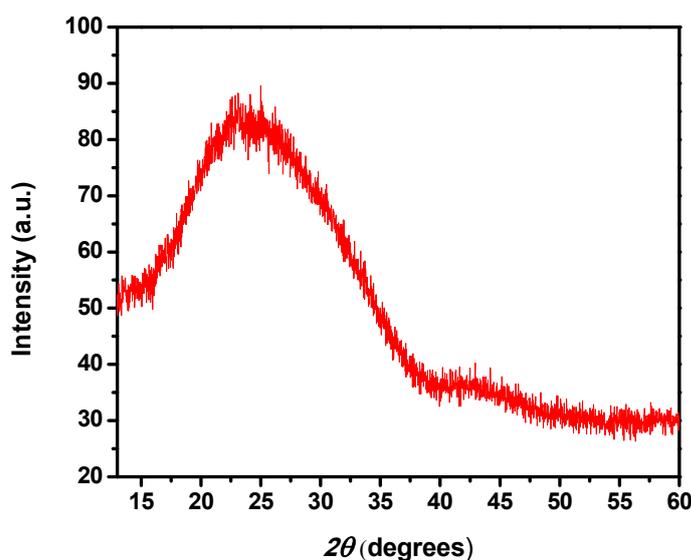


Figure 2.6. XRD spectrum of the vanadium hybrid material. The main broad peak indicates the amorphous structure of the vanadium hybrid material.

The UV/vis spectra of the 50% vanadium containing hybrid material were recorded on thin films. The spectra involve the absorption of a thin film of the hybrid material after drying in vacuum, and before light irradiation, and the absorption of the same film after light irradiation. In figure 2.7 the recorded spectra are depicted. In both cases, the material starts to absorb below 600 nm. After light irradiation, when the photopolymerization has taken place, a decrease in the absorbance is observed, more pronounced in the 350–400 nm region. This is attributed to the consumption of the V–OR bonds that absorb in this region, leading to their cleavage, and the subsequent reduction of vanadium (V) to vanadium (IV) with the concomitant formation of the alkyloxy radicals. It is also worth mentioning here that as the material is transparent above 600 nm, it is suitable for DLW using a lasers operating above this wavelength.

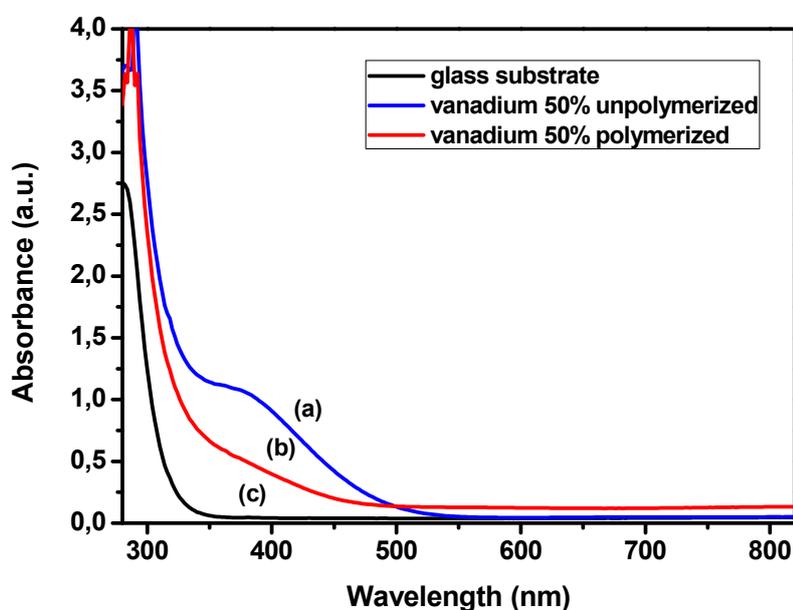


Figure 2.7. UV/vis absorption spectra of a thin film of the vanadium hybrid material (a) before photopolymerization and (b) after photopolymerization. (c) Absorption spectrum of the glass substrate.

Figure 2.8 shows the FT-IR spectra taken on thin films of the material before and after the polymerization process. The spectra look almost identical with the only major difference being the disappearance of the peak located at 1165 cm^{-1} which corresponds to the V–O–C vibration [103]. This result verifies the scission of the V–OR bond after light irradiation of the films.

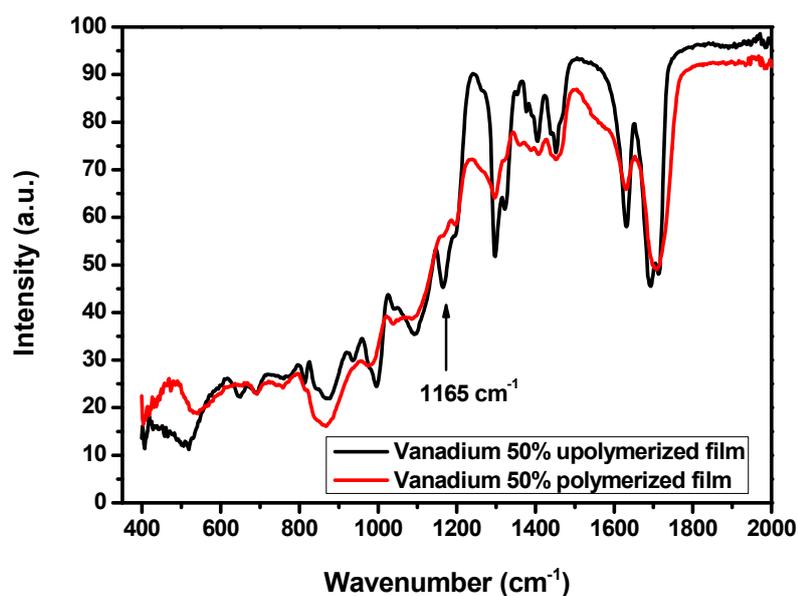


Figure 2.8. FTIR spectra of thin films of the material. The black line corresponds to the film before polymerization and the red line to the same film after the polymerization process.

For the 3D structure fabrication, the woodpile photonic crystal geometry was chosen [104]. The reason was that this specific structure has been widely used and characterized; due to its geometry of parallel rods, which are formed by single scanning of the laser beam through the volume of the material, it makes it a perfect candidate for the investigation of the structuring ability of the material. Moreover, this 3D structure allows us to compare the material structurability and resolution with our previous results, and those reported in the literature, using DLW [105], [106]. Figure 2.9 shows different views of one of the fabricated structures. It is a woodpile structure with dimensions $30 \times 30 \mu\text{m}$, period $1.1 \mu\text{m}$, consisting of 24 layers. The material used in this case was a 1:1 VOTIP:MAPTMS mole ratio. It can be seen that the material can be structured accurately, without distortion with a lateral resolution of approximately 200 nm. This was the highest VOTIP content that could result in good quality, high resolution structures. When lower concentrations of VOTIP were used (up to 1:9), the structures appeared similar and had similar resolution. Figure 2.10 shows representative SEM images of structures at a 1:9 and 3:7 VOTIP:MAPTMS molar ratio. In all cases, the material after polymerization resembled a hard glass. The structures remained mechanically stable and showed no sign of degradation for several weeks. VOTIP contents above 50%, resulted in a very hard material after the condensation step, since

the inorganic ratio was increased. However, this prohibited the efficient development of the material to reveal the 3D structures.

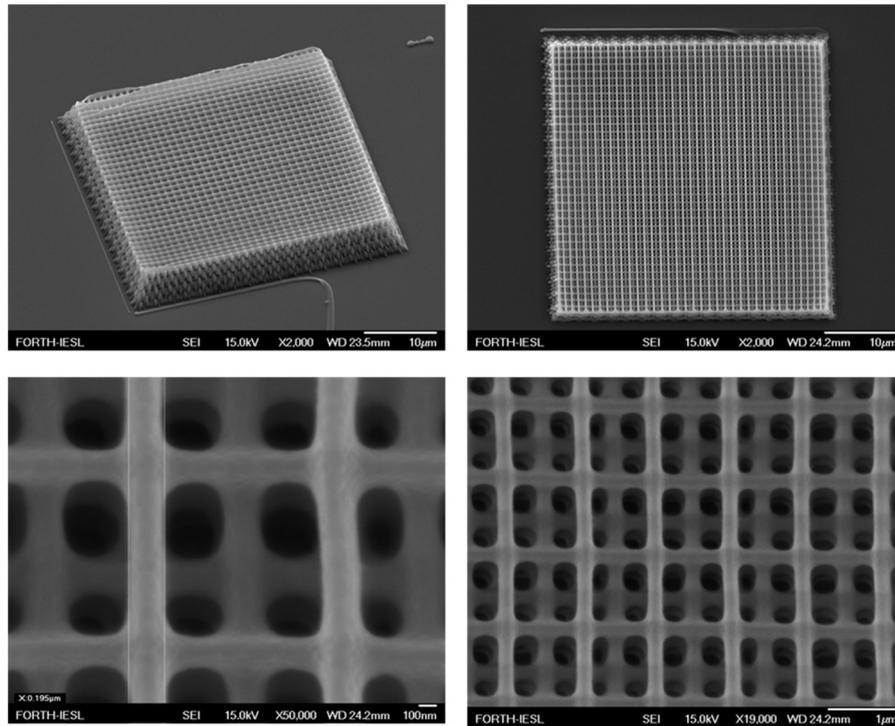


Figure 2.9. Different views of a woodpile structure fabricated using the vanadium composite material.

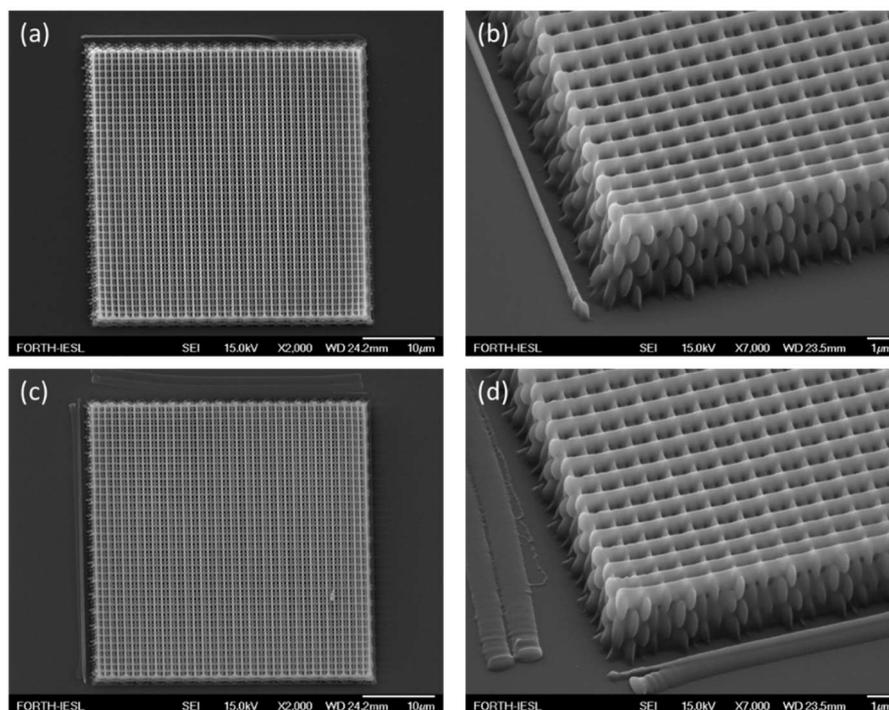


Figure 2.10. (a) and (b) woodpile structures fabricated from the 3:7 VOTIP:MAPTMS molar ratio material; (c) and (d) same structure fabricated from the 1:9 VOTIP:MAPTMS molar ratio material.

In order to verify whether the polymerization is due to a nonlinear phenomenon or other light-induced processes such as avalanche electron generation [107], nonlinear absorption measurements were carried out using the z-scan technique [108]. The z-scan technique is based on the measurement of the transmittance when a focused laser beam passes through a sample of nonlinear media. The sample is translated along the axis of the focused beam. When approaching the waist of the beam, the intensity is at a maximum. If the nonlinear absorption threshold is exceeded, the sample exhibits multiphoton absorption and a decrease in light transmittance can be observed, depending on the sample position with respect to the waist of the beam. By fitting the transmittance versus the sample position, the multiphoton absorption cross-section can be extracted. If the dominant process is two-photon absorption, the z-scan transmittance can be expressed as [108]:

$$T(Z) = \sum_{n=0}^{\infty} \frac{(-q_0)^n}{(n+1)^{3/2}(1+x^2)^n} \quad (1)$$

If the dominant process is three-photon absorption, then the z-scan transmittance can be expressed as [109], [110]:

$$T(Z) = \sum_{m=0}^{\infty} \frac{(-P_0^2)^m}{(2m)!(2m+1)^{3/2}(1+x^2)^{2m}} \quad (2)$$

Where, $P_0^2 = I_0^2 L_{eff} 2N_A p \times \frac{10^{-3} \sigma_3 \lambda^2}{(hc)^2}$ and σ_3 is the three-photon absorption cross-section.

Figure 2.11 shows a plot of the normalized laser transmitted intensity vs. the sample position. The material used is a 3:7 molar VOTIP:MAPTMS solution in 1-propanol (0.5 M).

It should be pointed out that two different lasers were used for the photopolymerization and the z-scan measurements: a Ti:Sapphire oscillator and a regenerative Ti:Sapphire amplifier, respectively. When the experimental conditions are taken into account, it can be calculated that the photon flux density is similar in both cases and of the order of 10^{29} photons/s·cm². This indicates that third order transition probabilities are the same for DLW and z-scan.

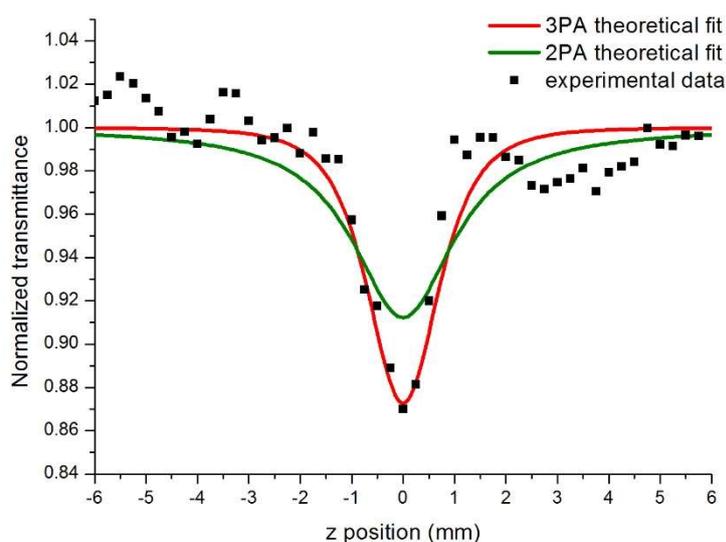


Figure 2.11. Z-scan measurements of nonlinear absorption for the vanadium propoxide

By fitting the data to eq. 2, we can calculate the value of the three-photon absorption cross-section of vanadium propoxide, which was found $\sigma_3 = 3.0 \times 10^{-80} \text{ cm}^6 \cdot \text{s}^2$. This value is comparable to that of several third-order nonlinear organic molecules (10^{-80} – $10^{-79} \text{ cm}^6 \cdot \text{s}^2$) [111], [112]; however, it is four orders of magnitude lower than the cross-sections ($10^{-76} \text{ cm}^6 \cdot \text{s}^2$) of some novel fluorene or stilbazolium derivatives used in optical limiting [113], [114]. It is worth mentioning, however, that these materials are used as dopants, at 1–2% content, above which there is saturation, while we were able to make a photopolymer containing up to 50 mol % VOTIP with respect to MAPTMS.

Figure 2.12 shows the laser power required for the polymerization of the vanadium composite material vs. its VOTIP content. The power was measured before the objective (average transmission 20%). The threshold energy was defined as the minimum laser power required for the fabrication of a complete woodpile structure, similar to the ones of figures 2.9 and 2.10. It is clear that the power required decreases linearly with the VOTIP content and starts saturating at VOTIP molar content above 30%. In comparison, a typical photoinitiator will stop affecting the required laser power at 1–3%. The minimum power required for the multiphoton polymerization at 50% VOTIP molar content is 1.2 mW.

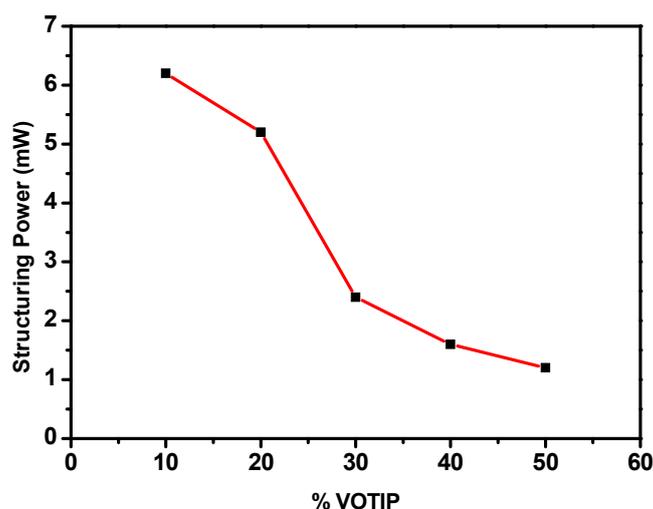


Figure 2.12. Minimum laser power required for the multiphoton polymerization of the vanadium composite material *vs.* the VOTIP content (moles).

In comparison, the power required to polymerize the composite material described in ref [115] with 1% photoinitiator, under exactly the same experimental conditions, is 2.8 mW. In the latter case, however, the photoinitiator used (Michler's ketone, 4,4-bis(diethylamino) benzophenone) is a two-photon absorber. Therefore, our three-photon structuring of the VOTIP composite material (a third order process) has comparable efficiency to the two-photon efficiency of standard composites (a second order process).

2.4 Conclusions

Alkyl orthovanadates $[\text{VO}(\text{OR})_3]$ are photochemically decomposed via homolytic cleavage of the V-OR bonds when exposed to UV light. This results in the reduction of vanadium (V) to vanadium (IV) and the simultaneous production of alkyloxy radicals that can act as initiating sites for free-radical polymerization. In the current work, we have shown that this VOR bond scission can be also induced using multiphoton absorption. We have thus employed a vanadium alkoxide compound at loadings as high as 50 mol % as both the photoinitiator and one of the components of our hybrid material, for the construction of 3D nanostructures. This high vanadium alkoxide loading leads to the high efficiency of the three-photon polymerization process, of this composite

being comparable to the two-photon polymerization efficiency of other composites, in which typically 1–2% photoinitiator is added.

Nowadays it is possible to obtain ultrashort pulse lasers operating at different wavelengths, which have been employed also in DLW [116]. Because of the high vanadium loading of our material, it is possible that the two-photon DLW efficiency of this composite using the appropriate laser will be very high. However, without a comprehensive study of the transitions involved, it is not possible to predict if this is indeed the case, and what would be a possible two-photon wavelength.

Photopolymerization in the absence of an added photoinitiator has been previously reported by Malinauskas et al. [107] However, in that case the phenomenon was quite different. Very high intensities from an amplified picosecond laser were employed to induce avalanche electron generation, which subsequently caused the polymerization of the material. This was not specific to the material used. In the case described here, the z-scan measurements clearly indicate that the observed process is a nonlinear effect, and the laser power required is only a few mWs.

To conclude, we have demonstrated for the first time the redox multiphoton polymerization of a material, in which a vanadium alkoxide complex acts as both the photoinitiator and as one of the components of the organic–inorganic composite. The material self-generates radicals by multiphoton absorption, accompanied by a simultaneous reduction of vanadium (V) to vanadium (IV). We have used this material to make fully 3D structures with 200 nm resolution employing a femtosecond laser operating at 800 nm. In addition, we have carried out nonlinear optical measurements, and we have shown that the photoinitiation is most likely due to three-photon absorption of the vanadium species. The three-photon absorption coefficient of the material was found to be $\sigma_3 = 3.0 \times 10^{-80} \text{ cm}^6 \cdot \text{s}^2$, comparable to those of standard three-photon absorbers. Since it is possible, however, to load the composite with as much as 50 mole% vanadium complex, the efficiency of the three-photon polymerization process of the investigated composite is comparable to that of a two-photon polymerization of other standard materials containing less photoinitiator. In addition, using a different wavelength laser, as mentioned earlier, one could explore the two-photon dominant process and a commensurate increase in the efficiency of the polymerization. This, coupled with the high loadings of the vanadium isopropoxide should push the efficiency of 2PP higher than has been possible in the past.

CHAPTER 3: Active three-dimensional woodpile photonic crystal structures tuned for the visible light

Active 3D photonic devices were fabricated by combining Direct Laser Writing (DLW) and two-photon absorption with the in-situ synthesis of cadmium sulfide (CdS) nanoparticles within the hybrid matrix. The novel active 3D structures are based on an organic-inorganic zirconium-silicon hybrid material exhibiting a high $\chi^{(3)}$ nonlinearity and bearing a Cd precursor for the in-situ formation of the CdS nanoparticles. As a proof-of-principle, active 3D woodpile photonic crystals with an inlayer periodicity as low as 500 nm, exhibiting high resolution and clear photonic stop bands in the visible spectral region were successfully fabricated, while for the first time, evidence of ultrafast dynamic tuning of the photonic band gap properties in the visible range, is demonstrated.

3.1 Introduction

The design of responsive materials allowing to dynamically tune their photonic properties has been a subject of intense research during the last decade, due to their potential applications in all optical switching devices used in active photonic integrated circuits. A significant modification of the light-matter interaction can be achieved, for example, by the incorporation of quantum dot (QD) semiconductor nanocrystals in a photonic polymer matrix, since the energy of the band-to-band transitions of the semiconductor nanoparticles (NPs) embedded in the material, can overlap with the photonic band gap region [117], [118]. Composites consisting of nano-sized particles incorporated in a polymer matrix are of great interest due to their long-term stability offering new strategies for influencing the interactions that may take place between the matrix and the NPs. These composites are promising materials for a new generation of optical and electronic devices, as well as for biological labelling [119]–[121].

One way to implement an all-optical switching photonic device is based on a Kerr-type nonlinearity, that is, the refractive index of one of the materials embedded in the photonic matrix depends on the local intensity of light and, hence, the material exhibits a band structure that changes dynamically with light. In order to achieve high intensity contrast between the “on” and “off” states of the optical switch, a high nonlinear Kerr

coefficient is required along with a narrow resonance of the photonic switch. In addition, a well confined light source in the three dimensions is also highly desirable for complete control over the photonic density of states. Nanocrystal QDs are well known for their large third-order non-linearity arising from the quantum size effect [122]. Due to the existence of a complete photonic band gap [81], [123], [124], 3D photonic crystals provide a unique tailored dielectric platform by which the active properties of embedded QDs can be well controlled.

Although many novel photonic devices comprising 3D photonic crystals have been previously proposed [125], (e.g., opals, inverse opals, woodpile) it has been a challenge to experimentally incorporate QDs within 3D photonic crystal lattices and realize devices with demonstrable functionalities on the basis of a single-step processing with the ability to preserve the active materials properties. Self-assembly [126] and inversion [127] methods in combination with post-fabrication infiltration [128], as well as patterning polymeric materials with embedded quantum dots using layer by layer lithography [129] are the main approaches employed to obtain QD containing 3D periodic structures. Furthermore, the development of novel active 3D optical elements by direct patterning has been restricted mostly to the IR as QD structuring cannot reach optical-grade quality in the visible, since the dimensions of the features should be approximately $\lambda/4n$ (λ , wavelength and n , the refractive index).

On the other hand, optical lithography via direct laser writing [130] possesses the flexibility to engineer a variety of different lattice arrangements, which makes it an excellent candidate for the fabrication of intrinsic 3D devices, such as 3D photonic crystals. Several efforts have been undertaken in order to improve the resolution of direct laser written structures at the nanometer scale [131]–[133], as well as to realize functional 3D microstructures by incorporating nanocrystal QDs in the polymer resin [14], [134]–[138]. In DLW, usually either the NPs are combined with pure organic materials lacking structural stability due to shrinkage [115], [138], and, hence, restricting functionality mostly to the IR region, or the particles are dispersed in commercially available photoresists that wash out during the development process as they are not part of the photopolymer [14], [137]. In addition, segregation of the NPs during polymerization causes the photosensitive resin to become opaque, thus eliminating the possibility to fabricate 3D microstructures [137].

Nevertheless, these phenomena can be overcome by the appropriate functionalization of the QDs [134]. Therefore, in the present work, in order to avoid absorption and

scattering due to the aggregation of the NPs, we choose the in situ synthesis of semiconductor QDs within the 3D polymer photonic matrix, following DLW fabrication of the 3D structures. The QDs were prepared by polymerizing appropriate QD precursor molecules in a photo-patternable polymer resin. The latter is an organic-inorganic hybrid composite material synthesized via the sol-gel process [139], a versatile technique that has been exploited for the incorporation of inorganic networks into polymer matrices using as monomers molecules that carry an inorganic moiety and a polymerizable organic group. The former serves as the precursor to the inorganic network, whereas the latter acts as the precursor to the organic polymer. Upon the appropriate selection of the most suitable functionalities, from an enormous variety of precursor molecules, this technique offers the possibility to alter the composite material properties. The novel active photo-structurable material presented herein allows, on one hand, the homogeneous incorporation of QDs in the crosslinked polymer matrix and, on the other, combines the properties of its constituent components enabling the fabrication of 3D active devices on a small scale exhibiting high spatial resolution and negligible shrinkage [115], [131], [140].

Of direct relevance to the implementation of an all-optical switching photonic device, we show herein how the two-in-one functional properties of a novel active 3D printable hybrid material – namely high spatial resolution and high $\chi(3)$ nonlinear response, can be effectively utilized, first, to realize the visible light photonic band gap properties of the 3D woodpile photonic devices, evidenced by the existence of pronounced stop-bands clearly visible as a dip in transmission and an overlapped peak in the reflection spectra and, second, to demonstrate, for the first time, evidence of ultrafast dynamic tuning of the photonic band gap properties in the visible.

3.2 Experimental

3.2.1 Material synthesis

The material was prepared using methacryloxypropyltrimethoxysilane (MAPTMS, Sigma-Aldrich), Cadmium methacrylate $\text{Cd}(\text{MA})_2$, 2-(dimethylamino)ethyl methacrylate (DMAEMA, Sigma-Aldrich) and methacrylic acid (MAA, Sigma-Aldrich). Zirconium propoxide $\text{Zr}(\text{OPr})_4$, (ZPO, 70% solution in 1-propanol, Sigma-

Aldrich) was used as an inorganic network former. All chemicals were used without further purification.

The precursors used are metal alkoxide molecules and organic and hybrid monomers. For the formation of the inorganic network zirconium propoxide was used. Methacryloxypropyltrimethoxysilane (MAPTMS), 2-(dimethylamino)ethyl methacrylate (DMAEMA) and methacrylic acid (MAA) served as the hybrid and organic monomers. MAPTMS carries a trialkoxysilane functional group, which undergoes hydrolysis and condensation and is thus attached to the inorganic network and a polymerizable methacrylate moiety, which contributes to the formation of the organic matrix. Cadmium methacrylate $[\text{Cd}(\text{MAA})_2]$ was used as the precursor for the formation of the CdS nanoparticles. 4,4' – Bis(diethylamino) benzophenone (BIS) was employed as the photoinitiator. Figure 3.1 shows the chemical structures of the material building blocks.

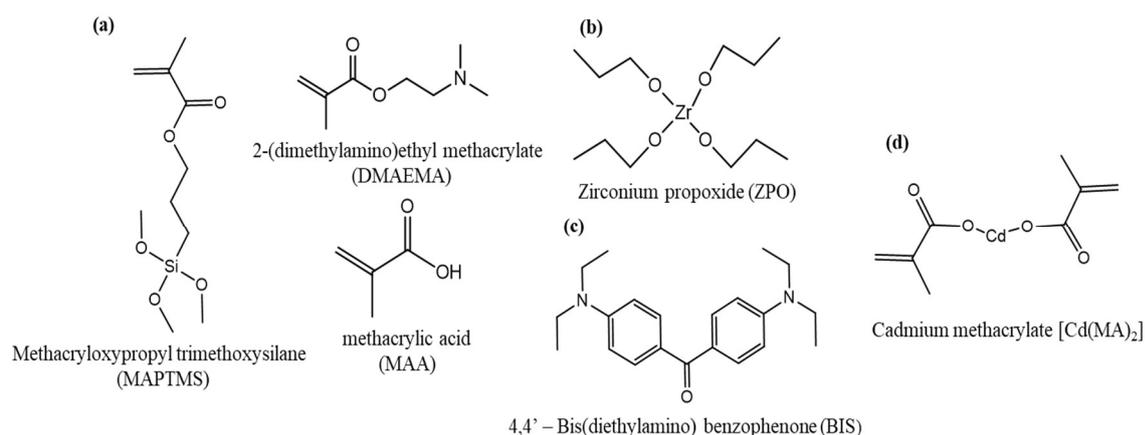


Figure 3.1. Chemical structures of the molecules used for the synthesis of the hybrid material.

(a) Organic and hybrid monomers (b) metal alkoxides (c) photoinitiator (d) quantum dot precursor.

First, $\text{Cd}(\text{MA})_2$ was synthesized by modifying the procedure reported previously by Sun et al. [141]: Cadmium oxide (CdO , Sigma-Aldrich) was added in portions in a flask, containing MAA and 1,5 ml of ethanol at room temperature. The molar ratio of CdO to MAA was 1:2. Subsequently the mixture was stirred for 24 hours and the desired product was obtained (figure 3.2).

Next, MAPTMS at a 8:2 molar ratio to ZPO, was hydrolyzed by the addition of HCl (concentration 0.1 M) and the mixture was stirred for 15 minutes. In a separate flask, ZPO was chelated by adding MAA at a 1:1 molar ratio. The solution was stirred for 20 minutes. The hydrolyzed MAPTMS was then added dropwise to the ZPO solution, following another 20 minutes of stirring. DMAEMA was added, at a 30% molar ratio with respect to MAPTMS and MAA. The mixture was stirred for 5 mins, following the subsequent addition of a small amount of nanopure water. Next, Cd(MA)₂ was added to the flask at a 1:1 molar ratio with respect to ZPO. The mixture was stirred for 30 minutes. BIS (Sigma-Aldrich), 1% w/w to the monomers, was used as the photoinitiator. After stirring for 30 minutes, the material was filtered using a 0.45 µm pore size filter. Figure 3.3 shows the reactions which take place for the synthesis of the hybrid material.

3.2.2 Sample preparation

Before the formation of the samples on glass substrates the latter were silanised following a two-step procedure described below. First, a mixture of ammonium hydroxide (NH₄OH) solution (28% w/w) was mixed with hydrogen peroxide (H₂O₂) solution (35% w/w) at a 3:1 volume ratio. Then, the glass substrates were immersed in the NH₄OH/H₂O₂ solution with both sides facing the liquid mixture. Subsequently, the solution was heated to 75 °C for 30 mins. This process leads to the effective cleaning of the surface of the substrates from any organic residue (dirt) and to the increase of the surface density of the silanol groups on the glass substrate. Finally, the substrates were rinsed thoroughly with deionized water and were dried under a nitrogen flow. In the second step, the clean substrates were immersed in a mixture of toluene and MAPTMS at a 0.2 % v/v, with both sides exposed to the mixture. The substrates were left in the MAPTMS solution overnight to ensure the formation of a dense layer of MAPTMS on the surface obtained by the reaction of the surface silanol groups with the methoxysilane groups of MAPTMS.

Samples were prepared by either spin coating a thin film of the material onto pre-silanized square microscope glass substrates, used for the material characterization studies, or by drop casting the hybrid material onto 100 µm-thick round silanized glass

substrates for use in 3D microfabrication. The resultant films/drops were dried under vacuum at ambient temperature for three days before the photopolymerization. The drying process led to the condensation of the alkoxide groups and the formation of the inorganic network, and to any volume loss of the material due to evaporation of traces of solvents produced by the condensation process. Next, the samples were exposed to UV (360 nm) or laser (800 nm) irradiation to fabricate the films for the material characterization or the 3D structures, respectively. After the irradiation process, the non-polymerized material, was removed by developing the samples sequentially in 4-methyl-2-pentanone, 2-propanol and dimethyl sulfoxide (DMSO). Following the development process, the samples were immersed in a sodium sulfide (Na_2S) solution in water for 6 hours to form the CdS QDs and pale yellow nanocomposites were obtained. Finally, the samples were rinsed several times with nanopure water and were allowed to dry in air at room temperature.

3.2.3 Characterization of the CdS quantum dot hybrid material and the 3D structures

For the characterization of the hybrid material, thin films were prepared (section 3.2.2) on glass microscope slides. The spectroscopic techniques used for the characterization of the material involve UV-Visible spectroscopy, X-ray diffraction (XRD) spectroscopy and the z-scan technique.

UV-Visible spectroscopy: the absorption spectra of thin films of the material were recorded in the 250-820 nm spectral range using a Perking Elmer Lambda 950 UV-VIS spectrometer.

XRD spectroscopy: X-ray diffraction studies were carried out on thin films prepared as described above. A Rigaku RINT 2000 Series wide-angle diffractometer was used for the measurements.

z-scan: The nonlinear absorption of the Zr-CdS composite material was investigated using the z-scan technique. The laser source employed is a regenerative Ti:Sapphire amplifier (Tsunami, SpectraPhysics), operating at 800 nm, with < 250 fs pulse width and 1 kHz repetition rate. The laser beam was focused with a 10 cm lens onto a thin polymeric film of the quantum dot containing material and the sample was moved with motorized stages along the beam propagation axis. The light transmittance was

measured with a photodetector (DET100A, Thorlabs). The same photodetector was installed before the sample, and a part of the beam was reflected onto it with a beam splitter, and acted as a reference photodetector in order to minimize the effect of laser output fluctuations. Sample movement, correction of laser energy fluctuations, and data collection were automated using a custom-made LabVIEW software. Detailed information about the z-scan technique can be found in section 2.2.4.

The 3D structures were characterized by Fourier Transform Infrared (FTIR) transmittance/reflectance spectroscopy and time resolved pump-probe spectroscopy.

FTIR: FTIR transmittance/reflectance spectra were measured with a Vertex 80 spectrometer coupled to a Hyperion 2000 IR microscope (Bruker Optics) equipped with Cassegrain objectives (15 \times , 36 \times) and a liquid nitrogen cooled mercury cadmium telluride detector.

Time resolved pump-probe spectroscopy: Pump-probe time-resolved transmission measurements are recorded by employing an amplified femtosecond Ti-Sapphire laser operating at 795 nm, with a pump pulse duration of ~ 30 fs, a pulse repetition rate of 1 kHz and pulse energy amplified to ~ 1 mJ per pulse. At the exit of the amplifier, the laser beam splits into two arms; one arm serves as a weak probe beam, and the other one as a pump beam. The probe beam is tightly focused within a quartz cuvette filled with distilled water in order to generate a white light supercontinuum source via optical rectification and plasma [142], [143], providing a broad spectral wavelength range from 440 nm to 720 nm. The supercontinuum pulses, after propagating through a telescope, in order to maintain beam collimation, are guided to a delay line which enables control of the length of the probe arm. This change of optical path sets the relative time delay (Δt) between pump and probe pulses. The white light probe beam further splits into two arms by a beam splitter; one arm serves as the probe Signal and the other one as the probe Reference. The probe Signal is focused by a lens into a 25 μm spot at the sample surface, whereas the latter is vertically displaced and focused by a similar lens to an unperturbed area on the sample. The sample holder is mounted on top of a rotation stage, so that the sample can be rotated by an angle with respect to the optical axis, while the whole combination is mounted on top of a three-dimensional translational stage in order to align the sample relative to the focus. The light is coupled out and collected by a lens at the entrance of the detection system, which consists of a monochromator with a CCD camera mounted at its exit. The sample plane is also inspected with a camera system in order to ensure that the light collected has passed

through the desired woodpile structure sitting on the sample. Incident fluence is calculated by recording both beam profiles at the focal plane of the probe beam by use of a CCD camera. Note that the size of the pump beam focus is much larger ($\sim 180 \mu\text{m}$) than that of the probe beam, thus achieving homogeneous excitation of the probed sample area.

The Optical Density (OD) of the transient absorption is extracted from measurements of the transient spectra calculated as the ratio of the probe pulse intensity being transmitted through an unperturbed sample area (probe Reference, $I_{\text{Ref}}(v)$) and that collected from a perturbed sample area (probe Signal, $I_{\text{Sig}}(v)$) four times prior to and after excitation by the pump as defined in Ref. 145, page 231 [144], [145].

3.2.4 3D Microfabrication

For the 3D structure fabrication the same procedure, described in section 2.2.5, was used. Briefly, the laser source employed was a Ti:Sapphire femtosecond oscillator operating at 800 nm with a pulse length of < 20 fs and a repetition rate of 75 MHz. A 100x microscope objective lens (Zeiss, Plan Apochromat, N.A. = 1.4) was used to focus the laser beam within the volume of the photosensitive material. The writing speed employed was $20 \mu\text{m s}^{-1}$ and the peak intensity at the center of the focal point was $\sim 0.35 \text{ TW/cm}^2$. After the completion of the component building process, the samples were developed in 4-methyl-2-pentanone, 2-propanol and dimethyl sulfoxide (DMSO), for at least 30 mins in each solvent. In the present work, the woodpile geometry was chosen for the fabrication of 3D photonic devices by DLW (see section 1.4.4).

3.2.5 Theoretical Calculations

The theoretical band structure of an infinite woodpile photonic crystal with an inlayer periodicity $a = 600$ nm was calculated with the freely available MIT photonic bands (MPB) software [146]. The refractive index of the dielectric rods was set to $n = 1.52$. The cross-section of the rods was assumed for simplicity to be rectangular having the same area (rod thickness (d) x rod height (h) = $80 \text{ nm} \times 240 \text{ nm}$) as the actual elliptical rods ($120 \text{ nm} \times 360 \text{ nm}$) and preserving the $1/3 = \text{thickness/height}$ ratio (due to the objective lens) to ensure that their shape does not affect the band gap properties. In

order to simulate the transmission and reflection from the finite experimental sample of 10 unit cells, a custom Finite Difference Time Domain (FDTD) code was employed using the same geometrical parameters as before, while assuming that the structure is infinite in the inlayer plane. The discrete time and space steps were set to $\delta t = 15 \times 10^{-18}$ s and $\delta x = 10 \times 10^{-9}$ m, respectively. In order to take into account the experimental scattering losses, artificial loss (conductivity) was introduced into the dielectric rods equal to $\sigma = 3 \times 10^3$ S, corresponding to an imaginary part of ~ 0.1 for the rod permittivity.

3.3 Results and discussion

The cadmium containing hybrid material was used for the in situ synthesis of CdS quantum dots within the volume of 3D photonic crystals (woodpile geometry) as well as thin films. Thin films of the material, before and after the formation of the CdS nanoparticles, were characterized by UV-Vis, photoluminescence spectroscopy and XRD. As seen in figure 3.4, the films before the formation of the CdS quantum dots are slightly yellow and transparent. The yellowish color arises from the photoinitiator that is added in the material. After the immersion of the films in the Na_2S aqueous solution, which induces the formation of the CdS nanoparticles, and extensive rinsing steps with deionized water, a remarkable difference in the color of the films is observed. The films obtain a deep yellow color and at the same time become opaque, signifying the formation of the CdS nanoparticles.

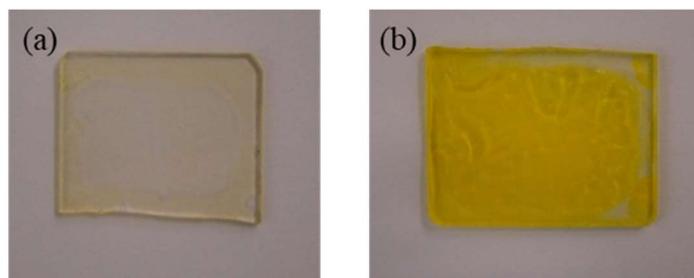


Figure 3.4. Thin films of there material on glass slides (a) before and (b) after the formation of the CdS nanoparticles

The UV-Vis absorption spectra of the samples were recorded on thin films of the material during three different stages of the final nanocomposite material synthesis and are depicted in figure 3.5. The glass substrate was also measured and was used as a reference. The first sample was the zirconium hybrid material, the second the zirconium-Cd(MA)₂ material before the formation of the CDs and the fourth film was the zirconium-Cd(MA)₂ material, after treatment with Na₂S solution, to induce the formation of the CdS quantum dots.

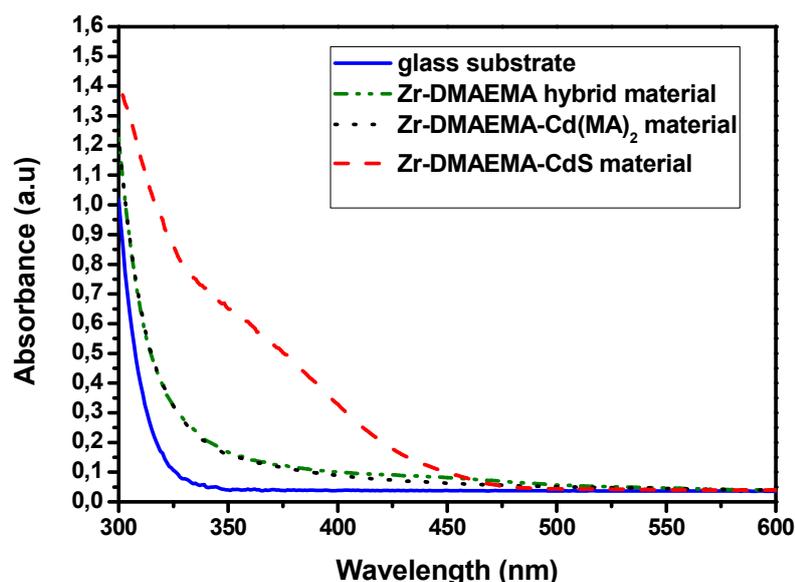


Figure 3.5. UV-Vis absorption spectra of thin films of the Zr hybrid material before the addition of Cd(MA)₂ (green dash-dotted line), in the presence of Cd(MA)₂ (black dotted line) and after the in situ synthesis of the CdS quantum dots (red dashed line). The absorption measured from the glass substrate (blue solid line) is shown as a reference.

As seen in figure 3.5, the glass substrate has no absorbance above 350 nm. The absorbance of the zirconium composite films is higher above 360 nm but negligibly different from that of the zirconium-Cd(MA)₂ material. This allows us to conclude that there is no significant effect of cadmium methacrylate on the absorption properties of the zirconium composite. On the other hand, a significant increase in absorption, above 350 nm, was observed after the formation of the CdS nanoparticles. After treatment with Na₂S a broad absorption band appeared in the film in the 350-450 nm range which corresponds to the energy transition between the electron-hole (exciton) energy levels and signifies the formation of the CdS quantum dots.

The XRD pattern of the CdS containing film was recorded and is presented in figure 3.6. The spectrum exhibits three broad peaks centered at 2θ values of 26.5, 44 and 51.8° attributed to the (111), (220) and (311) planes of cubic CdS, respectively.

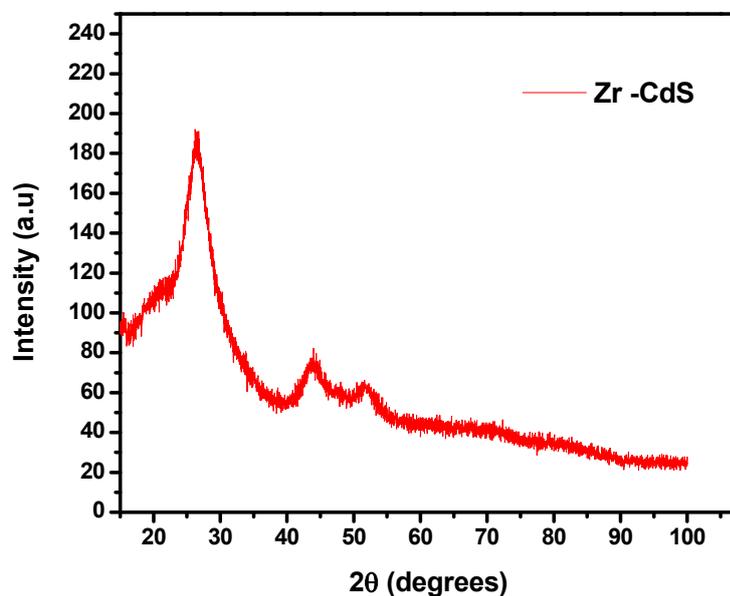


Figure 3.6. XRD pattern of the CdS containing films

Cadmium sulfide exists in nature in the form of two different minerals, hexagonal greenockite in the bulk material and cubic hawleyite in nanomaterials. It is of interest to note that a mixture of hexagonal and cubic phases is routinely observed for CdS nanoparticles. The reason for that being that the two phases have similar energy levels and the transformation from one another is most feasible. However, the particle size plays an important role in determining the crystal structure. By reducing the size, the crystal lapses into the cubic structure from the hexagonal one, for particle sizes below 5 nm [147], whereas above this size the material comprises a mixture of both phases. The hexagonal structure has three distinct and closely located peaks at $2\theta = 24^\circ$, 26° and 29° , which are quite close to the intense (111) peak of the cubic structure. In the present pattern the peak at 26.55° is symmetric and the (103) peak of the hexagonal phase at 48° is absent. This suggests that the nanoparticles prepared in the current work exhibit a cubic lattice due to their small size.

The incorporation of CdS QDs in the polymer matrix results in a novel composite material which exhibits a nonlinear refractive index value of $n_2 = 185.7 \times 10^{-15} \text{ (cm}^2/\text{W)}$ measured by means of the z-scan method [108]. The corresponding z-scan

measurements performed on a thin film of the QD containing material revealed the characteristic peak-valley trace of a $\chi^{(3)}$ non-linear material shown in figure 3.7. In particular, a positive nonlinearity is observed, since the peak-to-valley sequence was recorded as the sample translated towards the focusing lens. It is worth noting that the magnitude of n_2 measured for the novel nanocomposite presented herein is three orders of magnitude larger than the values obtained for standard solvents. Such large nonlinearities have been previously reported in similar experiments involving QDs doped nanocomposites [14], [148], [149].

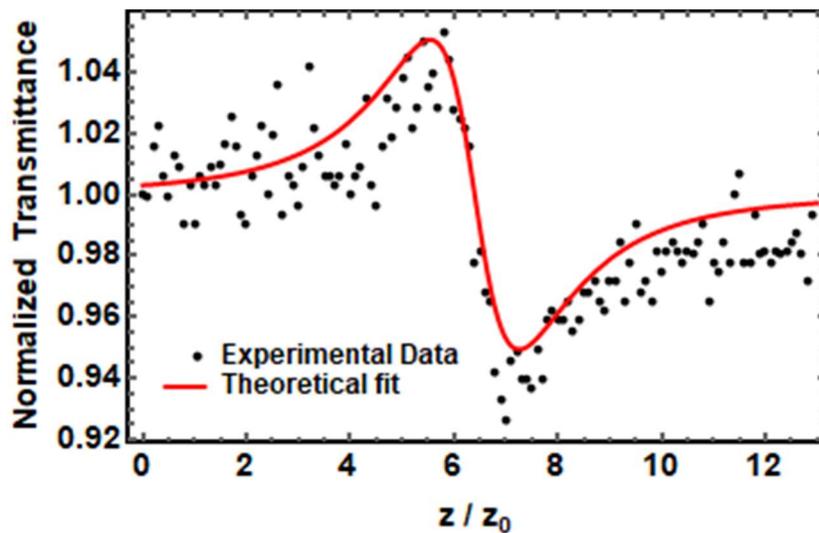


Figure 3.7. Normalized z-scan transmittance measured at 800 nm for a polymeric film doped with CdS quantum dots. The red solid line represents the fitting used to extract the n_2 value

The 3D structures fabricated using the Cd(MA)₂ containing hybrid material follow the woodpile geometry and are depicted in figure 3.8. Woodpile photonic crystals with an interlayer periodicity of 600 nm, 550 nm and 500 nm were written and were next reacted with Na₂S to induce the formation of the CdS nanoparticles. Figure 3.8a shows an SEM image of an array of the 3D photonic structures. The top row corresponds to 600 nm period woodpile structures, the middle row corresponds to 550 nm period and the bottom row to 500 nm period structures. Moving from left to right, in the same image, the structures are fabricated with decreasing laser writing power at an energy step of ~ 0.04 TW/cm₂ (peak intensity at the focal point). Each woodpile structure has a footprint of 50 μm x 50 μm and consists of 10 unit cells while, the writing velocity was 20 $\mu\text{m}/\text{s}$ for all them.

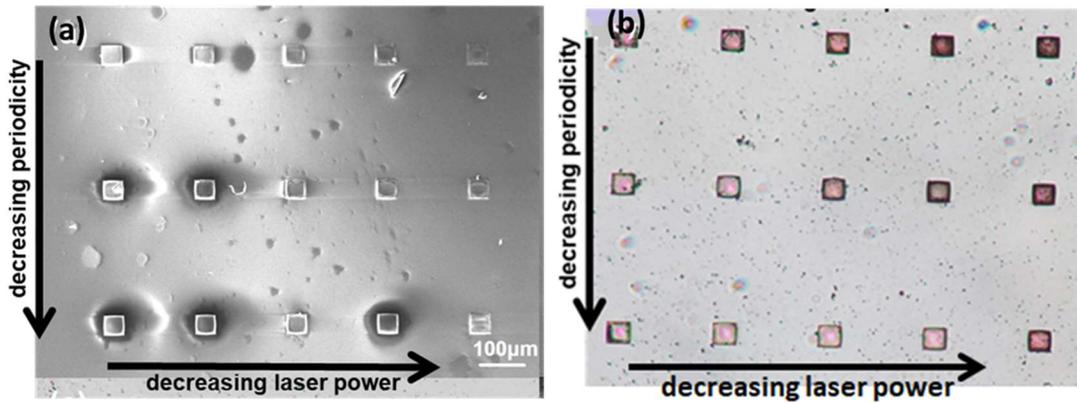


Figure 3.8. (a) SEM picture of the fabricated woodpile photonic structures functionalized with CdS quantum dots: overview of a series of woodpile structures with varying inlayer periodicity; 600 nm (top row), 550 nm (middle row), and 500 nm (bottom row) and with decreasing laser writing power (left to right), b) an optical microscope image of (a).

In addition, an optical microscope image of the same QD containing structures, depicted in figure 3.8a, is displayed in figure 3.8b. The woodpile photonic crystal is designed to have a band gap along the stacking direction [104] (i.e., normal to the substrate) and, hence, those structures with a prominent band gap display a vivid colour as the incident light is partially reflected by the structure due to the photonic band gap effect (e.g., all the structures depicted on and above the main diagonal of the picture). In contrast, those structures not exhibiting a photonic band gap display a dull colour as the incident light is fully transmitted (e.g., all the structures shown below the main diagonal of the picture).

A closer view of a 500 nm inlayer periodicity structure is depicted after functionalization with CdS QDs in figure 3.9. Figure 3.9a shows a top view of the structure while, figure 3.9b depicts the same structure at higher magnification. The woodpile structure demonstrate very high structural quality which verifies that the QD formation procedure is not destructive for the fabricated photonic devices.

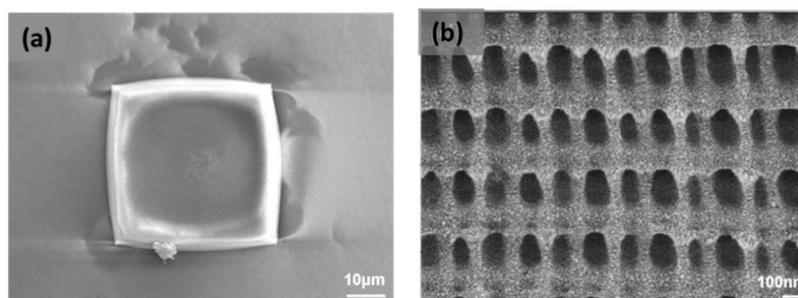


Figure 3.9. a) Top view of a 500 nm inlayer periodicity woodpile structure functionalized with QDs b) the same structure at higher magnification.

Energy Dispersive X-Ray Spectroscopy (EDS) measurements obtained from the functionalized woodpile structures revealed the cadmium and sulfur elements present in the structures supporting the formation of the QDs within the polymer photonic matrix. Figure 3.10 shows representative results of the EDS measurements taken on the structure depicted in figure 3.9, before and after the formation of the nanoparticles. Similar spectra were obtained for all the fabricated structures.

In order to validate the high quality of the fabricated 3D woodpile photonic crystals transmission and reflection spectra were obtained by FTIR spectroscopy to verify the presence of stop gaps. The results are shown in figure 3.11. In particular, transmission and reflection spectra were recorded before (Figure 3.11a) and after (Figure 3.11b) the QD formation within the 3D photonic matrix. The measurements were carried out at normal incidence (i.e., along the stacking direction of the woodpile structure) in the wavelength region from 1000 nm to 440 nm. As seen, the corresponding fundamental stop band for the case of a woodpile structure with inlayer periodicity 600 nm, 550 nm and 500 nm is clearly visible as a pronounced dip in the transmission and a peak in reflection; the peak wavelength of the band gap blue shifts from 760 nm, to 710 nm, and to 620 nm, by varying the inlayer periodicity from 600 nm, to 550 nm and to 500 nm, respectively.

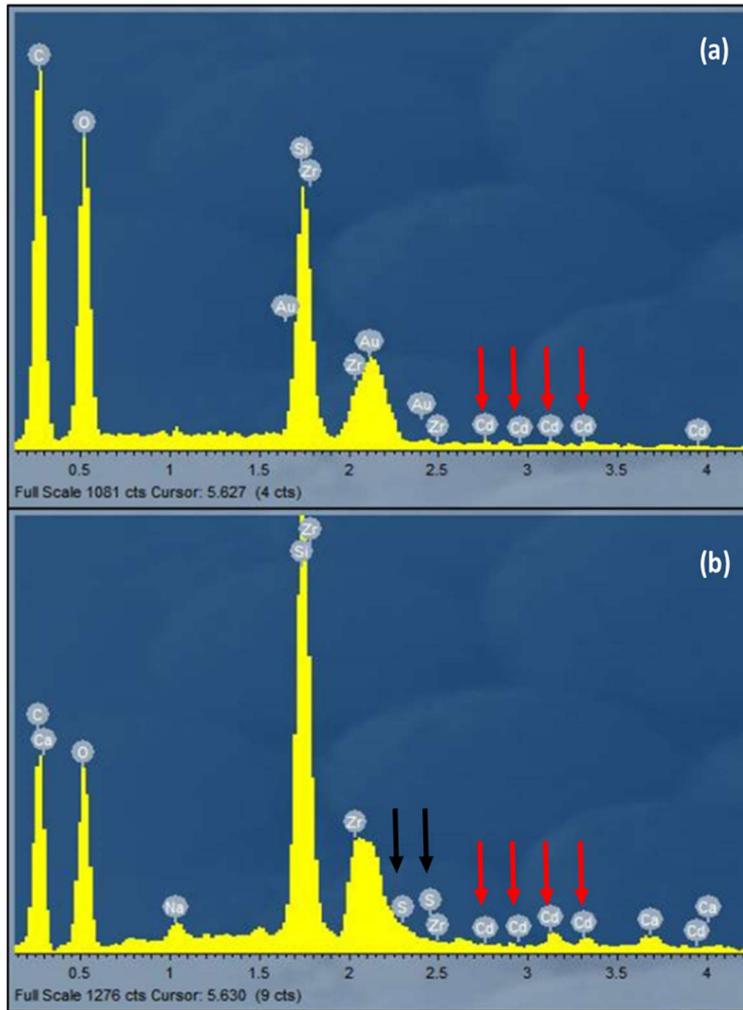


Figure 3.10. EDS measurements on a woodpile photonic crystal a) before and b) after the in situ synthesis of the CdS quantum dots. The red arrows show the Cd element while, the black arrows indicate the S element.

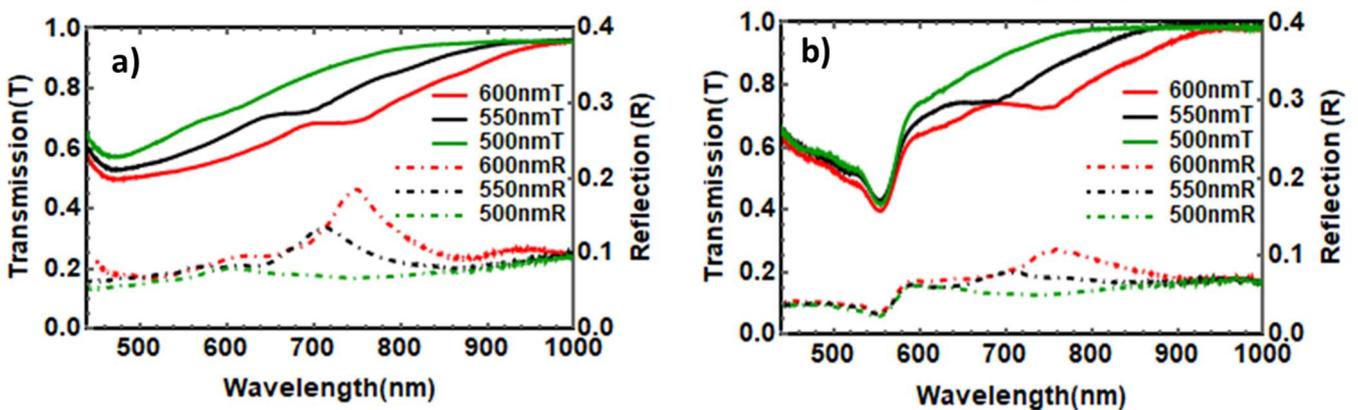


Figure 3.11. Measured transmission (solid) and reflection (dashed-dot) response of woodpile photonic structures with 600 nm (red), 550 nm (black) and 500 nm (green) inlayer periodicity (a) before and (b) after the in situ synthesis of the CdS quantum dots.

The results obtained from the FTIR measurements, showing the position and amplitude of the photonic stopgaps, were compared with theoretical calculations. The theoretical photonic band structure calculations were performed along the stacking direction (ΓZ) for the case of a woodpile structure with an inlayer periodicity $\alpha = 600$ nm, as shown in figure 3.12a, and predict that the central wavelength of the fundamental stop band should lie near 960 nm, which is about 200 nm red-shifted with respect to the experimentally observed value (i.e., stop band at 760 nm, figure 3.11). However, shrinkage of the 3D structures, due to the high loading of the composite material with organic molecules, such as DMAEMA, could have resulted in the deformation of the initial structure [115], and were verified by SEM (Figure 3.9a). Simulations on linear transmission spectra along the ΓZ direction, performed for the same system, are depicted in figure 3.12b (upper panel). It was calculated that when introducing a 20% shrinkage compared to the ideal structure (based on the SEM images) a blue-shift of the fundamental stop band of about 200 nm (Figure 3.12b, middle panel) is observed, which is in accordance with the experimental findings (i.e., stop band at 760 nm, shown in Figure 3.11, red-colored spectra).

Furthermore, sample imperfections are expected to have a direct influence on the optical properties of the structures, resulting in a less pronounced depth of the photonic band gap and an overall lower transmittance of about 50% with respect to the theoretically calculated value. A more pronounced effect is observed for the peak reflectance, which is highly influenced by the surface quality [150], [151]. In addition, the long-wavelength band gap edge in transmission appears steeper than the short-wavelength one, the latter showing an incomplete recovery of the transmittance (see figure 3.11). In order to take into account light scattering originating from surface roughness and sample imperfections, a phenomenological imaginary part of the index of refraction for the rod permittivity was introduced in the theoretical calculations as proposed in Ref. 151. The results are displayed in figure 3.12b (lower panel) showing a good agreement with the experimental findings.

The dynamic tuning of the photonic properties of the fabricated 3D woodpile photonic structures functionalized with CdS QDs was investigated using a time-resolved differential pump-probe technique [152]. With strong pumping, a femtosecond shifting of the photonic band gap is expected as a result of the changes induced in the refractive index of the backbone material in the photonic matrix due to the Kerr nonlinearity. Optimal homogeneous switching is expected especially near the first order band gap

and for pump wavelengths for which a Kerr nonlinearity can be induced. In order to maximize the switching magnitude, the pump wavelength should lie near the upper edge of the first order stop band [153]. Therefore, for all measurements presented herein, the sample was homogeneously excited by a pump beam centered at 795 nm, while it was probed by measuring the transmittance in the wavelength range from 440 nm to 720 nm as a function of the pump-probe delay time. Differential pump-probe measurements were achieved by splitting the probe beam into two parts, used as the signal and the reference, respectively.

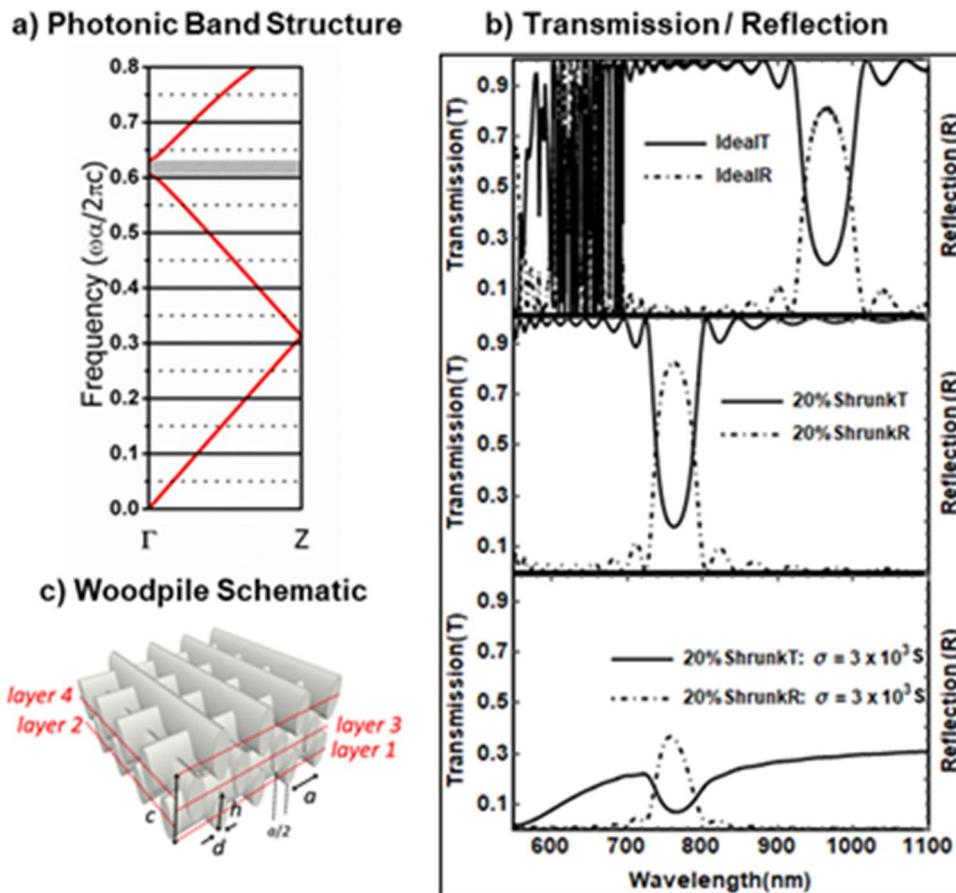


Figure 3.12. Theoretical calculations along the stacking direction (ΓZ) of a woodpile photonic crystal with inlayer periodicity $\alpha = 600$ nm: a) photonic band structure calculations of an infinite system, b) simulated transmission (solid) and reflection (dashed-dot) response for finite system with 10 unit cells ($4 \times 10 = 40$ layers), assumed to be infinite in the inlayer plane; i) ideal structure (upper panel), ii) introducing 20% shrinkage to the ideal structure (middle panel), iii) introducing artificial loss (conductivity, σ) into the dielectric rods equal to $\sigma = 3 \times 10^3$ S (lower panel) and c) schematic of the woodpile photonic crystal showing one unit cell (of length c) along the stacking direction.

Prior to recording the dynamic tuning of the photonic band gap properties, a complementary tracking of the CdS exciton dynamics was provided by a transient absorption experiment carried out for the case of a QD containing polymer film. The time-resolved differential pump-probe measurements obtained are shown in the main panel of figure 3.13, where a time-resolved spectral representation of the changes in the Optical Density (ΔOD) (z-axis, color-axis) as a function of wavelength (y-axis) and the pump-probe delay time (x-axis) is displayed (see Experimental Section for details). Regions appearing red show a positive change in the OD , while those appearing blue represent negative change in the OD as shown in the colour-scale on the left-hand side. The zero pump-probe delay is also recorded as a cross-correlation parabolic-like trace between the scattered pump light from the sample and a delayed white light pulse. Note that the time-zero of the experiment is not unique and varies with the probe wavelength. This is due to the chromatic dispersion that the broadband white light supercontinuum probe beam has attained since its generation

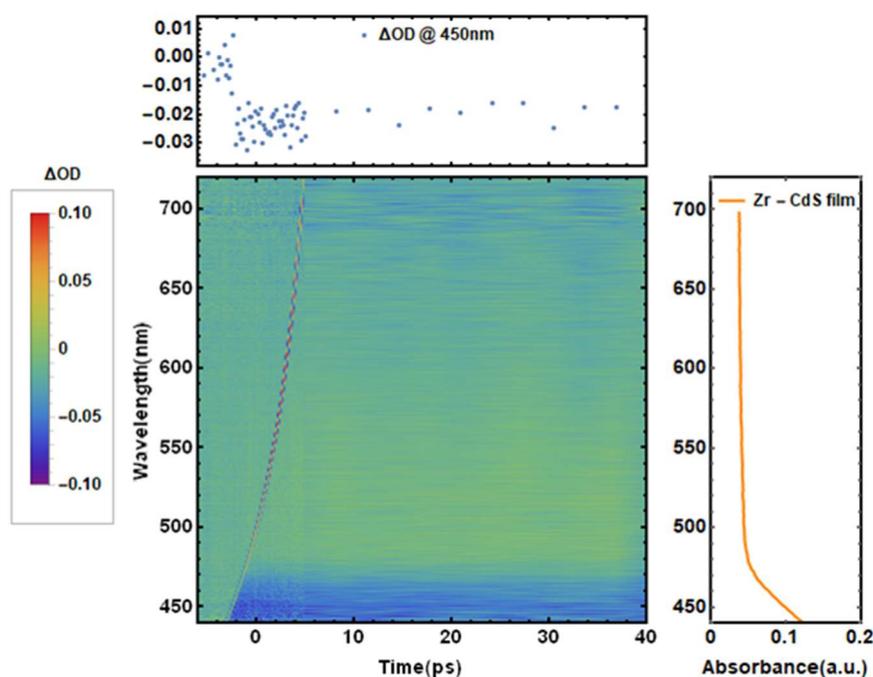


Figure 3.13. Pump-probe measurements on a polymer film doped with CdS quantum dots. Incident pump fluence ~ 17.5 mJ/cm². Main panel: Spectrogram of the changes in Optical Density (ΔOD) of transient absorption as a function of wavelength and pump-probe delay time. Left panel: Color-scale representing the range of ΔOD values. Upper panel: A temporal cross-section of $\Delta OD(\Delta t)$ at the wavelength of 450 nm. Right panel: UV-Vis absorption spectrum (also shown in Figure 3.5) of the QD containing polymer film.

A spectral region where $\Delta OD < 0$ was recorded at wavelengths shorter than 475 nm, just after the arrival of the excitation pulse, (incident pump fluence at $\sim 17.5 \text{ mJ/cm}^2$) hinting at a femtosecond rise-time, which correlates to the exciton binding energy of CdS. Given that the pump operates at 795 nm, this is clear evidence of a nonlinear process, which is in fact two-photon absorption and is in accordance with the linear absorption spectrum obtained from UV-Vis spectroscopy (right panel, also shown in Figure 3.5).

It should be noted that the ΔOD is defined as $\Delta OD = \log \frac{I^{ref}}{I^{sig}}$, where I^{Sig} is the power transmitted from the sample (Signal) and I^{Ref} is the power transmitted from the Reference. In the absence of pump, $\frac{I^{ref}}{I^{sig}}$ is equal to 1. Hence, ΔOD tracks changes in the transmittance from the sample due to the presence of the pump; in the absence of the pump or when no changes are induced by the presence of the pump would yield $\Delta OD = 0$ marked as the green areas on the plot, while increased transmission corresponds to $\Delta OD < 0$, marked as blue regions, and reduced transmission as $\Delta OD > 0$, shown as red regions. In the case of the QD containing film, before the pump is applied, the probe beam is subject to absorption according to the spectra shown in Figure 3.5. Once the pump is present, the population is excited as the pump is absorbed by the film and, therefore, when the probe arrives thereafter, less population is available in the ground state to absorb the probe power leading to a reduced absorption and, hence, an increased transmittance from the film (compared to the absence of the pump). This is manifested as $\Delta OD < 0$ i.e., the blue region shown in Figure 3.13. Of course, after excitation, the population starts relaxing and as the pump-probe delay is increased, this is experienced by the probe as an increased absorption (higher population is available in the ground state to absorb the probe power). Eventually, for very long delays the population returns to its ground state and is all available again to be absorbed entirely by the probe (not shown for the time window chosen here).

In addition, a temporal cross-section of $\Delta OD(\Delta t)$ at the wavelength of 450 nm is depicted in Figure 3.13, upper panel, where the observed dynamics reflect the energy relaxation and recombination of the photo-excited carriers. The results obtained are typical for II-VI QDs embedded in a glass/polymer matrix usually consisting of fast initial decay components with characteristic time constants from tens of femtoseconds to several picoseconds followed by a slower nanosecond decay [154]–[156].

Furthermore, in order to eliminate any effect arising from the pure polymer film, a similar experiment was carried out for the composite sample before the formation of the QDs, shown in figure 3.14, where no pump-induced change was recorded in the OD as expected.

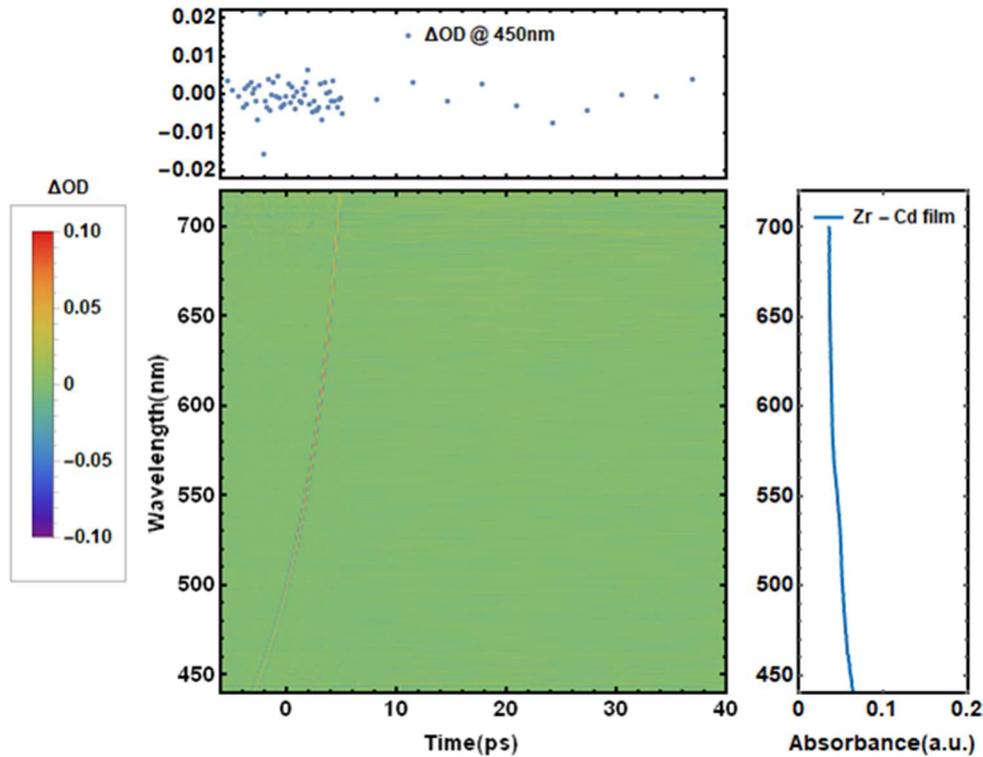


Figure 3.14. Pump-probe measurements of a sample of the composite material before the formation of the QDs. Incident pump fluence $\sim 17.5 \text{ mJ/cm}^2$. Main panel: Spectrogram of the changes in Optical Density (ΔOD) of transient absorption as a function of wavelength and pump-probe delay time. Left panel: Color-scale representing the range of ΔOD values. Upper panel: A temporal cross-section of $\Delta OD(\Delta t)$ at the wavelength of 450 nm. Right panel: UV-Vis absorption spectrum (also shown in Figure 3.5) of the pure polymer film.

Time-resolved differential pump-probe measurements were carried out for the case of a woodpile structure functionalized with CdS QDs, shown in Figure 3.15. On the right panel, the linear transmission spectrum of the respective woodpile photonic structure with 600 nm inlayer periodicity is displayed (also shown in Figure 3.11b) in order to facilitate the comparison of the dynamics. The location of the fundamental stop-band is marked as a grey region. On the left panel, the color-scale representing the range of the recorded ΔOD values is depicted. At high excitation levels ($\sim 11 \text{ mJ/cm}^2$), an intense pump-induced change in the differential signal dynamics is recorded on the right-hand

side of the zero delay line (marked as a red dotted line) for a wide wavelength range below the short-wavelength band gap edge for a long time period of several ps (> 25 ps). In particular, positive values of the OD are recorded upon excitation that build up for positive time delays indicating that $\frac{I^{Ref}}{I^{Sig}} > 1$ i.e., the transmittance from the woodpile structure decreases.

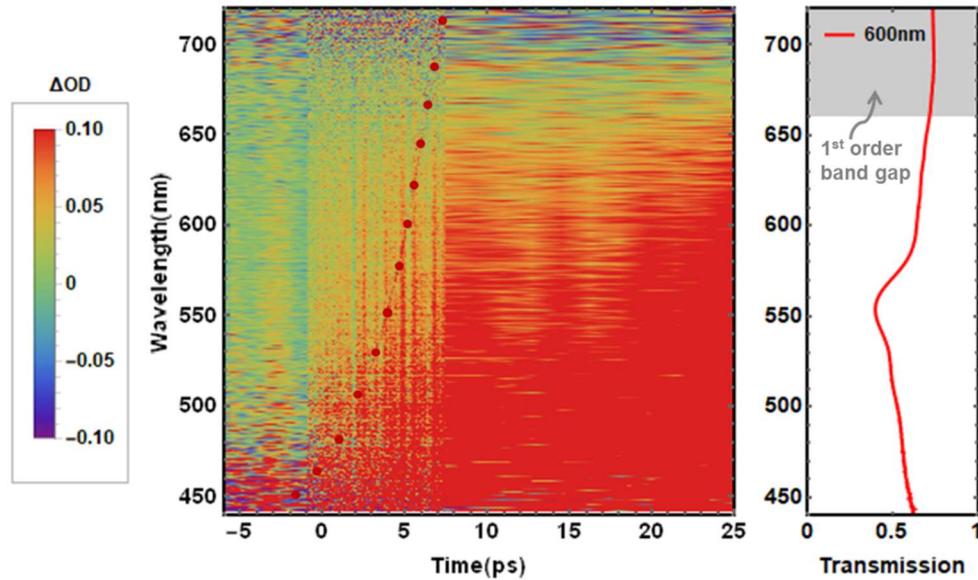


Figure 3.15. Pump-probe measurements on a woodpile structure with 600 nm inlayer periodicity containing CdS quantum dots. Incident pump fluence ~ 11 mJ/cm². Middle panel: Spectrogram of the changes in Optical Density (ΔOD) of transient absorption as a function of wavelength and pump-probe delay time. The red dots are a guide to the eye indicating the cross-correlation trace of pump-probe delay. Left panel: Color-scale representing the range of ΔOD values. Right panel: Transmission spectrum (also shown in Figure 3.11b) of the functionalized woodpile structure. The gray region represents the position of the fundamental band gap.

However, this is an unexpected result which implies that either the changes in transmission are observed possibly due to a pump-induced shift of the photonic band gap, or that the woodpile photonic crystal is damaged due to the high pump excitation and, hence, lower intensity is recorded due to scattering. FTIR linear transmission measurements, shown in figure 3.16, were performed on the same woodpile structure after the excitation and revealed that the woodpile structure remained intact.

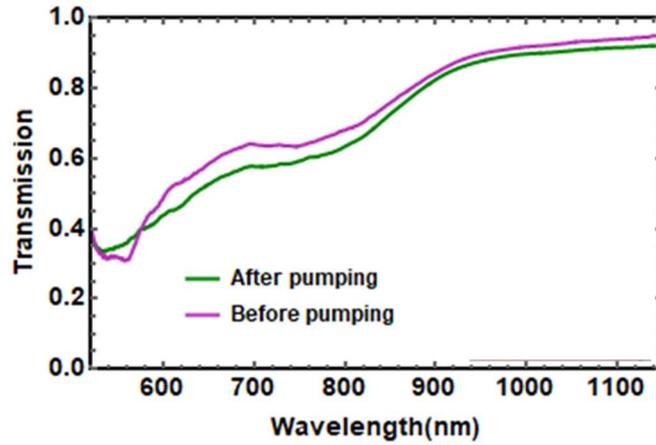


Figure 3.16. Transmission measurements for a woodpile structure with 600 nm inlayer periodicity functionalized with CdS quantum dots: before (purple) and after (green) high pump excitation (incident pump fluence $\sim 11 \text{ mJ/cm}^2$).

Moreover, time-resolved differential pump-probe measurements at high excitation energies ($\sim 18.1 \text{ mJ/cm}^2$) were carried out on woodpile photonic crystal structures before the formation of the CdS QDs in order to confirm that the pump-induced changes recorded for the doped sample were not due to the polymer matrix. The results obtained for the hybrid woodpile structure with 600 nm inlayer periodicity are shown in Figure 3.17, where no pump-induced change of the OD was recorded.

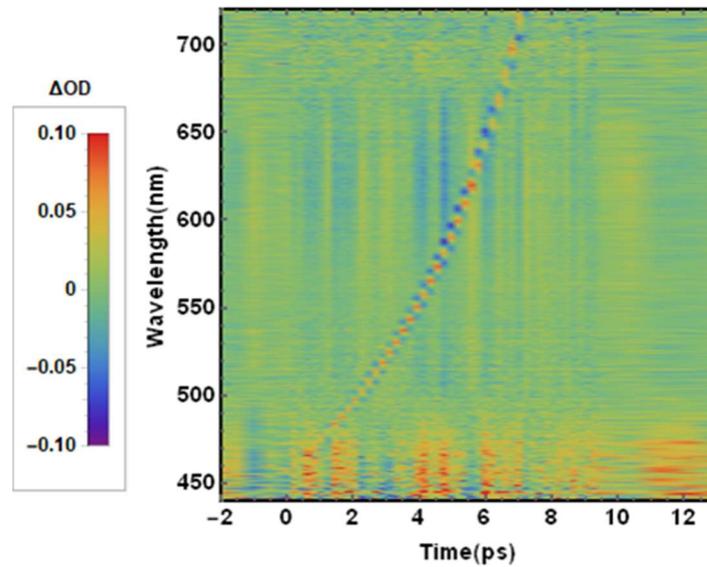


Figure 3.17. Pump-probe measurements on a woodpile structure with 600 nm inlayer periodicity prior to the in situ synthesis of the CdS quantum dots. Incident pump fluence $\sim 18.1 \text{ mJ/cm}^2$. Main panel: Spectrogram of the changes in Optical Density (ΔOD) of transient absorption as a function of wavelength and pump-probe delay time. Left panel: Color-scale representing the range of ΔOD values.

According to photonic-band-structure calculations for materials possessing Kerr nonlinearity, a positive change in refractive index would lead to a “blue” shift of both photonic band edges along with a significant widening of the photonic band gap [157]–[159]. In our case, a pump-induced response of the QD containing woodpile structures was observed on a sub-picosecond time scale mainly recorded for a wide wavelength range below the short-wavelength band gap edge. In addition, the recorded signal rises further at positive time delays (> 10 ps), instead of rapidly decaying as the photonic feature would relax back to its original wavelength, also reported previously in analogous experiments involving 3D nonlinear photonic crystals [160]–[162]. However, in most cases, semiconductor materials such as gallium arsenide or silicon were utilized, where large-refractive index-contrast photonic crystals were obtained and a monochromatic probe beam was employed, instead of a white light super-continuum probe, with a central wavelength located at the short-wavelength band gap edge in order to achieve high intensity contrast between the “on” and “off” states of the optical switching.

In our case, a clear ultrafast dynamic response is recorded for the woodpile photonic structures functionalized with CdS QDs, which indicates a photonic band gap shift, however, further experiments are required to identify the competing ultrafast all-optical switching mechanisms that take place between the 3D polymer photonic matrix and the functionalized QDs [121] for a comprehensive understanding of the underlying effects in order to reach more solid conclusions. Such a complementary study of the involved mechanisms is planned as part of our future work. In this context, more stable QDs systems need to be developed with narrow size distribution, as well as, enhanced resistance to photo-bleaching for potential applications in the field of ultrafast all-optical switching.

3.4 Conclusions

High-resolution 3D woodpile photonic devices were successfully fabricated containing an organic-inorganic silicon-zirconium composite and CdS QDs. The structures were realized by the combination of diffusion-assisted DLW by two-photon absorption and the in situ synthesis of CdS NPs. The novel active 3D printable hybrid composite

material exhibits a high nonlinear refractive index value measured by means of the z-scan method, whereas the fabricated woodpile structures show clear photonic stop bands in the visible wavelength region. By means of time-resolved pump-probe spectroscopy, evidence of a photonic band gap shift was demonstrated. It is expected, that the nanocomposite material presented herein, can find applications in active micro/nanodevices, such as ultrafast switching and modulation applications.

CHAPTER 4: 3D photonic structures for photonic crystal lasing applications

The fabrication of 3D photonic devices functionalized with a gain material which emits in the visible region of the electromagnetic spectrum is reported. The 3D structure under consideration is a photonic crystal following the woodpile geometry with inlayer periodicity of 550 nm, while the gain medium consists of CdSe-CdS core-shell QDs. For the fabrication of the 3D photonic structures the Direct Laser Writing (DLW) technique was employed. The QDs were synthesized using high temperature wet chemical methods and their incorporation in the PC structures was performed by chemical functionalization of the surface of the 3D structures in order to achieve permanent attachment of the QDs.

4.1 Introduction

Lasing action can be achieved by the combination of three ingredients: a gain medium, a pump source and a feedback mechanism. The most widely known example are the common lasers. They use a set of mirrors that create a cavity (feedback mechanism), with a gain material (gain medium) placed between them, while the pumping can be either electrical or optical. It has been proposed that the size of the lasers can be reduced, to occupy only a few cubic micrometers, using photonic crystal structures. As discussed above PCs exhibit photonic bandgaps. Near the band edge of these gaps, the group velocity, v_g , of photons localized in the structure approaches zero, and this can be treated as a slow light effect. In this way, photons undergoing multiple reflections in the lattice experience longer interaction with the gain material, thus resulting in an enhanced effective gain. In PCs fabricated with gain materials, lasing operation occurs at the band edges.

Over the last years, tremendous research has focused on the fabrication of photonic crystal devices due to their potential application to control, bend, trap, switch, slow, reflect and extract light. A large part of this research was dedicated to the fabrication of photonic crystal lasers. To date, most of the studies involved 2D devices [163]–[172] and has utilized planar 2D photonic crystal slab cavities.

The realization of 3D photonic crystal lasers has been hindered by limitations in 3D fabrication. The difficulty doesn't arise from the fabrication of the structures themselves, but rather from the combination of the 3D photonic crystals with an appropriate gain material that will result in an effective gain device. Most of the work reported in the literature on 3D PC involves the use of liquid crystal-based materials [173] and the self-assembly of colloidal particles which create opal [174]–[176] or inverse opal [177], [178] structures, and this is because this is the most facile method of creating 3D PC structures. These systems have though certain demerits. In most of the cases, and in real lasing experiments, they need to be immersed in dye based liquids which reduce the refractive index contrast and pose serious complications for practical applications. Moreover, inverse opal structures are very susceptible in fabrication defects apart from yielding very small sample sizes. The greatest disadvantage though, in all cases, is the use of organic dyes as a gain medium. These molecules suffer from poor thermal and photo-stability, which hamper microscopic applications, requiring high excitation light intensities (pumping in the case of lasers) and resulting in short-term lifetime of the devices. Moreover, their narrow band absorption limits the pumping sources used for their excitation, rising once again the issue of practical applications. In the seek for potential alternatives, photonic crystals containing quantum dots have gained enormous interest from the research community in recent years [179]. Quantum dots are semiconductor nanoparticles and are considered the best alternative to organic dyes due to their attractive property of comprising an absorption that gradually increases toward shorter wavelengths (below the first excitonic absorption band) and a narrow emission band of mostly symmetric shape. The spectral position of absorption and emission are tunable by the particle size (the so-called quantum size effect). This broad absorption allows free selection of the excitation wavelength. Moreover, quantum dots are stable fluorophores, due to their inorganic nature, which reduces the effect of photobleaching compared to organic dyes. The work that stands out so far, is the one reported by Tandaechanurat *et al.* [180]. These researchers demonstrated lasing action in a 3D photonic crystal nanocavity containing quantum dots at an emission wavelength of 1200 nm. Although their 3D photonic crystal possesses a full bandgap, it suffers from serious drawbacks. They observed the lasing oscillation at liquid helium temperature (7 K), which automatically makes its integration in 3D photonic circuits very difficult.

Herein, we report the fabrication of 3D photonic structures that could act as nanolasers, from woodpile photonic crystal structures fabricated using multi-photon lithography and novel hybrid organic –inorganic materials.

4.2 Experimental

4.2.1 Material synthesis

4.2.1.1 Hybrid photopolymerizable material synthesis

The hybrid material was prepared using methacryloxypropyltrimethoxysilane (MAPTMS, Sigma-Aldrich), 2-(dimethylamino)ethyl methacrylate (DMAEMA, Sigma-Aldrich), methacrylic acid (MAA, Sigma-Aldrich) and zirconium propoxide $Zr(OPr)_4$, (ZPO, 70% solution in 1-propanol, Sigma-Aldrich). All chemicals were used without further purification.

The precursors used are metal alkoxide molecules and organic and hybrid monomers. For the formation of the inorganic network, zirconium propoxide was used. Methacryloxypropyltrimethoxysilane (MAPTMS), 2-(dimethylamino)ethyl methacrylate (DMAEMA) and methacrylic acid (MAA) served as the hybrid and organic monomers. MAPTMS monomer carries a trialkoxysilane functional group, which undergoes hydrolysis and condensation and is thus attached to the inorganic network. Moreover, bearing a polymerizable methacrylate moiety, it contributes to the formation of the organic matrix. 4,4' – Bis(diethylamino) benzophenone (BIS) was used as the photoinitiator. Figure 4.1 shows the chemical structures of the chemicals used for the synthesis of the material.

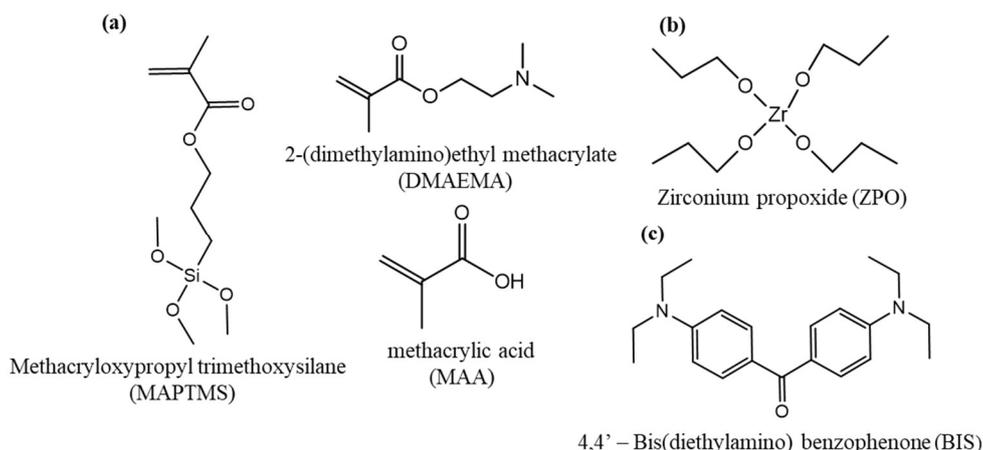


Figure 4.1. Chemical structures of the chemicals used for the synthesis of the hybrid photosensitive material

For the synthesis of the hybrid material the sol-gel technique was employed. First, MAPTMS at a 8:2 molar ratio with respect to ZPO, was hydrolyzed by the addition of HCl (concentration 0.1 M) and the mixture was stirred for 15 minutes. In a separate flask, ZPO was chelated by adding MAA at a 1:1 molar ratio with respect to ZPO. The solution was stirred for 20 minutes. The hydrolyzed MAPTMS was then added dropwise to the ZPO-MAA solution, followed by another 20 minutes of stirring. DMAEMA was then added, at a 30% molar ratio with respect to MAPTMS and MAA. The mixture was stirred for 5 minutes, following the addition of a small amount of nanopure water. Finally, BIS (Sigma-Aldrich), 1% w/w with respect to the monomers, was used as the photoinitiator. After stirring for 30 minutes, the material was filtered using a 0.45 μm pore size filter. The reactions taking place during the synthesis of the material are shown in section 3.2, Figure 3.3.

4.2.1.2 CdSe-CdS core-shell quantum dot synthesis

The materials used for the synthesis of the core-shell quantum dots are cadmium oxide (99.99%), selenium (99.5%, 100 mesh), sulfur (99.98%, powder), trioctylphosphine oxide (TOPO, 90%), tributylphosphine (TBP, 97%), 1-octadecene (ODE), oleic acid (OA, 90%), hexadecylamine (HDA, 97%) and stearic acid (99%). All chemicals were purchased from Aldrich and were used without any further purification.

Octadecene (ODE) was selected as the only noncoordinating good solvent for both the core nanocrystals and the two injected solutions for the growth of the shells. Its relatively low melting point (below 20 °C), high boiling point (about 320 °C), low cost, low toxicity, low reactivity, and excellent solvation of all other compounds at elevated temperatures, render ODE an ideal solvent for the growth of high-quality nanocrystals [48], [181]. CdO and elemental sulfur were chosen as the precursors for the growth of the CdS shell onto the CdSe core nanocrystals. Hexadecylamine (HDA) was used as the ligand for the core-shell nanocrystals, because alkylamines have been proven to be good ligands for the highly luminescent plain CdSe core [42], [49] and the CdSe-CdS core-shell nanocrystals [182].

The synthesis of the CdSe-CdS nanocrystals was carried out using a slight modification of the procedure reported in Ref. [66].

CdSe core synthesis. In a typical reaction, 0.2 mmol CdO, 0.8 mmol stearic acid, and 2 g ODE were added in a 25 ml two-neck flask, placed in a heating mantle, and were heated to about 200 °C to obtain a colorless clear solution. Next, this solution was cooled to room temperature and HDA (1.5 g) and 0.5 g of TOPO were added in the flask. The system was degassed under a nitrogen flow and was reheated to 280 °C. A selenium solution was prepared at this temperature by dissolving 2 mmol of Se in 0.472 g TBP, and following dilution with 1.37 g ODE was quickly injected in the reaction vessel. The temperature was then reduced to 250 °C for the growth of the cores. Nanocrystal size was monitored by recording the UV-vis spectra of aliquots taken from the reaction solution at different time intervals. The reaction was stopped by removing the heating after the desired size was achieved. The core nanocrystals were purified by precipitation/decantation with excess of 2-propanol in a centrifuge at 11000 rpm and 5 °C for 30 min. Finally, the collected cores were redispersed in hexane.

CdS shell growth. For the deposition of the shell on the cores, the successive ionic layer adsorption and reaction (SILAR) method was used. The SILAR technique is based on the alternating injections of the Cd and S precursors in the solution containing the CdSe nanocrystals for the growth of CdSe-CdS core-shell particles. The amount of cadmium or sulfur precursors required for each layer was determined by the number of surface atoms on a given size core-shell nanocrystal. Because there is only about 5-6% lattice mismatch between the CdSe and CdS bulk crystals, the calculations were based on the wurtzite structure of CdSe nanocrystals for the first layer, while for the remaining layers the calculations were based on the wurtzite structure of CdS, always taking in

account the increase in the diameter of the particles after each shell formation. The average thickness of one monolayer of CdS was taken as 0.35 nm, so every additional layer would increase the diameter of a nanocrystal by 0.7 nm [66].

The injected cadmium solution (0.04 M) was prepared by dissolving CdO (0,0615 g) in oleic acid (1,083 g) and ODE (10,8 mL) at 250 °C. The injected sulfur solution (0.04 M) was prepared by dissolving 0,0128 g sulfur in 10 ml ODE at 200 °C. Both injected solutions were made prepared under a N₂ flow. After obtaining clear solutions, the injected Cd solution was allowed to cool to about 60 °C and the sulfur solution was allowed to cool to room temperature. For each injection, a calculated amount of a given solution was obtained by a syringe.

The amount of Cd and Se precursor solution required to form each CdS layer, was calculated as following. First, the size of the CdSe cores was measured by TEM. Next, the absorption spectrum of a solution of the CdSe cores was employed to calculate their number using the Beer-Lambert law, $A = \varepsilon c \ell$, where A is the absorption maximum, ε is the extinction coefficient of the nanocrystals and is size dependent, c is the concentration of the solution and ℓ corresponds to the path the light has traveled through the nanocrystal solution (i.e the cuvette thickness). The extinction coefficient was calculated according to Ref. [183]. For the formation of the first CdS layer, the surface anion/cation pairs (i.e Cd/Se pairs) of the plain CdSe nanocrystals were calculated for a single core using the following equation:

$$\text{surface anion/cation pairs} = \frac{4\pi r^2}{d^2}$$

Where, r corresponds to the radius of the core and d is the lattice parameter of the wurtzite structure of the CdSe nanocrystals. Next this value was multiplied by the number of cores in the solution to find the total surface anion/cation pairs. Finally, the same amount of Cd and S atoms was used for the formation of the first layer.

For the remaining layers, a similar procedure was followed, using for each extra layer the correct r (increased by 0,25 nm for each CdS layer) and d values, which coincide with the wurtzite CdS lattice parameter value for the second layer and above.

For the formation of the CdS shell, the CdSe nanocrystals were dissolved in hexane and mixed with 1.5 g ODA and 5.0 g ODE, in a 25 mL two-neck flask. The flask was then pumped down at room temperature with a mechanical pump for 30 min to remove the hexane and at 100 °C for another 5-10 min to remove any residual air from the system. Subsequently, the system was purged with N₂ and the reaction mixture was further

heated to 240 °C. Every 5 min alternating injections of the Cd and S precursor solutions were injected in the flask, until the desired number of shells were formed. The purification of the core-shell particles was performed by centrifugation using an excess of 2-propanol at 11000 rpm and 5 °C. Finally, the particles were redispersed in anhydrous toluene.

4.2.2 Sample preparation

Before the formation of the samples on glass substrates the latter were silanised following a two-step procedure described below. First, a mixture of ammonium hydroxide (NH₄OH) solution (28% w/w) was mixed with hydrogen peroxide (H₂O₂) solution (35% w/w) at a 3:1 volume ratio. Then, the glass substrates were immersed in the NH₄OH/H₂O₂ solution with both sides facing the liquid mixture. Subsequently, the solution was heated to 75 °C for 30 mins. This process leads to the effective cleaning of the surface of the substrates from any organic residue (dirt) and to the increase of the surface density of the silanol groups on the glass substrate. Finally, the substrates were rinsed thoroughly with deionized water and were dried under a nitrogen flow. In the second step, the clean substrates were immersed in a mixture of toluene and MAPTMS at a 0.2 % v/v, with both sides exposed to the mixture. The substrates were left in the MAPTMS solution overnight to ensure the formation of a dense layer of MAPTMS on the surface obtained by the reaction of the surface silanol groups with the methoxysilane groups of MAPTMS

The samples were prepared by drop casting the hybrid material onto 100 µm-thick round silanized glass substrates for the 3D microfabrication. The resultant drops were dried under vacuum at ambient temperature for three days before the photopolymerization. The drying process led to the condensation of the alkoxide groups and the formation of the inorganic network and to any volume loss of the material due to evaporation of solvent traces produced by the condensation process. Next, the samples were exposed to laser (800 nm) irradiation for the fabrication of the 3D structures. After the irradiation process, the non-polymerized material, was removed by developing the samples sequentially in 4-methyl-2-pentanone, 2-propanol and dimethyl sulfoxide (DMSO). Following the development process, the 3D structures were functionalized with the CdSe-CdS core-shell particles.

The functionalization of the 3D structures with the CdSe-CdS QDs was achieved by the chemical attachment of the particles onto the surface of the photonic structures.

Three different routes were followed for this purpose:

1. Functionalization of the surface of the 3D structures with (3-aminopropyl)triethoxysilane (APTES) or (3-aminopropyl)- dimethylethoxysilane (APDES). The chemical structures of these molecules are shown in Figure 4.2. The hydroxyl groups present on the surface of the hybrid material, used for the fabrication of the 3D structures, were exploited for the binding of APTES or APDES molecules onto the surface of the 3D structures. The fabricated photonic structures were immersed in a 0,5 % v/v solution of APDES or APTES in anhydrous toluene. The structures were kept immersed in the solution overnight and were next, removed and rinsed several times with anhydrous toluene. In a second step, the functionalized structures were immersed once again in a solution of the CdSe-CdS QDs in anhydrous toluene and were kept overnight at 70-80 °C. At this step, capping exchange reactions took place on the surface of the QDs, and some of the hexadecylamine molecules were replaced with the APTES or APDES molecules attached on the 3D structures. Finally, the QD functionalized structures were rinsed several times with toluene.

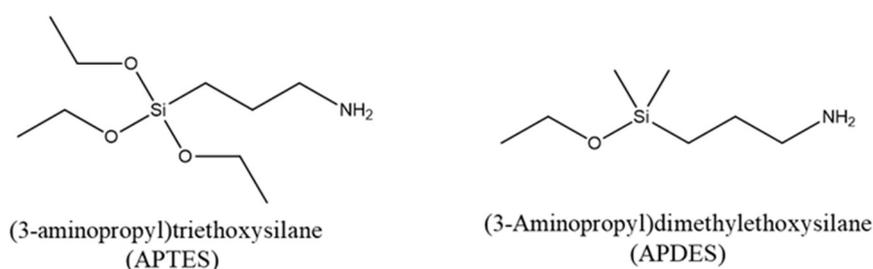


Figure 4.2. Chemical structures of APTES and APDES used for the permanent attachment of the CdSe-CdS quantum dots on the surface of the 3D structures

2. The second route involved the capping exchange of the quantum dots with APTES or APDES and in a second step the reaction of the QDs, functionalized with these molecules, with the 3D structures to covalently attach the particles on the surface of the 3D structures. Capping exchange of 30 %, 50 %, 70 % and 100 % of the ligands stabilizing the particles was investigated, by dissolving the appropriate amount of APTES/APDES for each capping exchange reaction in a solution of the QDs in anhydrous toluene and letting the reaction to proceed overnight at 70-80

°C. Using the APTES molecule, a capping exchange up to 30% was successfully achieved. Above this APTES ratio, the QD particles formed aggregates and were precipitated at the bottom of the reaction flask, possibly due to the hydrolysis of the trifunctional alkoxy silane site of the APTES molecule from residues of moisture inside the flask, in combination with the high amount of APTES ligands on the surface of the QDs, that led to the interconnection of the particles. For the APDES molecule a capping exchange up to 100% was achieved, without the formation of aggregates. Next, the 3D structures were immersed in the QD solution overnight for the immobilization of the particles on the surface of the structures.

3. The third route involved the combination of the above two approaches in one pot. For this, the 3D structures were immersed in a solution of the CdSe-CdS particles in anhydrous toluene and the appropriate amount of APDES molecule was added. The reaction flask was kept at 70-80 °C overnight, in which the capping exchange of the particles and their attachment on the 3D structures took place simultaneously.

All routes were successful and gave similar results, however, the QD functionalized 3D structures obtained by the second and third routes, exhibited slightly enhanced photoluminescence compared to those obtained by the first route.

4.2.3 Fabrication of the 3D photonic structures

3D photonic devices of woodpile geometry was fabricated by DLW (see section 1.4.4). For the fabrication of the 3D structures the procedure described in Sections 2.2.5 and 3.2.5 was used. Briefly, the laser source employed was a Ti:Sapphire femtosecond oscillator operating at 800 nm with a pulse length of < 20 fs and a repetition rate of 75 MHz. A 100x microscope objective lens (Zeiss, Plan Apochromat, N.A. = 1.4) was used to focus the laser beam into the volume of the photosensitive material. The writing speed employed was $20 \mu\text{m s}^{-1}$ and the peak intensity at the center of the focal point was $\sim 0.35 \text{ TW/cm}^2$. After completion of the component building process, the samples were developed for 30 min in ethanol, 30 min in 4-methyl-2-pentanone and 30 min in DMSO, and were further rinsed with 2-propanol.

4.2.4 Characterization of the CdSe-CdS Quantum Dots and the 3D structures

The synthesized quantum dots were characterized by UV-Visible spectroscopy, Photoluminescence (PL) spectroscopy and Transmission Electron Microscopy (TEM), while their emission efficiency was determined by means of their relevant quantum yield (QY) with respect to a known highly fluorescent dye. The fabricated 3D photonic devices functionalized with the CdSe-CdS nanoparticles were characterized by Scanning Electron Microscopy (SEM), Fourier Transform Infrared (FTIR) transmittance/reflectance spectroscopy and micro-photoluminescence (μ -PL) spectroscopy.

UV-Visible spectroscopy: the absorption spectra of thin films of the material were recorded in the 250-800 nm spectral range using a Perking Elmer UV-Vis spectrometer.

Photoluminescence spectroscopy and QY measurements: For the PL measurements, dilute solutions of the CdSe and CdSe-CdS quantum dots in toluene were prepared. The CdSe-CdS solutions had a maximum absorption in the range of 0.05 to 0.1. Sulfo-Rhodamine 101 was used as the fluorescent standard. Measurements were recorded on a Jobin–Yvon Horiba, FluoroMax-P (SPEX) fluorescence spectrometer upon excitation with a Xenon arc lamp (emission range 290-700 nm).

TEM: Transmission electron microscopy images were obtained with a JEOL JEM-2100 electron microscope operating at an accelerated voltage of 200 kV. Samples for TEM were prepared by depositing a drop of the dilute CdSe-CdS nanoparticle solution onto a carbon-coated Cu grid.

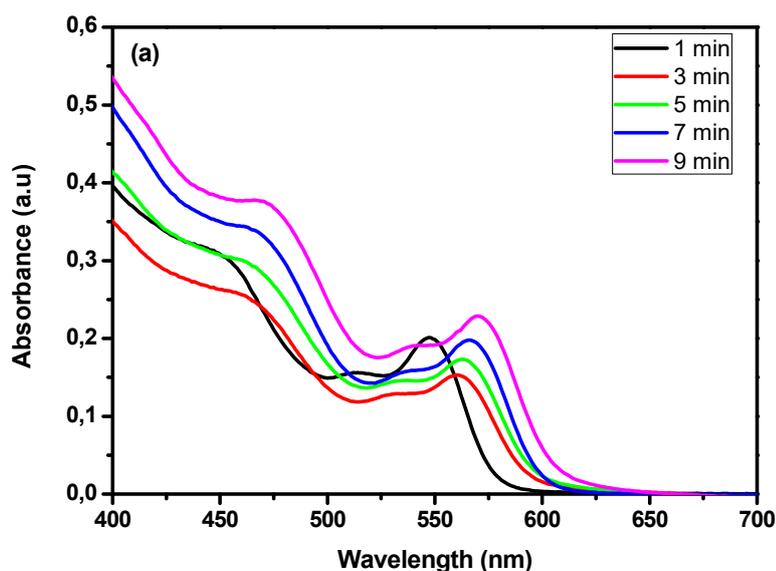
SEM: Scanning Electron Microscopy images were obtained with a JEOL Model JSM-6390LV scanning electron microscope equipped with an Oxford INCA PentaFET-x3 energy dispersive X-ray spectroscopy (EDS) detector.

FTIR spectroscopy: FTIR transmittance/reflectance spectra were measured with a Vertex 80 spectrometer coupled to a Hyperion 2000 IR microscope (Bruker Optics) and equipped with Cassegrain objectives (15 \times , 36 \times) and a liquid nitrogen cooled mercury cadmium telluride detector.

Micro-Photoluminescence measurements: μ -PL spectra were collected on a backscattering setup, using a continuous wave laser at 473 nm as an excitation source and a 40x objective with a numerical aperture of 0.65 forming a 1 μ m spot diameter. The excitation power for all measurements was set to 6 μ W [184].

4.3 Results and discussion

The growth of the CdSe nanoparticles during their synthesis reaction was monitored by removing small aliquots from the reaction flask at different time intervals, and analyzing the samples by UV-Vis and PL spectroscopy. Samples were removed using a glass syringe, at 1 min, 3 min, 5 min, 7 min and 9 min reaction time, and were quickly added in cold hexane to terminate the reaction. After purification the spectra were recorded and are shown in Figure 4.3. A shift towards higher wavelengths (red-shift) was observed in the absorption and PL spectra with increasing the reaction time, suggesting the growth of the particles. The shift is more abrupt for the first 3 min of reaction, indicating a rapid growth of the particles, whereas the diameter increases at a slower rate until 9 min reaction time, when it stops increasing further, suggesting the consumption of all the precursors.



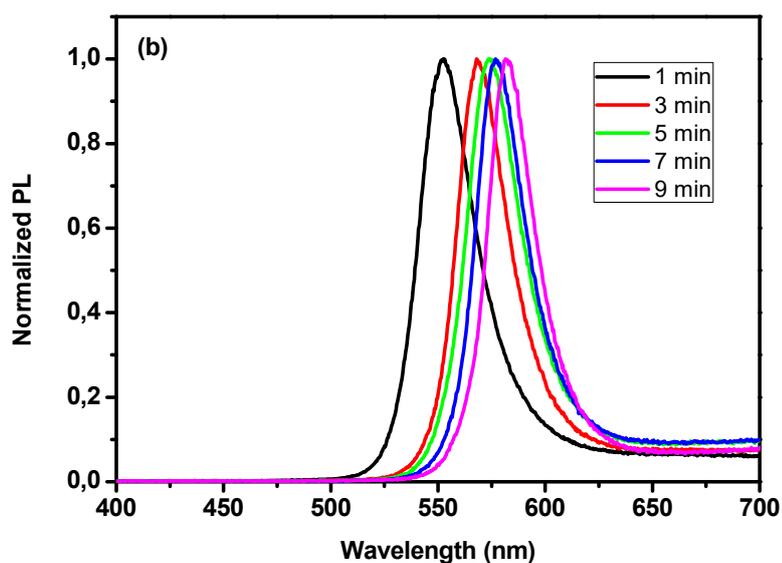


Figure 4.3. (a) Absorption spectra of the CdSe particles at different reaction times, following injection of the Se precursor solution and (b) normalized PL spectra of the same samples.

From this particle growth investigation, it was found that the particles whose optical properties matched closer the optical properties of the fabricated 3D photonic structures, were the particles at 9 min reaction time. Therefore, these nanocrystals were chosen for further growth of the CdS shell. Three monolayers of CdS were grown onto the CdSe cores, upon alternative injections of the Cd and S precursor solutions, as described in section 4.2.1.2. The UV-vis spectra of the CdSe-CdS core-shell particles are shown in Figure 4.4.

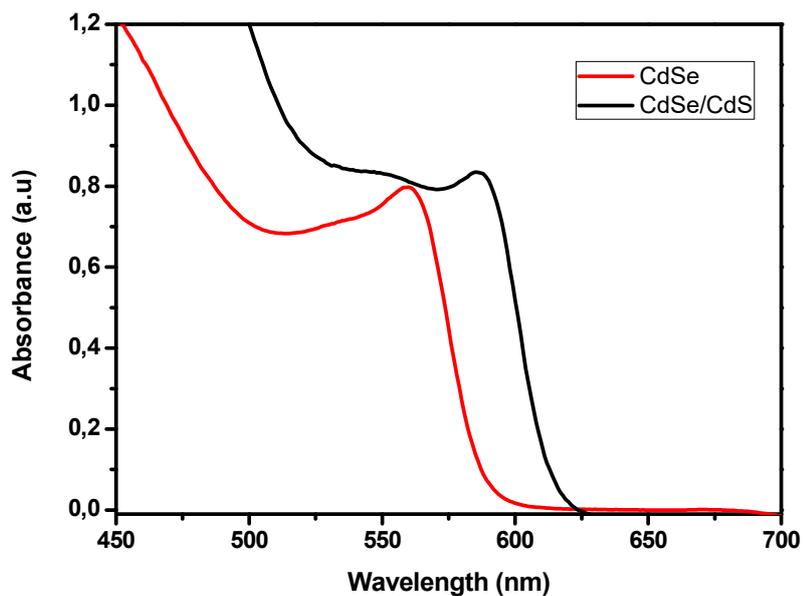


Figure 4.4. Absorption spectra of the CdSe (red line) and CdSe-CdS core-shell (black line) particles.

A clear shift in the absorbance towards longer wavelengths is observed for the core-shell particles. This phenomenon is attributed to the partial leakage of the exciton's electron into the surrounding shell and has been previously reported for CdSe-CdS and other core-shell QD systems [66], [185], [186].

TEM measurements allowed us to visualize the quantum dots and determine the average particle size and particle size distribution. Figure 4.5 shows TEM images of the CdSe core and CdSe-CdS core-shell particles with 3 monolayers of CdS. Due to the small size of the CdSe particles, the resolution of the TEM images is quite poor, whereas, the contrast enhances after the growth of the shell, resulting in a better visualization of the particles. The size distribution of the CdSe particles is shown in Figure 4.6a and the mean diameter was found 3.8 ± 0.1 nm, while the size distribution of the CdSe-CdS particles is shown in Figure 4.6b and their mean diameter was measured 5.3 ± 0.1 nm, from which the size of the shell is calculated at 1.5 nm.

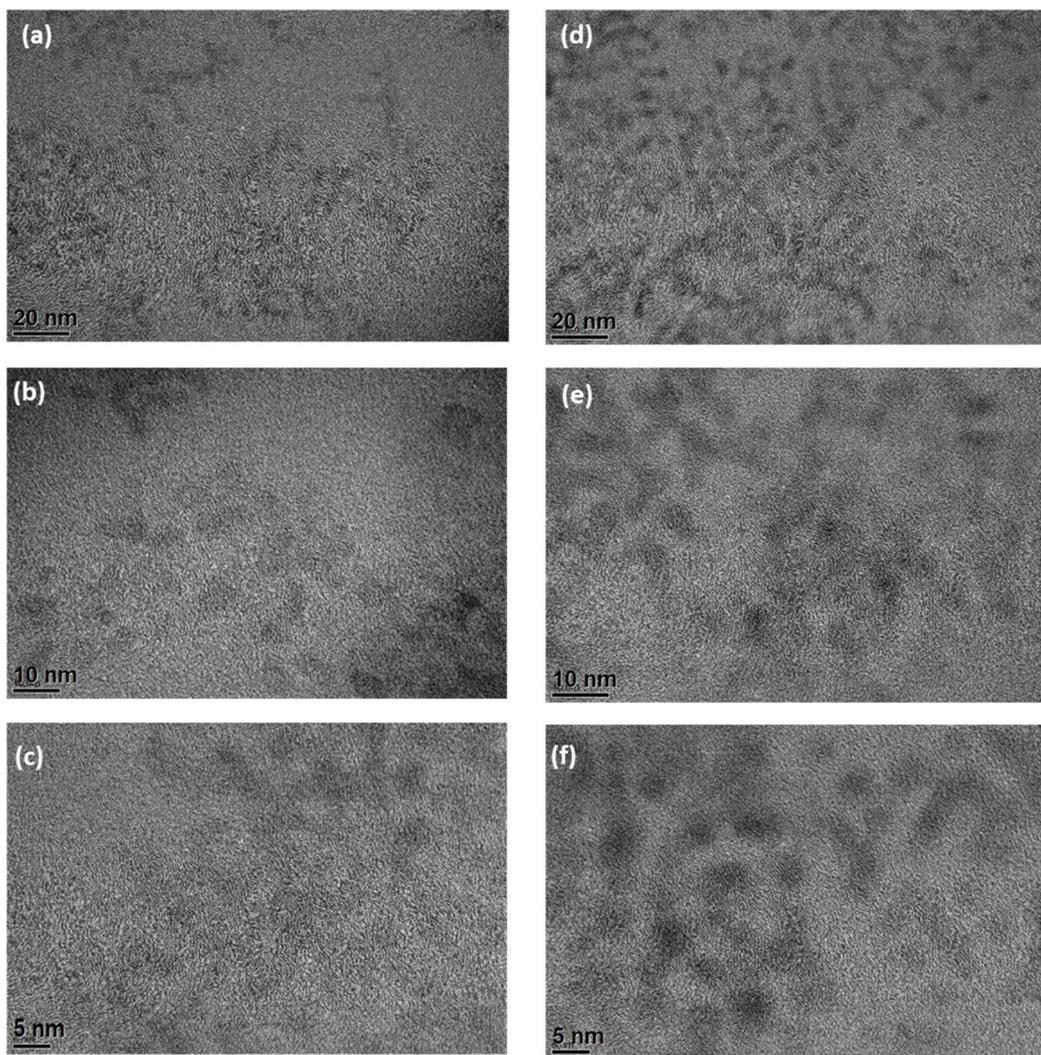


Figure 4.5. TEM images of the (a) CdSe core and the (d) CdSe-CdS core-shell particles with 3 monolayers of CdS. (b), (c) and (e), (f) are higher magnification images of (a) and (d), respectively.

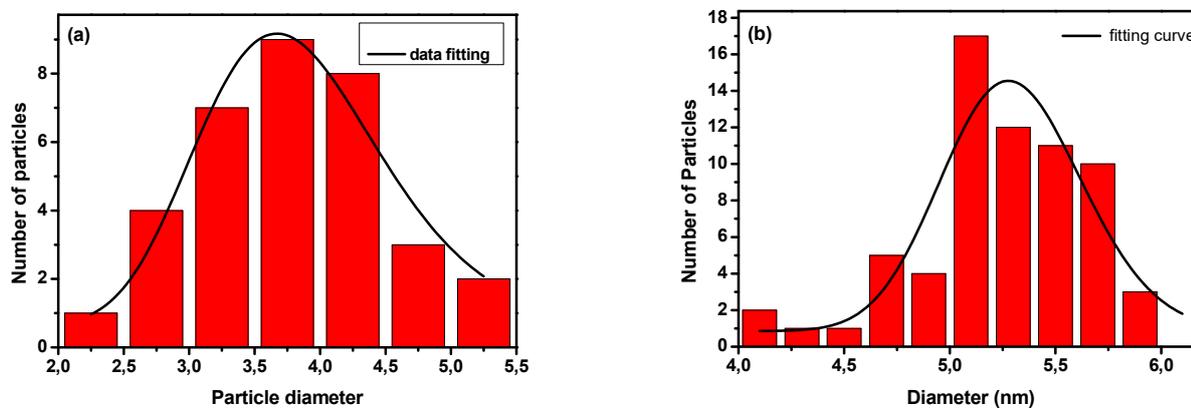


Figure 4.6. Size distribution of the (a) CdSe core ($d = 3.8 \pm 0.1$ nm) and the (b) CdSe-CdS core-shell ($d = 5.3 \pm 0.1$ nm) particles.

Following the formation of the CdS shell, the QY of the core-shell particles was measured using the relevant quantum yield method. Quantum yield (Φ) is defined as the ratio of the number of photons emitted to the number of photons absorbed by the material. Therefore, the maximum value of Φ is 1. Notably, quantum yield is independent of instrument settings and describes how efficiently a fluorophore converts the excitation light into fluorescence. In the relevant QY method, the QY of an unknown sample, the CdSe-CdS QDs in our case, is determined in relation to the QY of a known fluorescent dye.

The fundamental principle of this comparative method is that two solutions (i.e. the reference and the test sample) with identical absorbance at a specific excitation wavelength can be assumed to be absorbing the same number of photons. Therefore, provided the experimental conditions remain the same, the ratio of the integrated fluorescence intensities of the two solutions can be related to the ratio of the Φ values. In this work, six solutions were prepared; three comprised the CdSe-CdS particles in toluene and the other three were solutions of Sulforhodmine 101 (SR101) in ethanol. The choice of SR101 as the standard, is justified by the high quantum yield ($\Phi_{\text{SR101}}=0,95$) of the dye molecule, and the good overlap of its absorption and fluorescence spectra with those of the CdSe-CdS nanoparticles. The solutions were prepared in pairs of CdSe-CdS and SR101 with the same absorption at a specific wavelength, the excitation wavelength. The recorded spectra are shown in Figure 4.7. The first pair was a solution of CdSe-CdS in toluene and a solution of SR101 in ethanol with absorption 0.095 at 575 nm, the second pair comprised solutions with absorption 0.065, at the same excitation wavelength, and the third pair solutions with absorption 0.05 at the same wavelength. The concentration of all samples was low enough to ensure that the absorbance values at the excitation wavelength were below 0.1, to avoid concentration quenching problems and to remain in the linear range of the Beer-Lambert law.

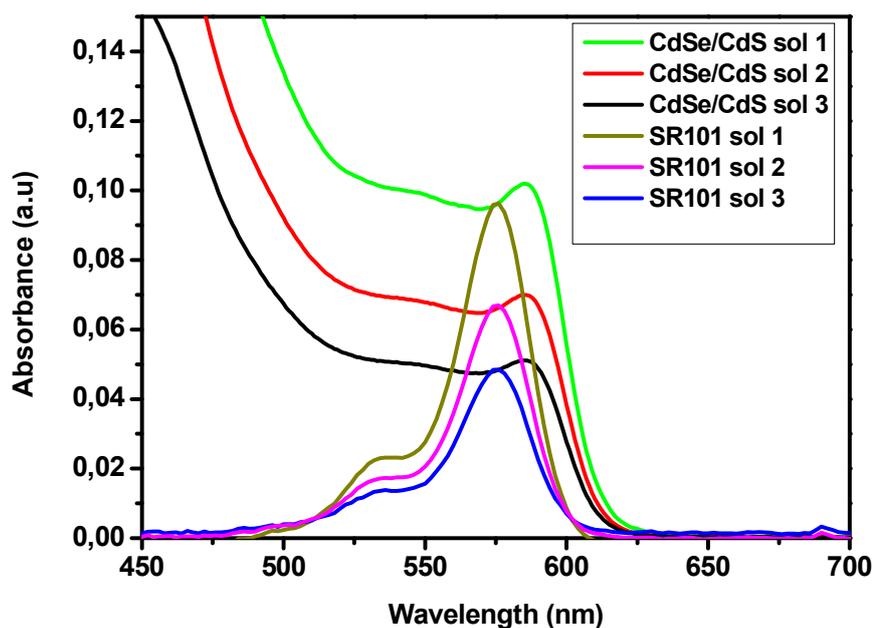
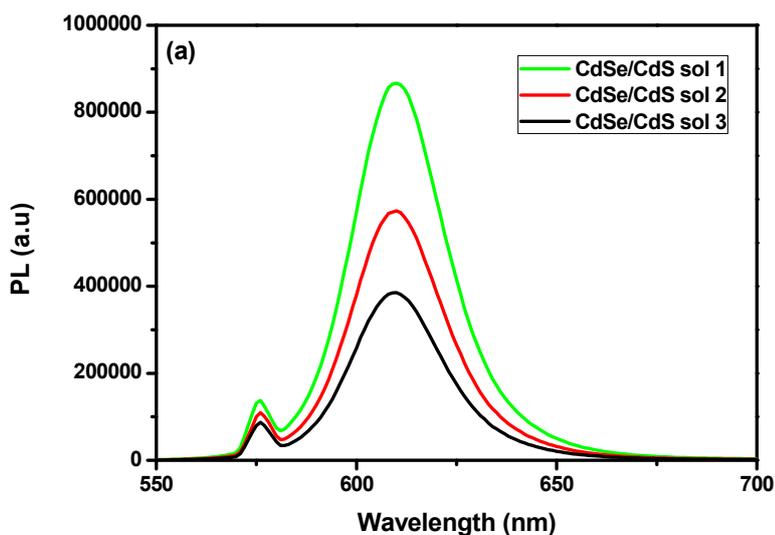


Figure 4.7. Absorption spectra of solutions of the CdSe-CdS core-shell particles and solutions of SR101 with absorption values 0.095, 0.065 and 0.05 at 565 nm.

Keeping the same absorption values at the excitation wavelength, ensures that the solutions of the CdSe-CdS quantum dots and the solutions of SR101 absorb the same number of photons. Next the PL spectra of these samples were recorded and are depicted in Figure 4.8.



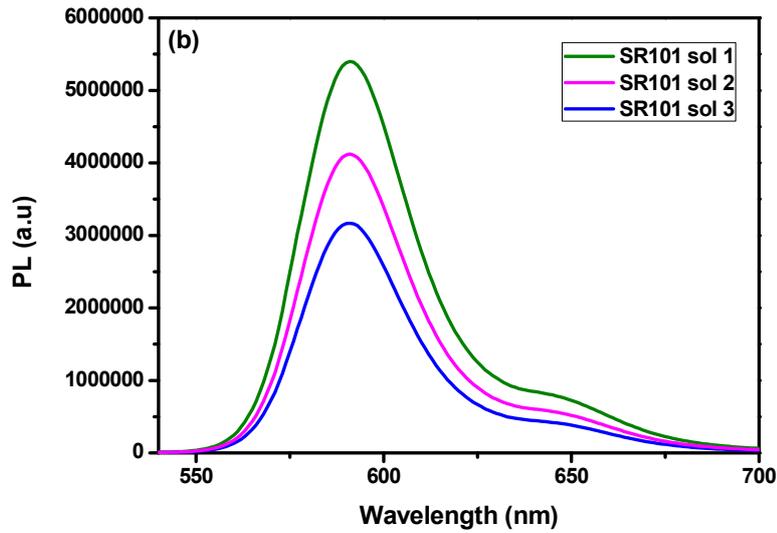


Figure 4.8. Photoluminescence (PL) spectra of the (a) CdSe-CdS solutions and the (b) SR101 solutions of different absorption values

The PL spectra were integrated and the integrated PL versus the absorption max was plotted for all three CdSe-CdS and SR101 solutions. The results are shown in figure 4.9. The QY was calculated from these values using the following equation:

$$\Phi_{\text{CdSe-CdS}} = \Phi_{\text{SR101}} \frac{\text{Grad}_{\text{CdSe-CdS}}}{\text{Grad}_{\text{SR101}}} \cdot \frac{n_{\text{toluene}}^2}{n_{\text{ethanol}}^2}$$

Where, $\Phi_{\text{CdSe-CdS}}$ and Φ_{SR101} correspond to the QY of the CdSe-CdS particles and SR101, respectively, $\text{Grad}_{\text{CdSe-CdS}}$ and $\text{Grad}_{\text{SR101}}$ correspond to the gradients obtained from the linear fit of the integrated PLs vs the absorbance max for the QDs and SR101, respectively, and n_{toluene} (1.497) and n_{ethanol} (1.361) are the refractive indices of toluene and ethanol, which served as the solvents for the quantum dots and SR101, respectively. Using this equation the QY of the CdSe-CdS particles was found:

$$\Phi_{\text{CdSe-CdS}} \sim 0,28 \text{ (28\%)} \text{ with respect to SR101}$$

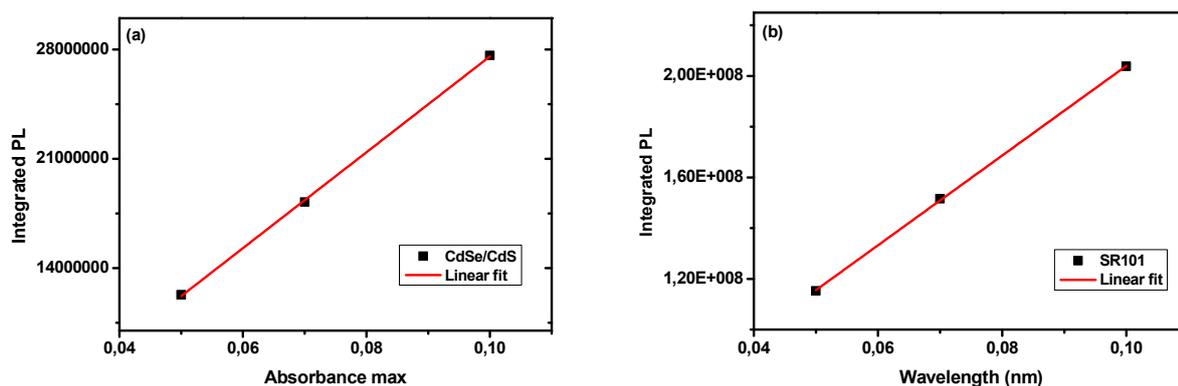


Figure 4.9. Linear fit of the integrated PL versus the absorption max for (a) the CdSe-CdS nanoparticles (slope $3,1 \cdot 10^8$) and (b) SR101 (slope $1,7 \cdot 10^9$).

Moreover, the PL lifetime of our quantum dots was determined using time-resolved pump-probe transmission measurements in a solution of the CdSe-CdS particles at room temperature, employing an amplified femtosecond Ti-Sapphire laser operating at 795 nm, with a pump pulse duration of ~ 30 fs and a pulse repetition rate of 1 kHz. Figure 4.10 shows the time-resolved spectral representation of the changes in $\Delta T/T_0$ (z-axis, color-axis) as a function of wavelength (y-axis) and the pump-probe delay time (x-axis).

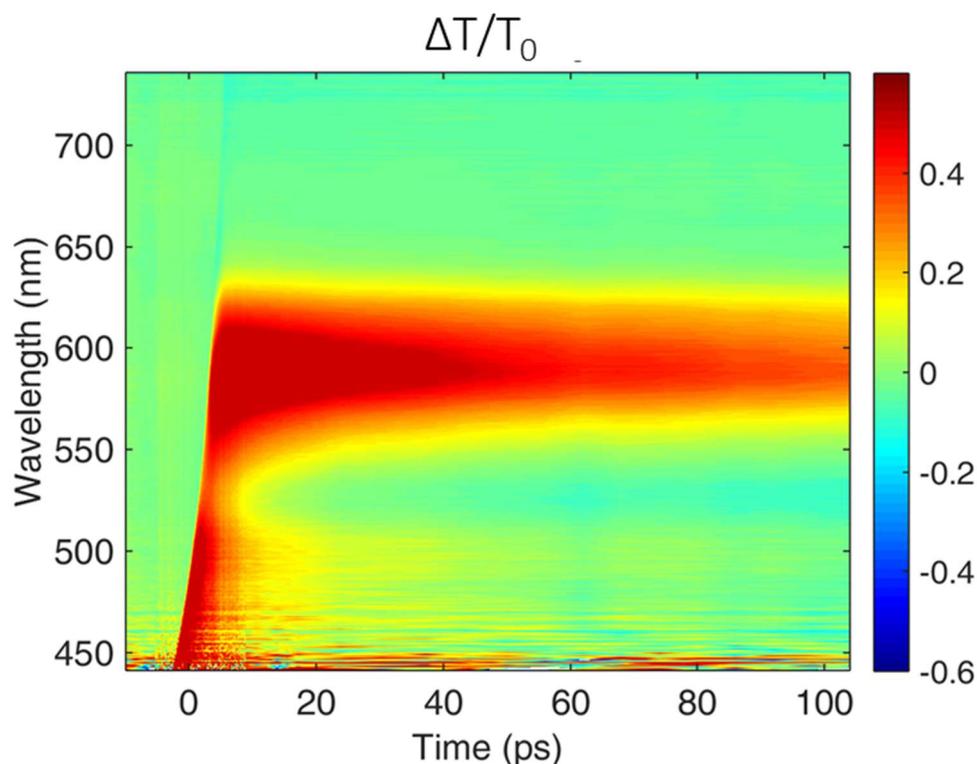


Figure 4.10. Pump-probe measurements of a solution of CdSe-CdS quantum dots showing the spectrogram of the changes in $\Delta T/T_0$ as a function of wavelength and the pump-probe delay time.

The red area in the spectrum, more pronounced between 550 and 650 nm, indicates an increase in transmission from the solution, which corresponds to the PL of the particles. By plotting the $\Delta T/T_0$ versus the delay time for a specific wavelength, the PL decay curve is extracted. This was performed for the wavelength of 600 nm and the results are shown in Figure 4.18a. From these data, the average PL lifetime can be obtained by fitting the decay with the appropriate exponential function. The analysis of the decay is a challenging task due to a lack of models for its description. A function that has often been used to fit the QD PL decay kinetics, as a convenient mathematical description of the QD PL decay, is the Kohlrausch or stretched exponential function:

$$I(t) = Ae^{(-\frac{t}{\tau})}$$

Where, $0 < A \leq 1$ and τ have the dimensions of time. According to the well-established description of the exciton structure in the most widely studied CdSe QDs, the PL decay of an ensemble of nearly monodisperse QDs at room temperature should be predominantly single exponential, $\exp(-t/\tau)$ [190]. However, this is seldomly observed experimentally. The data are typically approximated by a sum of exponentials, in most cases two, that correspond to the bright and dark exciton states, or fit to a single exponential, ignoring the long-time tails of the decays (dark excitons). The 'bright' exciton is the electron-heavy-hole pair with anti-parallel spins (emits photon), while in dark exciton the electron and heavy-hole spins are oriented parallel to each other. In this case, a single photon cannot take the total spin, and the pair is optically inactive.

In our case, the stretched exponential function showed a remarkably good fitting using the sum of two exponentials:

$$I(t) = A_1e^{(-\frac{t}{\tau_1})} + A_2e^{(-\frac{t}{\tau_2})}$$

Where, A_1 and A_2 are the intensity amplitudes of the two decays with lifetimes τ_1 and τ_2 , respectively. The results are shown in Figure 4.11b.

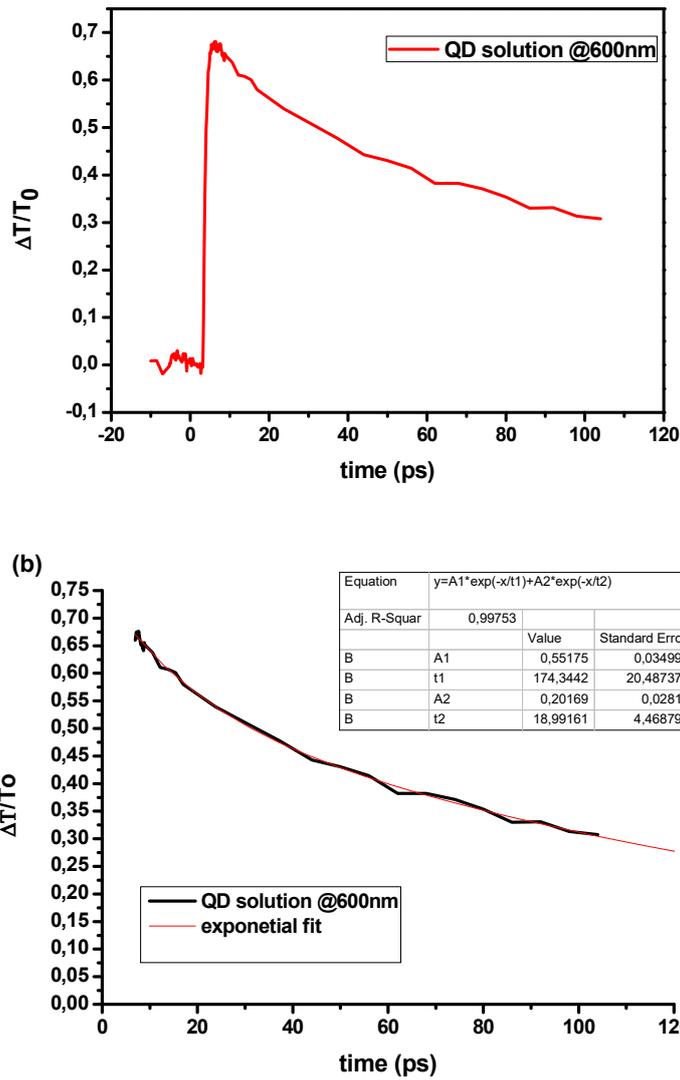


Figure 4.11. (a) PL decay curve for the solution of CdSe-CdS QDs at 600 nm (b) exponential fit using the two exponential stretched functions with $A_1=0,55175$, $\tau_1=174,3442$ s and $A_2=0,20169$, $\tau_2=18,99161$ s.

The average lifetime τ_{av} was then calculated from an intensity weighted mean:

$$\tau_{av} = \frac{A_1 \tau_1^2 + A_2 \tau_2^2}{A_1 \tau_1 + A_2 \tau_2}$$

and was found ~ 170 ps.

After their successful synthesis, the CdSe-CdS core-shell nanoparticles, were immobilized on the surface of 3D structures fabricated by the DLW technique. For this, APTES and APDES molecules (Figure 4.2) were used to functionalize the surface of the 3D structures with primary amine groups, as described in section 4.2.2. These

bifunctional molecules served as the spacers between the 3D structures and the QD nanoparticles. The hydroxysilane (-Si-OH) groups, present on the surface of the hybrid material, due to the incomplete condensation of the silane groups of MAPTMS, reacted with the alkoxy silane group of APTES/APDES, while the primary amine end-group of APTES/APDES, became attached onto the surface of the quantum dots by capping exchange the existing ligands. In order to verify that APTES/APDES was indeed chemically attached onto the 3D structures, the free primary amine groups on the 3D structures were quantified by the ninhydrine test. In this test, a primary amine group, reacts with ninhydrine (Figure 4.12) to produce a deep blue or purple color (known as Ruhemann's purple) product. An array of 4x3 3D structures of the woodpile geometry and with a fingerprint of 1 mm x 1 mm, were fabricated and were functionalized with APDES. Subsequently, they were immersed in a 0.2 % w/v ninhydrine solution in ethanol/water and were heated to 60 °C.

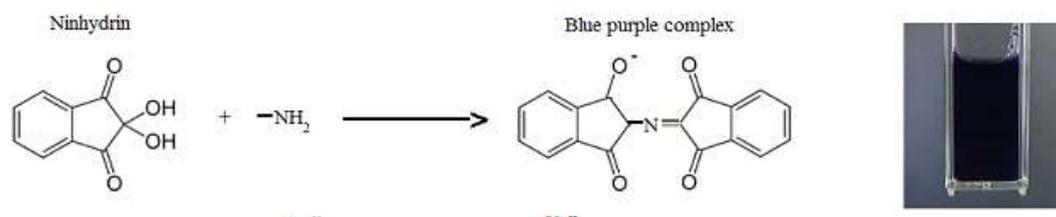


Figure 4.12. Reaction of ninhydrine with a primary amine to give a deep purple-blue colored product.

The color of the array of the 3D structures changed remarkably from pale yellow to dark blue, within a few minutes after immersion in the ninhydrine solution, verifying the presence of the primary amino groups on the surface of the 3D structures (Figure 4.13). Moreover, the structures were uniformly colored indicating that the APDES molecules covered the entire surface of the structures, which was attributed to the very large number of uncondensed hydroxysilane groups on the 3D structures following the sol-gel reaction and photopolymerization.

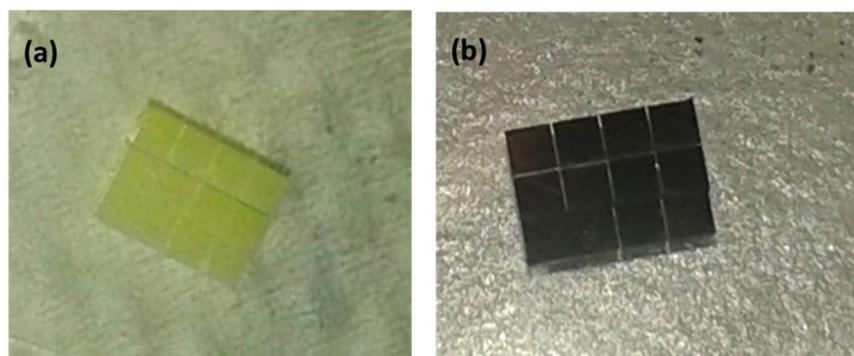


Figure 4.13. Images of a 4x3 array of 3D structures with a woodpile geometry, comprising a 1 mm x 1 mm footprint each (total covered area 4 x 3 mm²). (a) The 3D structures functionalized with APDES and (b) the same structures after reaction with ninhydrine. The dark blue color verifies the successful binding of the APDES molecules onto the surface of the 3D structures.

Next, the synthesized quantum dots were immobilized onto the amine functionalized 3D structures. Figure 4.14a shows a 1 mm x 1 mm 3D structure, with a woodpile geometry, functionalized with the QDs. EDS measurements (Figure 4.14b) revealed the presence of the Cd and Se elements, verifying the successful attachment of the QDs onto the structures. Moreover, EDS measurements taken on a cross section of the structure (Figures 4.14c and d) revealed again the presence of the Cd and Se atoms, indicating that the entire surface of the structures was covered with the nanoparticles.

Next, woodpile photonic structures of remarkably smaller size were fabricated. The woodpiles had a footprint of 50 μm x 50 μm , with an inlayer periodicity of 1 μm . Two different approaches were followed for the functionalization of these 3D structures with the QDs. In the first approach, the 3D structures were first functionalized with the APDES molecules, followed by the attachment of the QDs onto the functional structures as described above, whereas, in the second approach, the particles were first capping-exchanged with APDES, and were next attached onto non-functionalized 3D structures. After the functionalization of the 3D structures with the CdSe-CdS QDs, $\mu\text{-PL}$ measurements were performed. The set up used is described in section 4.2.4. The excitation wavelength was 543 nm and the measurements were performed at room temperature. The recorded spectra are shown in figure 4.15.

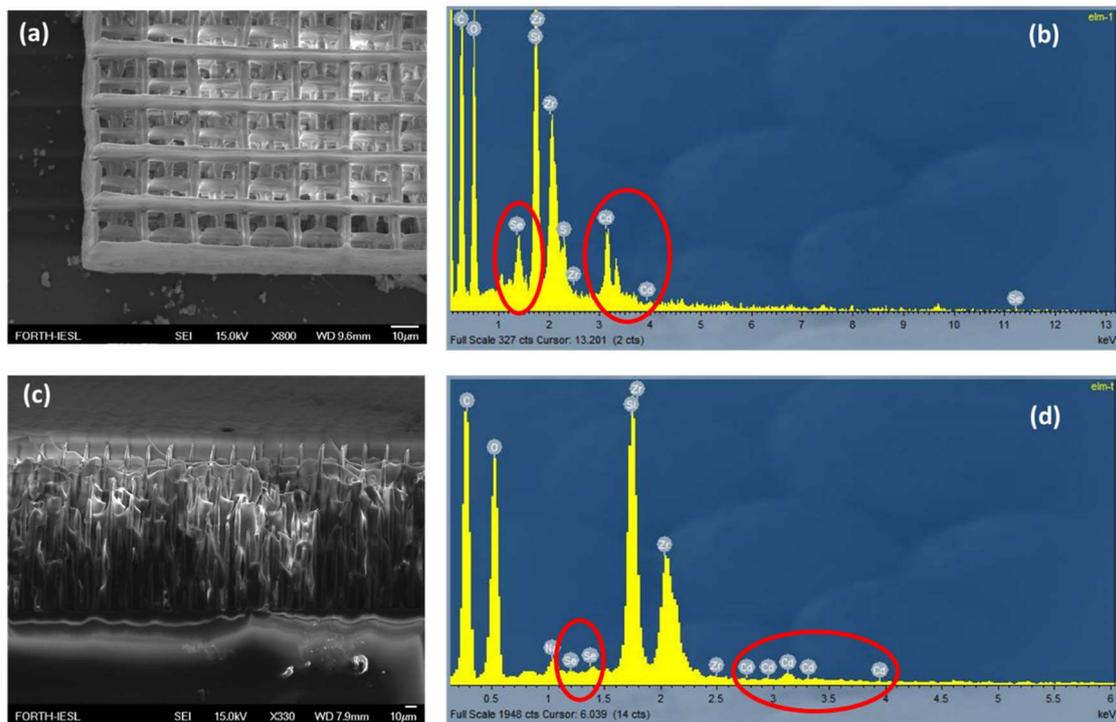


Figure 4.14. (a) SEM image of a 3D structure functionalized with the synthesized quantum dots, (b) EDS measurement taken at normal incidence reveal the presence of the Cd and Se elements, (c) cross section SEM image of the same structure and (d) EDS measurement taken on the cross sectioned part revealed again the presence of Cd and Se.

Figure 4.15a, shows the μ -PL spectra obtained on normal incidence from woodpile 3D structures with inlayer periodicity of 1 μm . The red line corresponds to the μ -PL measured on a woodpile structure with QDs which were first functionalized with APDES and then bound onto the surface of the 3D structure, whereas, the black, corresponds to the μ -PL measured on an identical structure which was first functionalized with APDES and then reacted with the QD particles. For comparison the PL spectrum from a woodpile structure, which was not functionalized with the nanoparticles, is shown in the figure (green line) and shows zero PL. As one can see, both QD functionalization strategies result in highly emissive 3D structures, at the emission wavelengths of the synthesized particles. Lower PL was found for the structure functionalized first with APDES and then reacted with the QD particles, which was attributed to possible steric hindrance effects, since the QD particles bear initially long spacers, which may prevent them from efficiently reaching the surface of the structures to interact with the APDES molecules. Figure 4.15b shows the μ -PL spectra taken from different areas of the woodpile structures mentioned above. It is evident, that all μ -PL spectra exhibit similar PL intensity values, which verifies that the QDs are

uniformly and homogeneously attached on the surface of the 3D structures. Figure 4.15c shows an image of a functionalized 3D woodpile structure under excitation with a CW laser beam of 543 nm. The emission from the particles is very high and is clearly observed by naked eye. Also, the color of the PL is in good agreement with the emission wavelength of the particles at ~ 600 nm (orange color).

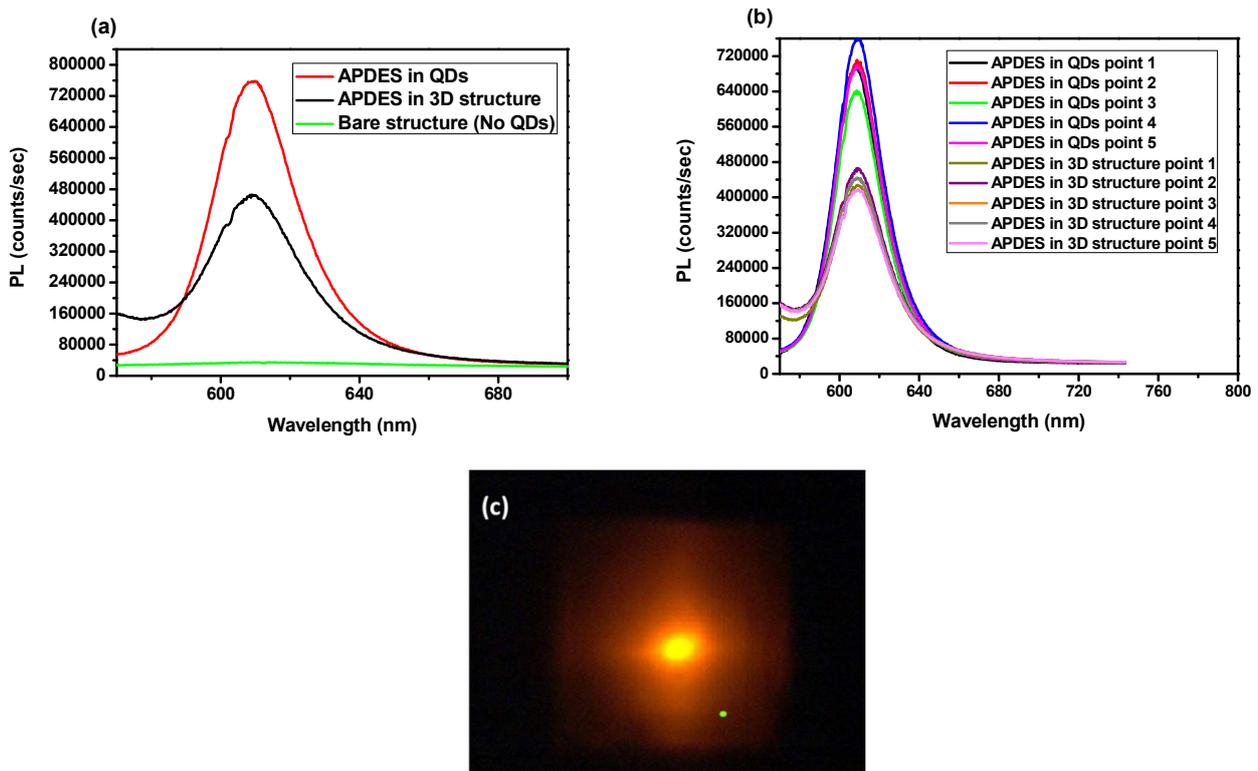


Figure 4.15. (a) μ -PL spectra taken from woodpile structures with inlayer periodicity of 1 μm . The red line corresponds to a 3D structure which was functionalized with QDs cap-exchanged with APDES, while, the black line corresponds to a 3D structure which was first functionalized with the APDES molecules and next the particles were allowed to bind onto the 3D surface. The green line corresponds to the PL of a bare structure not functionalized with QDs. (b) PL measurements at different areas of the structures described in (a). (c) Image of a QD functionalized 3D woodpile structure excited by a CW laser beam of 543 nm.

Woodpile 3D structures of much lower inlayer periodicity are required to build a photonic device that can act as a photonic crystal laser. Therefore, woodpile structures with periodicity varying from 700 nm to 500 nm were fabricated and were characterized by FTIR spectroscopy. The most appropriate structure was found that with an inlayer periodicity of 550 nm, which exhibited stop-gaps with the lower bandedge very close to the emission wavelength of the QD particles. Figure 4.16 shows SEM images of a 550

nm period structure, while Figure 4.17 shows transmission and reflection FTIR spectra taken from this structure at normal incidence.

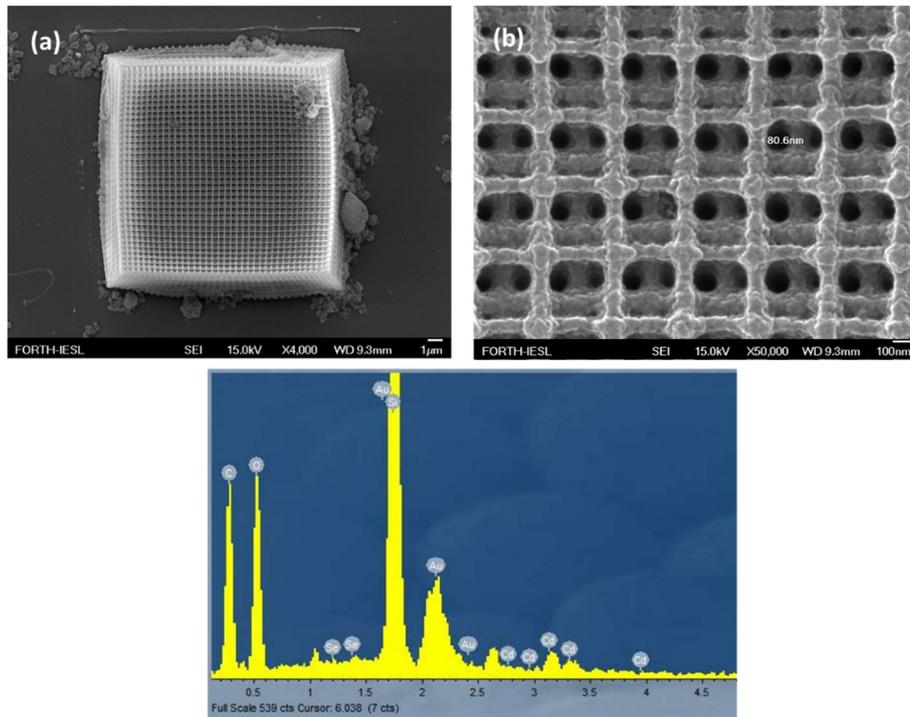


Figure 4.16. (a) SEM image of a 550 nm inlayer periodicity woodpile structure functionalized with CdSe-CdS quantum dots, (b) closer view of the same structure with minimum feature size at 80 nm and (c) EDX measurement obtained from the structure revealing the presence of Cd and Se elements.

In figure 4.17a the transmission and reflection spectra of a 45x45 nm woodpile structure with an inlayer periodicity of 550 nm are depicted. The corresponding fundamental stop band is clearly visible as a dip in the transmission and a peak in reflection centered at about 700 nm. It is also observed that the PL of the gain medium, the QDs, is located at the lower bandedge of the woodpile photonic crystal. Similar results were obtained for the 70x70 µm woodpile structure with the same periodicity, depicted in figure 4.17b. Although the bandedge is shifted towards high wavelengths (red-shift), possibly due to the lower shrinkage of this larger size structure, the PL of the particles lies at the lower bandedge of the stopband. Finally, Figure 4.17c shows the transmittance of the 70x70 µm structure before functionalization with the QDs (black line) and after functionalization with the particles (red line). It is evident that the optical response of the structure is not affected at all after the functionalization with the particles, indicating that the functionalization process does not alter the response of the photonic structures.

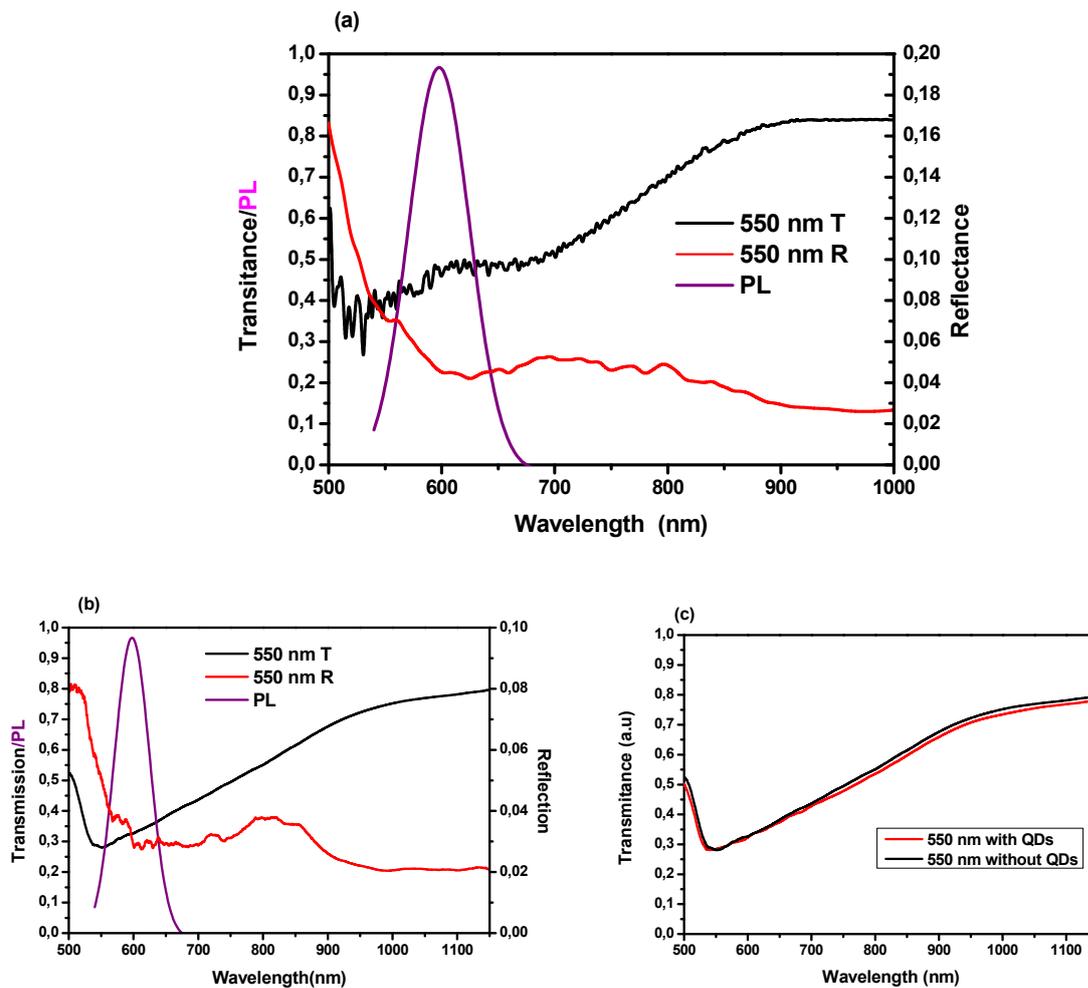


Figure 4.17. Transmission and reflection spectra at normal incidence, plotted together with the PL of the QDs (a) from a 45x45 μm 3D woodpile structure with inlayer periodicity of 550 nm (b) from a 70x70 μm woodpile structure with in layer periodicity of 550 nm (c) transmittance spectra from the 70x70 μm structure before and after its functionalization with the CdSe-CdS particles.

Next, the QD functionalized woodpile photonic crystals were pumped using the same μ-PL setup equipped with a 543-nm CW laser. The spot size covered the whole 3D structure, while the excitation intensity was increased gradually from 5 μW-205 μW (measured before the objective). Figure 4.18 shows the PL spectra recorded.

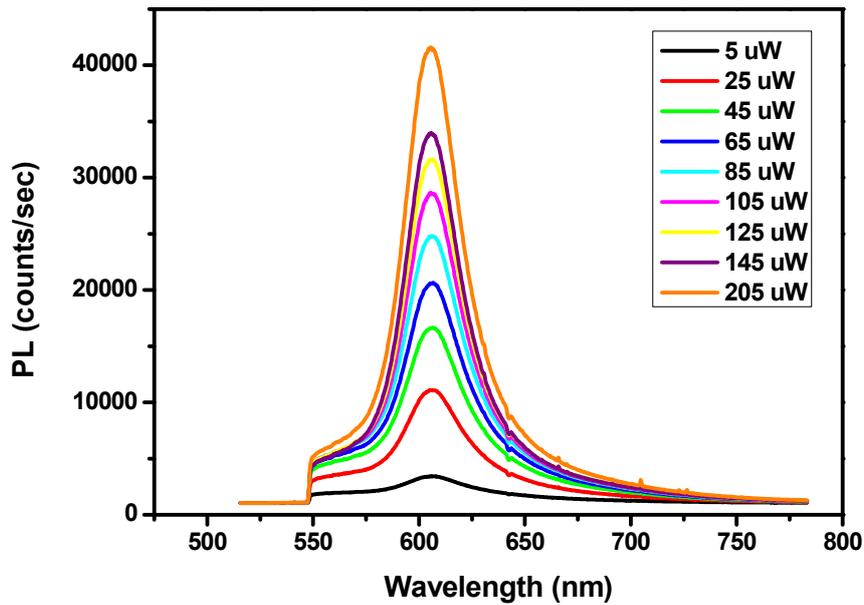


Figure 4.18. μ -PL spectra recorded after pumping the QD containing 3D photonic structures at increasing pump intensity.

From figure 4.18 it is evident that as the pump power increases, the PL intensity also increases. This result is anticipated, since a higher excitation power will result to higher PL values. With increasing pump power it is expected that the system will reach the lasing threshold at some point, which is the characteristic pump power above which the emitted light is characterized by a dramatic power increase and spectral narrowing (down to a few nanometers). However, in our case even for an excitation power of 205 μ W, the maximum output of the laser, no lasing action is observed and the PL increases linearly with the power. An obvious reason for this result would be that the excitation power, even at the maximum output of the pump laser, is still below the lasing threshold. However, we strongly believe that the possible reason for which we do not observe lasing in our system is the excitation source itself. Literature reports on similar systems (photonic crystals with gain medium), have employed pulsed lasers as the excitation sources with a minimum pulse duration of the order of nanoseconds [15], [170], [173]–[175], [187]–[189]. Thus, we strongly believe that one of the reasons affecting the non lasing action in our system is the pump source. The most appropriate excitation source in our case would be a pulsed laser, to effectively pump the system. The CW laser used in this study, has the advantage of providing energy at a constant way, but lacks a high excitation peak power. Thus, it would be more appropriate to use a

pulsed laser as the excitation source since it will exhibit a high intensity peak power which could result in more effective gain.

4.4 Conclusions

We have demonstrated the synthesis of highly luminescent CdSe-CdS core-shell quantum dots and the fabrication of high-resolution woodpile photonic crystals using the multi-photon lithography technique. The woodpile structures, show clear stop-gaps at visible wavelengths. Moreover, the organic-inorganic nature of the materials that we used for the fabrication of the structures, allowed us to modify their surface with functional molecules that act as binding sites for the chemical immobilization of the synthesized quantum dots onto the surface of the 3D photonic crystals. This functionalization process is simple, and does not require the use of high temperatures, allowing its application to any kind of nanoparticles using the same or different functional molecules. The QD particles can act as a gain medium on the photonic structures, enriching the structures with high emission properties. For this reason, the emission of the quantum dots was designed to lie at the same wavelengths of the bandedges of the stopgaps of the photonic structures, resulting in a device that could act as a photonic crystal laser.

Preliminary lasing experiments, with a CW laser excitation source, did not show any amplified spontaneous emission from the structures and further studies are required using other excitation sources. The most appropriate excitation source for such a device would be a pulsed laser, able to provide high pumping intensities to the system.

Overall, we have demonstrated a simple and cost effective generic route for the realization of functional devices that are not limited to the use of the specific hybrid materials and/or the quantum dots presented herein. Any material, organic, inorganic or hybrid, comprising surface functional groups could be employed and any type of semiconductor nanoparticles could replace our CdSe-CdS particles. Alternative spacer molecules, to replace APDES, and orthogonal chemistries, would be required to chemically bind any kind of metallic nanoparticles onto 1D, 2D and 3D fabricated structures.

Conclusions and future perspectives

Three-dimensional (3D) printing is a massive trend worldwide. Some predict that in a decade 10% of all manufactured products could be 3D printed. Eventually, it might be possible to 3D print any functional device with features ranging from the molecular to the macroscopic scale “at the push of a button”. Consequently, 3D printing has gained considerable attention in industrial fabrication. Before reaching the consumer market, these technologies could also enable many scientific developments.

In this work we have focused on the synthesis of novel photosensitive materials that can be applied to laser-based (Direct Laser Writing) 3D printing approaches for specific applications. In particular, DLW of the materials, by multi-photon polymerization, has been employed for the realization of 3D structures that exhibit active optical properties.

In the first part of the work (Chapter 2), we have shown the synthesis of a new photoactive material that demonstrates for the first time a redox multiphoton polymerization initiation mechanism, in which a vanadium alkoxide complex acts as both the photoinitiator and as one of the components of the organic–inorganic composite. The material self-generates radicals by multiphoton absorption, accompanied by a simultaneous reduction of vanadium (V) to vanadium (IV). Fully 3D structures, with 200 nm resolution, were fabricated from this material employing a femtosecond laser operating at 800 nm. In addition, nonlinear optical measurements performed by means of the z-scan method, showed that the photoinitiation is most likely due to three-photon absorption of the vanadium species. The three-photon absorption coefficient of the material was measured $\sigma_3 = 3.0 \times 10^{-80} \text{ cm}^6 \cdot \text{s}^2$, comparable to those of standard three-photon absorbers. However, since it is possible to load the composite with as much as 50% molar vanadium complex, the efficiency of the three-photon polymerization process of the investigated composite is comparable with that of a two-photon polymerization of other standard materials containing excess photoinitiator.

In Chapter 3, we discuss the modification of a hybrid photosensitive material, which has been extensively used by our team, with a monomer that can act as a quantum dot precursor for the in situ synthesis of CdS nanoparticles within the fabricated 3D photonic structures. The novel active, 3D printable, hybrid material synthesized

exhibits a high nonlinear refractive index value measured by means of Z-scan method, whereas the fabricated woodpile structures show clear photonic stop bands in the visible wavelength region. By means of time-resolved pump-probe spectroscopy, evidence of a photonic band gap shift was demonstrated.

Finally, in Chapter 4 the synthesis of CdSe-CdS quantum dots and their successful immobilization on the surface of 3D high resolution photonic devices is shown. The approach is based on the exploitation of the surface chemistry of both the 3D structures and the QD nanoparticles. The high emission efficiency of these particles which lies at the wavelengths of the bandedges of the stopgaps of the photonic structures renders them ideal candidates for use as the gain medium in 3D lasing applications.

The main aim of this work was the design of functional materials for the realization of active devices for optical applications. Functional devices often require materials with appropriate electrical, magnetic, optical, mechanical and chemical properties. Although some of these properties have been attained by 3D laser writing of existing materials, other important material properties are currently out of reach and require significant research efforts for their realization. Examples are mechanically compliant and chemically functionalized materials as well as semiconducting and conducting materials for optoelectronics. In all these cases, adaptive materials are highly desirable. Our work on 3D photonic structures functionalized with semiconductor nanoparticles falls exactly in this area. For the in situ synthesis of the CdS nanoparticles within the 3D photonic devices, although a clear ultrafast dynamic response was recorded from the woodpile photonic structures, which indicates a photonic band gap shift, further experiments are required to identify the competing ultrafast all-optical switching mechanisms that take place between the 3D polymer photonic matrix and the functionalized QDs. This will also enable the comprehensive understanding of the underlying mechanisms and will allow to reach more solid conclusions. Such complementary experiments are planned as part of the future work of this study. In this context, more stable QDs systems need to be developed with narrow size distribution, as well as enhanced resistance to photo-bleaching, for application in ultrafast all-optical switching. For the study involving the surface functionalization of 3D photonic crystals with highly emissive quantum dot particles, preliminary experiments involving a CW laser as the pump source did not exhibit any lasing action. Despite this fact, more extensive and comprehensive studies are essential to examine the system in detail. The CW laser used so far, has the advantage of providing energy at a constant

fluence, but lacks a high excitation peak power. We believe that it would be more appropriate to use pulsed lasers as the excitation source, because they exhibit a high intensity peak power which could result in more effective gain. Moreover, further experiments should be performed to verify that the gain material is sufficient to provide effective gain. Finally, the losses of the photonic structure itself should be examined to verify that extensive losses from the structure are not inhibiting the lasing action.

Another major challenge in DLW is to achieve high writing speeds, because overall volumes of cubic centimeters, with sub-micrometer or nanometer feature sizes, are often required to 3D print functional devices for certain applications. The overall required optical laser power increases with the square root of the scanning speed, and therefore, for acceptable optical laser powers, more efficient (two-photon) photoinitiator molecules and mechanisms are highly desirable. It thus becomes evident that highly sensitive photoresists are increasingly required. The vanadium composite material synthesized in this work, could serve as an ideal candidate to overcome the writing speed challenge. The high vanadium alkoxide loading of the material, leads to a highly efficient 3-photon polymerization process, which is comparable to the 2-photon polymerization efficiency of most well-known composite materials. As part of the future work of this study, the two-photon DLW efficiency of this composite, using the appropriate laser source, should be investigated, and the maximum writing speeds attained should be explored in the fabrication of large size functional devices.

References

- [1] C. J. Brinker and G. W. Scherrer, *Sol-Gel Science The physics and chemistry of sol-gel processing*. Academic Press, 1990.
- [2] B. N. Chichkov and A. Ostendorf, “Two-Photon Polymerization: A New Approach to Micromachining,” *Photonics Spectra*, no. October, 2006.
- [3] H. Sun and S. Kawata, “Two-Photon Photopolymerization and 3D Lithographic Microfabrication,” *Quantum*, pp. 169–274, 2004.
- [4] K.-S. Lee, D.-Y. Yang, S. H. Park, and R. H. Kim, “Recent developments in the use of two-photon polymerization in precise 2D and 3D microfabrications,” *Polym. Adv. Technol.*, vol. 17, no. 2, pp. 72–82, Feb. 2006.
- [5] G. Filippidis, J. Catherine, M. Farsari, V. Zorba, and C. Fotakis, “Construction of micron three-dimensional structures employing multi-photon polymerization,” *Proc. Inst. Mech. Eng. Part N J. Nanoeng. Nanosyst.*, vol. 219, no. 4, pp. 165–168, Jan. 2005.
- [6] J. Serbin, a Egbert, a Ostendorf, B. N. Chichkov, R. Houbertz, G. Domann, J. Schulz, C. Cronauer, L. Fröhlich, and M. Popall, “Femtosecond laser-induced two-photon polymerization of inorganic-organic hybrid materials for applications in photonics.,” *Opt. Lett.*, vol. 28, no. 5, pp. 301–3, Mar. 2003.
- [7] A. Ovsianikov, A. Gaidukeviciute, B. N. Chichkov, M. Oubaha, B. D. MacCraith, I. Sakellari, A. Giakoumaki, D. Gray, M. Vamvakaki, M. Farsari, and C. Fotakis, “Two-Photon Polymerization of Hybrid Sol-Gel Materials for Photonics Applications,” *Laser Chem.*, vol. 2008, pp. 1–7, 2008.
- [8] M. Malinauskas, A. Gaidukevičiūtė, V. Purlys, A. Žukauskas, I. Sakellari, E. Kabouraki, A. Candiani, D. Gray, S. Pissadakis, R. Gadonas, A. Piskarskas, C. Fotakis, M. Vamvakaki, and M. Farsari, “Direct laser writing of microoptical structures using a Ge-containing hybrid material,” *Metamaterials*, vol. 5, no. 2–3, pp. 135–140, Jun. 2011.
- [9] A. Ovsianikov, A. Ostendorf, and B. N. Chichkov, “Three-dimensional photofabrication with femtosecond lasers for applications in photonics and biomedicine,” *Appl. Surf. Sci.*, vol. 253, no. 15, pp. 6599–6602, May 2007.
- [10] A. Ovsianikov, S. Schlie, A. Ngezahayo, A. Haverich, and B. N. Chichkov, “Two-photon polymerization technique for microfabrication of CAD-designed 3D scaffolds from commercially available photosensitive materials,” *J. Tissue Eng. Regen. Med.*, vol. 1, pp. 443–449, 2008.
- [11] V. Melissinaki, A. A. Gill, I. Ortega, M. Vamvakaki, A. Ranella, J. W. Haycock, C. Fotakis, M. Farsari, and F. Claeysens, “Direct laser writing of 3D scaffolds for neural tissue engineering applications.,” *Biofabrication*, vol. 3, no. 4, p. 045005, Dec. 2011.

- [12] R. Guo, Z. Li, Z. Jiang, D. Yuan, W. Huang, and A. Xia, "Log-pile photonic crystal fabricated by two-photon photopolymerization," *J. Opt. A Pure Appl. Opt.*, vol. 7, no. 8, pp. 396–399, Aug. 2005.
- [13] S. Psycharakis, A. Tosca, V. Melissinaki, A. Giakoumaki, and A. Ranella, "Tailor-made three-dimensional hybrid scaffolds for cell cultures," *Biomed. Mater.*, vol. 6, no. 4, p. 045008, Aug. 2011.
- [14] B. Jia, D. Buso, J. van Embden, J. Li, and M. Gu, "Highly non-linear quantum dot doped nanocomposites for functional three-dimensional structures generated by two-photon polymerization," *Adv. Mater.*, vol. 22, no. 22, pp. 2463–7, Jun. 2010.
- [15] P. Reiss, M. Protière, and L. Li, "Core/shell semiconductor nanocrystals," *Small*, vol. 5, no. 2, pp. 154–168, 2009.
- [16] S. H. Wei and A. Zunger, "Calculated natural band offsets of all II-VI and III-V semiconductors: Chemical trends and the role of cation d orbitals," *Appl. Phys. Lett.*, vol. 72, no. 16, pp. 2011–2013, 1998.
- [17] C. J. Murphy and J. L. Coffey, "QuantumDots: A Primer," *Appl. Spectrosc.*, vol. 56, no. 1, p. 16A–27A, 2002.
- [18] S. V. Gaponenko, *Introduction to Nanophotonics*. Cambridge University press, 2010.
- [19] T. Kippeny, L. A. Swafford, and S. J. Rosenthal, "Semiconductor Nanocrystals: A Powerful Visual Aid for Introducing the Particle in a Box," *J. Chem. Educ.*, vol. 79, no. 9, p. 1094, Sep. 2002.
- [20] C. R. Kagan, E. Lifshitz, E. H. Sargent, and D. V. Talapin, "Building devices from colloidal quantum dots," *Science (80-.)*, vol. 353, no. 6302, 2016.
- [21] L. E. Brus, "A simple model for the ionization potential, electron affinity, and aqueous redox potentials of small semiconductor crystallites," *J. Chem. Phys.*, vol. 79, no. 11, pp. 5566–5571, 1983.
- [22] L. E. Brus, "Electron-electron and electron-hole interactions in small semiconductor crystallites: The size dependence of the lowest excited electronic state," *J. Chem. Phys.*, vol. 80, no. 9, pp. 4403–4409, 1984.
- [23] A. Ekimov, Onushcheko, "Quantum Size Effect in Three-Dimensional Microscopic Semiconductor Crystals," *ZhETF Pisma Redaktsiiu*, vol. 34, no. 06, pp. 345–348, 1981.
- [24] E. Chason, S. T. Picraux, J. M. Poate, J. O. Borland, M. I. Current, T. Diaz de la Rubia, D. J. Eaglesham, O. W. Holland, M. E. Law, C. W. Magee, J. W. Mayer, J. Melngailis, and A. F. Tasch, "Ion beams in silicon processing and characterization," *J. Appl. Phys.*, vol. 81, no. 10, pp. 6513–6561, May 1997.
- [25] V. L. Colvin, A. N. Goldstein, and A. P. Alivisatos, "Semiconductor nanocrystals covalently bound to metal surfaces with self-assembled monolayers," *J. Am. Chem. Soc.*, vol. 114, no. 13, pp. 5221–5230, Jun. 1992.

- [26] A. R. Kortan, R. Hull, R. L. Opila, M. G. Bawendi, M. L. Steigerwald, P. J. Carroll, and L. E. Brus, "Nucleation and Growth of CdSe on ZnS Quantum Crystallite Seeds, and Vice Versa, in Inverse Micelle Media," *J. Am. Chem. Soc.*, vol. 112, no. 4, pp. 1327–1332, Feb. 1990.
- [27] G. N. Karanikolos, P. Alexandridis, G. Itkos, A. Athos Petrou, and T. J. Mountziaris, "Synthesis and Size Control of Luminescent ZnSe Nanocrystals by a Microemulsion–Gas Contacting Technique," *Langmuir*, vol. 20, pp. 550–553, 2004.
- [28] E. Kuçur, W. Bücking, R. Giernoth, and T. Nann, "Determination of Defect States in Semiconductor Nanocrystals by Cyclic Voltammetry," *J. Phys. Chem. B*, vol. 109, no. 43, pp. 20355–20360, Nov. 2005.
- [29] D. Bera, L. Qian, S. Sabui, S. Santra, and P. H. Holloway, "Photoluminescence of ZnO quantum dots produced by a sol–gel process," *Opt. Mater. (Amst.)*, vol. 30, no. 8, pp. 1233–1239, Apr. 2008.
- [30] L. Spanhel and M. A. Anderson, "Semiconductor clusters in the sol-gel process: quantized aggregation, gelation, and crystal growth in concentrated zinc oxide colloids," *J. Am. Chem. Soc.*, vol. 113, no. 8, pp. 2826–2833, Apr. 1991.
- [31] C. B. Murray, D. J. Norris, and M. G. Bawendi, "Synthesis and characterization of nearly monodisperse CdE (E = sulfur, selenium, tellurium) semiconductor nanocrystallites," *J. Am. Chem. Soc.*, vol. 115, no. 19, pp. 8706–8715, Sep. 1993.
- [32] D. Leonard, M. Krishnamurthy, C. M. Reaves, S. P. Denbaars, and P. M. Petroff, "Direct formation of quantum-sized dots from uniform coherent islands of InGaAs on GaAs surfaces," *Appl. Phys. Lett.*, vol. 63, no. 23, pp. 3203–3205, Dec. 1993.
- [33] K. Leonardi, H. Selke, H. Heinke, K. Ohkawa, D. Hommel, F. Gindele, and U. Woggon, "Formation of self-assembling II–VI semiconductor nanostructures during migration enhanced epitaxy," *J. Cryst. Growth*, vol. 184–185, pp. 259–263, Feb. 1998.
- [34] S. H. Xin, P. D. Wang, A. Yin, C. Kim, M. Dobrowolska, J. L. Merz, and J. K. Furdyna, "Formation of self-assembling CdSe quantum dots on ZnSe by molecular beam epitaxy," *Appl. Phys. Lett.*, vol. 69, no. 25, pp. 3884–3886, Dec. 1996.
- [35] E. Kurtz, J. Shen, M. Schmidt, M. Grün, S. K. Hong, D. Litvinov, D. Gerthsen, T. Oka, T. Yao, and C. Klingshirn, "Formation and properties of self-organized II–VI quantum islands," *Thin Solid Films*, vol. 367, no. 1–2, pp. 68–74, May 2000.
- [36] M. T. Swihart, "Vapor-phase synthesis of nanoparticles," *Curr. Opin. Colloid Interface Sci.*, vol. 8, no. 1, pp. 127–133, Mar. 2003.
- [37] C. Burda, X. Chen, R. Narayanan, and M. A. El-Sayed, "Chemistry and Properties of Nanocrystals of Different Shapes," *Chem. Rev.*, vol. 105, no. 4, pp. 1025–1102, Apr. 2005.
- [38] C. Lobo and R. Leon, "InGaAs island shapes and adatom migration behavior on (100),

- (110), (111), and (311) GaAs surfaces,” *J. Appl. Phys.*, vol. 83, no. 8, pp. 4168–4172, Apr. 1998.
- [39] R. J. Ellingson, M. C. Beard, J. C. Johnson, P. Yu, O. I. Micic, A. J. Nozik, A. Shabaev, and A. L. Efros, “Highly efficient multiple exciton generation in colloidal PbSe and PbS quantum dots,” *Nano Lett.*, vol. 5, no. 5, pp. 865–871, 2005.
- [40] M. A. Hines and G. D. Scholes, “Colloidal PbS Nanocrystals with Size-Tunable Near-Infrared Emission: Observation of Post-Synthesis Self-Narrowing of the Particle Size Distribution,” *Adv. Mater.*, vol. 15, no. 21, pp. 1844–1849, Nov. 2003.
- [41] L. Qu, Z. A. Peng, and X. Peng, “Alternative Routes toward High Quality CdSe Nanocrystals,” *Nano Lett.*, vol. 1, no. 6, pp. 333–337, 2001.
- [42] L. Qu and X. Peng, “Control of photoluminescence properties of CdSe nanocrystals in growth,” *J. Am. Chem. Soc.*, vol. 124, no. 9, pp. 2049–2055, 2002.
- [43] H. Lee, P. H. Holloway, and H. Yang, “Synthesis and characterization of colloidal ternary ZnCdSe semiconductor nanorods,” *J. Chem. Phys.*, vol. 125, no. 16, 2006.
- [44] Y. Bae, N. Myung, and A. J. Bard, “Electrochemistry and electrogenerated chemiluminescence of CdTe nanoparticles,” *Nano Lett.*, vol. 4, no. 6, pp. 1153–1161, 2004.
- [45] M. A. Hines and P. Guyot-Sionnest, “Bright UV-Blue Luminescent Colloidal ZnSe Nanocrystals,” *J. Phys. Chem. B*, vol. 102, no. 19, pp. 3655–3657, 1998.
- [46] W. W. Yu, Y. A. Wang, and X. Peng, “Formation and Stability of Size-, Shape-, and Structure-Controlled CdTe Nanocrystals: Ligand Effects on Monomers and Nanocrystals,” *Chem. Mater.*, vol. 15, no. 22, pp. 4300–4308, 2003.
- [47] L. Bakueva, S. Musikhin, M. A. Hines, T.-W. F. Chang, M. Tzolov, G. D. Scholes, and E. H. Sargent, “Size-tunable infrared (1000–1600 nm) electroluminescence from PbS quantum-dot nanocrystals in a semiconducting polymer,” *Appl. Phys. Lett.*, vol. 82, no. 17, pp. 2895–2897, Apr. 2003.
- [48] D. Battaglia and X. Peng, “Formation of High Quality InP and InAs Nanocrystals in a Noncoordinating Solvent,” *Nano Lett.*, vol. 2, no. 9, pp. 1027–1030, 2002.
- [49] D. V. Talapin, A. L. Rogach, A. Kornowski, M. Haase, and H. Weller, “Highly Luminescent Monodisperse CdSe and CdSe/ZnS Nanocrystals Synthesized in a Hexadecylamine-Trioctylphosphine Oxide-Trioctylphosphine Mixture,” *Nano Lett.*, vol. 1, no. 4, pp. 207–211, 2001.
- [50] W. K. Bae, M. K. Nam, K. Char, and S. Lee, “Gram-scale one-pot synthesis of highly luminescent blue emitting Cd_{1-x}Zn_xS/ZnS nanocrystals,” *Chem. Mater.*, vol. 20, no. 16, pp. 5307–5313, 2008.
- [51] X. Zhong, M. Han, Z. Dong, T. J. White, and W. Knoll, “Composition-tunable Zn_xCd_{1-x}Se nanocrystals with high luminescence and stability,” *J. Am. Chem. Soc.*, vol. 125,

- no. 28, pp. 8589–8594, 2003.
- [52] V. Poderys, M. Matulionyte, A. Selskis, and R. Rotomskis, “Interaction of Water-Soluble CdTe Quantum Dots with Bovine Serum Albumin.,” *Nanoscale Res. Lett.*, vol. 6, no. 1, p. 9, Dec. 2011.
- [53] W. T. Mason, *Fluorescent and luminescent probes for biological activity : a practical guide to technology for quantitative real-time analysis*. Academic Press, 1999.
- [54] C. Wang, X. Gao, Q. Ma, and X. Su, “Aqueous synthesis of mercaptopropionic acid capped Mn²⁺-doped ZnSe quantum dots,” *J. Mater. Chem.*, vol. 19, no. 38, p. 7016, Sep. 2009.
- [55] M. N. Kalasad, M. K. Rabinal, and B. G. Mulimani, “Ambient Synthesis and Characterization of High-Quality CdSe Quantum Dots by an Aqueous Route,” *Langmuir*, vol. 25, no. 21, pp. 12729–12735, Nov. 2009.
- [56] R. Kho, C. L. Torres-Martínez, and R. K. Mehra, “A Simple Colloidal Synthesis for Gram-Quantity Production of Water-Soluble ZnS Nanocrystal Powders,” *J. Colloid Interface Sci.*, vol. 227, no. 2, pp. 561–566, Jul. 2000.
- [57] J.-H. Liu, J.-B. Fan, Z. Gu, J. Cui, X.-B. Xu, Z.-W. Liang, S.-L. Luo, and M.-Q. Zhu, “Green Chemistry for Large-Scale Synthesis of Semiconductor Quantum Dots,” *Langmuir*, vol. 24, no. 10, pp. 5241–5244, May 2008.
- [58] Gia-Wei Shu, Wan-Zhen Lee, I.-J. Shu, Ji-Lin Shen, James Cheng-An Lin, W. H. Chang, Ruoh-Chyu Ruaan, and Wu Ching Chou, “Photoluminescence of colloidal CdSe/ZnS quantum dots under oxygen atmosphere,” *IEEE Trans. Nanotechnol.*, vol. 4, no. 5, pp. 632–636, Sep. 2005.
- [59] S. Sapra, A. L. Rogach, and J. Feldmann, “Phosphine-free synthesis of monodisperse CdSe nanocrystals in olive oil,” *J. Mater. Chem.*, vol. 16, no. 33, p. 3391, Aug. 2006.
- [60] C. Zhai, H. Zhang, N. Du, B. Chen, H. Huang, Y. Wu, and D. Yang, “One-Pot Synthesis of Biocompatible CdSe/CdS Quantum Dots and Their Applications as Fluorescent Biological Labels,” *Nanoscale Res. Lett.*, vol. 6, no. 1, p. 31, Sep. 2010.
- [61] S. Dayal, M. O. Reese, A. J. Ferguson, D. S. Ginley, G. Rumbles, and N. Kopidakis, “The Effect of Nanoparticle Shape on the Photocarrier Dynamics and Photovoltaic Device Performance of Poly(3-hexylthiophene):CdSe Nanoparticle Bulk Heterojunction Solar Cells,” *Adv. Funct. Mater.*, vol. 20, no. 16, pp. 2629–2635, Aug. 2010.
- [62] U. T. D. Thuy, N. Q. Liem, D. X. Thanh, M. Protière, and P. Reiss, “Optical transitions in polarized CdSe, CdSe/ZnSe, and CdSe/CdS/ZnS quantum dots dispersed in various polar solvents,” *Appl. Phys. Lett.*, vol. 91, no. 24, p. 241908, Dec. 2007.
- [63] V. Biju, Y. Makita, A. Sonoda, H. Yokoyama, Y. Baba, and M. Ishikawa, “Temperature-sensitive photoluminescence of CdSe quantum dot clusters,” *J. Phys.*

- Chem. B*, vol. 109, no. 29, pp. 13899–13905, 2005.
- [64] Y. Yin and A. P. Alivisatos, “Colloidal nanocrystal synthesis and the organic-inorganic interface,” *Nature*, vol. 437, no. 7059, pp. 664–670, 2005.
- [65] X. Chen, Y. Lou, A. C. Samia, and C. Burda, “Coherency strain effects on the optical response of core/shell heteronanostructures,” *Nano Lett.*, vol. 3, no. 6, pp. 799–803, 2003.
- [66] J. J. Li, Y. A. Wang, W. Guo, J. C. Keay, T. D. Mishima, M. B. Johnson, and X. Peng, “Large-scale synthesis of nearly monodisperse CdSe/CdS core/shell nanocrystals using air-stable reagents via successive ion layer adsorption and reaction.,” *J. Am. Chem. Soc.*, vol. 125, no. 41, pp. 12567–75, Oct. 2003.
- [67] Y.-J. Lee, Y.-C. Yao, M.-T. Tsai, A.-F. Liu, M.-D. Yang, and J.-T. Lai, “Current matching using CdSe quantum dots to enhance the power conversion efficiency of InGaP/GaAs/Ge tandem solar cells,” *Opt. Express*, vol. 21, no. S6, p. A953, 2013.
- [68] A. Issac, C. Von Borczyskowski, and F. Cichos, “Correlation between photoluminescence intermittency of CdSe quantum dots and self-trapped states in dielectric media,” *Phys. Rev. B - Condens. Matter Mater. Phys.*, vol. 71, no. 16, pp. 1–4, 2005.
- [69] A. B. Djurišić, Y. H. Leung, W. C. H. Choy, K. W. Cheah, and W. K. Chan, “Visible photoluminescence in ZnO tetrapod and multipod structures,” *Appl. Phys. Lett.*, vol. 84, no. 14, pp. 2635–2637, 2004.
- [70] H. M. Cheng, K. F. Lin, H. C. Hsu, and W. F. Hsieh, “Size dependence of photoluminescence and resonant Raman scattering from ZnO quantum dots,” *Appl. Phys. Lett.*, vol. 88, no. 26, 2006.
- [71] P. N. Prasad and D. J. Williams, “Introduction to Nonlinear Optical Effects in Molecules and Polymers,” *Wiley*, 1991.
- [72] R. W. Boyd, *Nonlinear Optics*, Third Edit. Academic Press, 2008.
- [73] R. H. Lipson and C. Lu, “Photonic crystals: a unique partnership between light and matter,” *Eur. J. Phys.*, vol. 30, pp. 33–48, 2009.
- [74] E. Yablonovitch, “Photonic Crystals: What ’ s in a Name?,” *Physical Review Letters*, no. March, pp. 12–13, 2007.
- [75] F. Koenderink, “Emission and Transport of Light in Photonic Crystals,” Universiteit van Amsterdam, 2003.
- [76] J. D. Joannopoulos and S. G. Johnson, *Photonic Crystals: Molding the Flow of Light*. Princeton University Press, 2008.
- [77] E. Yablonovitch, “Inhibited spontaneous emission in solid-state physics and electronics,” *Phys. Rev. Lett.*, vol. 58, no. 20, pp. 2059–2062, 1987.
- [78] S. John, “Strong localization of photons in certain disordered dielectric superlattices,”

- Phys. Rev. Lett.*, vol. 58, no. 23, pp. 2486–2489, 1987.
- [79] V. L. Welch and J.-P. Vigneron, “Beyond butterflies — the diversity of biological photonic crystals,” *Opt Quant Electron*, vol. 39, pp. 295–303, 2007.
- [80] R. D. Meade, K. D. Brommer, A. M. Rappe, and J. D. Joannopoulos, “Existence of a photonic band gap in two dimensions Existence of a photonic band gap in two dimensions,” *Appl. Phys. Lett.*, vol. 61, pp. 495–497, 2014.
- [81] K. M. Ho, C. T. Chan, And, and C. M. Soukoulis, “Existence of a photonic gap in periodic dielectric structures,” *Phys. Rev. Lett.*, vol. 65, no. 25, pp. 3152–3155, 1990.
- [82] E. Yablonovitch, T. J. Gmitter, and K. M. Leung, “Photonic Band Structure: The Face-Centered-Cubic Case Employing Nonspherical Atoms,” *Appl. Phys. Lett.*, vol. 67, no. 17, pp. 2295–2298, 1991.
- [83] C. C. Cheng, V. Arbet-Engels, A. Scherer, and E. Yablonovitch, “Nanofabricated three dimensional photonic crystals operating at optical wavelengths,” *Phys. Scr.*, vol. 68, pp. 17–20, 1996.
- [84] H. S. Sozuer and W. J. Haus, “Photonic bands : simple-cubic lattice,” *J. Opt. Soc. Am.*, vol. 10, no. 2, pp. 296–302, 1993.
- [85] C. . Chan, S. Datta, K. . Ho, and C. M. Soukoulis, “A7 structure: A family of photonic crystals,” *Phys. Rev. B*, vol. 50, no. 3, pp. 1988–1991, 1994.
- [86] R. B. and M. S. K.M. Ho, C.T Chan, C.M. Soukoulis, “Photonic band gaps in three dimensions:New layer-by-layer periodic structures,” *Solid state Commun. Commun.*, vol. 89, no. 5, pp. 413–416, 1994.
- [87] P. Taylor, H. S. Sözüer, and J. P. Dowling, “Photonic Band Calculations for Woodpile Structures,” *J. Mod. Opt.*, vol. 41, no. 2, pp. 231–239, 1994.
- [88] Z. Sekkat and S. Kawata, “Laser nanofabrication in photoresists and azopolymers,” *Laser Photon. Rev.*, vol. 8, no. 1, pp. 1–26, Jan. 2014.
- [89] S. Juodkasis, V. Mizeikis, and H. Misawa, “Three-dimensional microfabrication of materials by femtosecond lasers for photonics applications,” *J. Appl. Phys.*, vol. 106, no. 5, p. 051101, Sep. 2009.
- [90] S. Maruo and J. T. Fourkas, “Recent progress in multiphoton microfabrication,” *Laser Photonics Rev.*, vol. 2, no. 1–2, pp. 100–111, Apr. 2008.
- [91] M. Farsari, M. Vamvakaki, and B. N. Chichkov, “Multiphoton polymerization of hybrid materials,” *J. Opt.*, vol. 12, no. 12, p. 124001, Dec. 2010.
- [92] A. Rosspeintner, S. C. Ligon, T. Scherzer, W. Husinsky, N. Pucher, K. Cicha, R. Liska, J. Stampfl, A. Ajami, J. Torgersen, E. Vauthey, Z. Li, and S. Naumov, “A Straightforward Synthesis and Structure–Activity Relationship of Highly Efficient Initiators for Two-Photon Polymerization,” *Macromolecules*, vol. 46, no. 2, pp. 352–361, 2013.

- [93] S. M. Aliwi and C. H. Bamford, "Photoactive polymers containing vanadium: 1 . Preparation , characterization and photoreactions," *Polymer (Guildf)*., vol. 18, no. 4, pp. 375–380, 1977.
- [94] a. Ovsianikov, a. Gaidukeviciute, B. N. Chichkov, M. Oubaha, B. D. MacCraith, I. Sakellari, a. Giakoumaki, D. Gray, M. Vamvakaki, M. Farsari, and C. Fotakis, "Two-Photon Polymerization of Hybrid Sol-Gel Materials for Photonics Applications," *Laser Chem.*, vol. 2008, pp. 1–7, 2008.
- [95] N. Ozer, "Electrochemical properties of sol-gel deposited vanadium pentoxide films," *Thin Solid Films*, vol. 305, pp. 80–87, 1997.
- [96] U. Klett and J. Fricke, "Gelation of vanadium (V) oxide-triisopropoxide doped silica gels," *J. Non. Cryst. Solids*, vol. 238, pp. 45–50, 1998.
- [97] A. Dement and A. Jovai, "Pulse Shape Influence on the Accuracy of z-scan Measurments," *Nonlinear Anal. Model. Control*, vol. 10, no. 2, pp. 119–136, 2005.
- [98] M. Sheik-Bahae, "sensitive measurement of optical nonlinearities using a single beam," *J. Quantum Electron.*, vol. 26, no. 4, pp. 760–769, 1990.
- [99] S. M. Aliwi, A. W. Al-Shorachi, and B. Y. Al-Banna, "Photolysis of methoxo-oxobis (benzohydroxamato) vanadium (V) different organic solvents," *J. Photochem. Photobiol. A*, vol. 81, pp. 31–36, 1994.
- [100] S. M. Aliwi, A. W. Al-Shorachi, and B. Y. Al-Banna, "Photodecomposition of alkyloxo-oxobis(benzohydroxamato)-vanadium (V) in acetone solutions," *J. Photochem. Photobiol. A*, vol. 83, pp. 171–175, 1994.
- [101] J. Livage, "Sol-Gel chemistry and electrochemical properties of vanadium oxide gels," *Solid State Ionics*, vol. 86–88, pp. 935–942, 1996.
- [102] J. Livage, "Vanadium Pentoxide Gels," *Chem. Mater.*, vol. 3, no. 8, pp. 578–593, 1991.
- [103] L. Albaric, N. Hovnanian, A. Julbe, and G. Volle, "Oxovanadium (V) -1-methoxy-2-propanoxide : synthesis and spectroscopic studies — a molecular precursor for a vanadium – magnesium oxide catalyst," *Polyhedron*, vol. 20, pp. 2261–2268, 2001.
- [104] K. M. Ho, C. . Chan, C. M. Soukoulis, R. Biswas, and M. Sigalas, "Photonic Band Gaps in Three Dimensions: New Layer-by-layer Periodic Structures," *Solid State Commun.*, vol. 89, no. 5, pp. 413–416, 1994.
- [105] J. Fischer and M. Wegener, "Three-dimensional direct laser writing inspired by stimulated-emission-depletion microscopy," *Opt. Mater. Express*, vol. 1, no. 4, pp. 2363–2366, 2011.
- [106] N. Vasilantonakis, K. Terzaki, I. Sakellari, V. Purlys, D. Gray, C. M. Soukoulis, M. Vamvakaki, M. Kafesaki, and M. Farsari, "Three-Dimensional Metallic Photonic Crystals with Optical Bandgaps," *Adv. Mater.*, vol. 24, no. 8, pp. 1101–1105, Feb. 2012.
- [107] M. Malinauskas, A. Zukauskas, R. Gadonas, and S. Juodkazis, "Mechanisms of three-

- dimensional structuring of photo-polymers by tightly focussed femtosecond laser pulses,” vol. 18, no. 10, pp. 910–913, 2010.
- [108] M. Sheik-Bahae, A. A. Said, T. H. Wei, D. J. Hagan, and E. W. Van Stryland, “Sensitive Measurement of Optical Nonlinearities Using a Single Beam,” *IEEE J. Quantum Electron.*, vol. 26, no. 4, pp. 760–769, 1990.
- [109] B. Gu, X.-Q. Huang, S.-Q. Tan, M. Wang, and W. Ji, “Z-scan analytical theories for characterizing multiphoton absorbers,” *Appl. Phys. B*, vol. 95, no. 2, pp. 375–381, May 2009.
- [110] A. O. Z. Li, A. A. J. Torgersen, and W. H. J. S. R. Liska, “3D grafting via three-photon induced photolysis of aromatic azides,” pp. 29–34, 2012.
- [111] Z. Suo, M. Drobizhev, C. W. Spangler, N. Christensson, and A. Rebane, “New Fluorophores Based on Trifluorenylamine with Very Large Intrinsic Three-Photon Absorption Cross Sections,” *Org. Lett.*, vol. 07, no. 22, pp. 4807–4010, 2005.
- [112] F. E. Hern, K. D. Belfield, and I. Cohanoschi, “Three-photon absorption enhancement in a symmetrical charge transfer fluorene derivative,” *Chem. Phys. Lett.*, vol. 391, pp. 22–26, 2004.
- [113] J. Liu, G. Li, and Y. Wang, “Impact of Electron Acceptor on Three-Photon Absorption Cross- Section of the Fluorene Derivatives,” *J. Phys. Chem. A*, vol. 116, pp. 7445–7451, 2012.
- [114] C. Zhan, D. Li, D. Zhang, and Y. Li, “Three-photon absorption from six stilbazolium derivatives : application for optical limiting,” *Chem. Phys. Lett.*, vol. 353, pp. 138–142, 2002.
- [115] A. Ovsianikov, J. Viertl, B. Chichkov, M. Oubaha, B. MacCraith, I. Sakellari, A. Giakoumaki, D. Gray, M. Vamvakaki, M. Farsari, and C. Fotakis, “Ultra-low shrinkage hybrid photosensitive material for two-photon polymerization microfabrication,” *ACS Nano*, vol. 2, no. 11, pp. 2257–2262, 2008.
- [116] M. Malinauskas, V. Purlys, M. Rutkauskas, A. Gaidukevičiūtė, and R. Gadonas, “Femtosecond visible light induced two-photon photopolymerization for 3D micro/nanostructuring in photoresists and photopolymers,” *Lith. J. Phys.*, vol. 50, no. 2, Apr. 2010.
- [117] P. Prabhakaran, W. J. Kim, K.-S. Lee, and P. N. Prasad, “Quantum dots (QDs) for photonic applications,” *Opt. Mater. Express*, vol. 2, no. 5, pp. 578–593, May 2012.
- [118] J. C. Norman, D. Jung, Y. Wan, and J. E. Bowers, “Perspective: The future of quantum dot photonic integrated circuits,” *APL Photonics*, vol. 3, no. 3, p. 030901, Mar. 2018.
- [119] T. Rath and G. Trimmel, “In situ syntheses of semiconducting nanoparticles in conjugated polymer matrices and their application in photovoltaics,” *Hybrid Mater.*, vol. 1, no. 1, p. 15, Jan. 2014.

- [120] H. Kim, S. Beack, S. Han, M. Shin, T. Lee, Y. Park, K. S. Kim, A. K. Yetisen, S. H. Yun, W. Kwon, and S. K. Hahn, “Multifunctional Photonic Nanomaterials for Diagnostic, Therapeutic, and Theranostic Applications,” *Adv. Mater.*, vol. 30, no. 10, pp. 1–33, 2018.
- [121] P. Lodahl, S. Mahmoodian, and S. Stobbe, “Interfacing single photons and single quantum dots with photonic nanostructures,” *Reviews of Modern Physics*, vol. 87, no. 2, pp. 347–400, 2015.
- [122] L. Banyai, Y. Z. Hu, M. Lindberg, and S. W. Koch, “Third-order optical nonlinearities in semiconductor microstructures,” *Phys. Rev. B*, vol. 38, no. 12, pp. 8142–8153, Oct. 1988.
- [123] E. Yablonovitch and T. J. Gmitter, “Photonic band structure: the face-centered-cubic case,” *J. Opt. Soc. Am. A*, vol. 7, no. 9, p. 1792, Sep. 1990.
- [124] S. Bin Hasan, A. P. Mosk, W. L. Vos, and A. Lagendijk, “Finite-size Scaling of the Density of States in Photonic Band Gap Crystals,” *Phys. Rev. Lett.*, vol. 120, no. 23, p. 237402, Jun. 2018.
- [125] C. López, “Three-dimensional photonic bandgap materials: semiconductors for light,” *J. Opt. A Pure Appl. Opt.*, vol. 8, no. 5, pp. R1–R14, May 2006.
- [126] S. C. Padmanabhan, K. Linehan, S. O’Brien, S. Kassim, H. Doyle, I. M. Povey, M. Schmidt, and M. E. Pemble, “A bottom-up fabrication method for the production of visible light active photonic crystals,” *J. Mater. Chem. C*, vol. 2, no. 9, pp. 1675–1682, Feb. 2014.
- [127] P. Lodahl, A. Floris van Driel, I. S. Nikolaev, A. Irman, K. Overgaag, D. Vanmaekelbergh, and W. L. Vos, “Controlling the dynamics of spontaneous emission from quantum dots by photonic crystals,” *Nature*, vol. 430, no. 7000, pp. 654–657, Aug. 2004.
- [128] J. Li, B. Jia, G. Zhou, C. Bullen, J. Serbin, and M. Gu, “Spectral Redistribution in Spontaneous Emission from Quantum-Dot-Infiltrated 3D Woodpile Photonic Crystals for Telecommunications,” *Adv. Mater.*, vol. 19, no. 20, pp. 3276–3280, Sep. 2007.
- [129] M. Qi, E. Lidorikis, P. T. Rakich, S. G. Johnson, J. D. Joannopoulos, E. P. Ippen, and H. I. Smith, “A three-dimensional optical photonic crystal with designed point defects,” *Nature*, vol. 429, no. 6991, pp. 538–542, Jun. 2004.
- [130] J. Stampfl, R. Liska, and A. Ovsianikov, *Multiphoton lithography: techniques, materials and applications*. .
- [131] I. Sakellari, E. Kabouraki, D. Gray, V. Purlys, C. Fotakis, A. Pikulin, N. Bityurin, M. Vamvakaki, and M. Farsari, “Diffusion-Assisted High-Resolution Direct Femtosecond Laser Writing,” *ACS Nano*, vol. 6, no. 3, pp. 2302–2311, 2012.
- [132] J. Fischer and M. Wegener, “Three-dimensional direct laser writing inspired by

- stimulated-emission-depletion microscopy,” vol. 1, no. 4, pp. 2363–2366, 2011.
- [133] J. Fischer and M. Wegener, “Three-dimensional optical laser lithography beyond the diffraction limit,” *Laser and Photonics Reviews*, vol. 7, no. 1, pp. 22–44, 2013.
- [134] R. Krini, C. W. Ha, P. Prabhakaran, H. El Mard, D.-Y. Yang, R. Zentel, and K.-S. Lee, “Photosensitive Functionalized Surface-Modified Quantum Dots for Polymeric Structures via Two-Photon-Initiated Polymerization Technique,” *Macromol. Rapid Commun.*, vol. 36, no. 11, pp. 1108–1114, Jun. 2015.
- [135] D. Buso, E. Nicoletti, J. Li, and M. Gu, “Engineering the refractive index of three-dimensional photonic crystals through multilayer deposition of CdS films,” *Opt. Express*, vol. 18, no. 2, p. 1033, Jan. 2010.
- [136] D.-X. Lu, Y.-L. Zhang, D.-D. Han, H. Wang, H. Xia, Q.-D. Chen, H. Ding, and H.-B. Sun, “Solvent-tunable PDMS microlens fabricated by femtosecond laser direct writing,” *J. Mater. Chem. C*, vol. 3, no. 8, pp. 1751–1756, Feb. 2015.
- [137] M. J. Ventura, C. Bullen, and M. Gu, “Direct laser writing of three-dimensional photonic crystal lattices within a PbS quantum-dot-doped polymer material,” *Opt. Express*, vol. 15, no. 4, p. 1817, Feb. 2007.
- [138] K. K. Jang, P. Prabhakaran, D. Chandran, J.-J. Park, and K.-S. Lee, “Solution processable and photopatternable blue, green and red quantum dots suitable for full color displays devices,” *Opt. Mater. Express*, vol. 2, no. 5, p. 519, May 2012.
- [139] J. Zha and H. Roggendorf, *Sol-gel science, the physics and chemistry of sol-gel processing*, Ed. by C. J. Brinker and G. W. Scherer, Academic Press, Boston 1990, xiv, 908 pp., bound?ISBN 0-12-134970-5, vol. 3, no. 10. WILEY-VCH Verlag GmbH, 1991.
- [140] I. Sakellari, a. Gaidukeviciute, a. Giakoumaki, D. Gray, C. Fotakis, M. Farsari, M. Vamvakaki, C. Reinhardt, a. Ovsianikov, and B. N. Chichkov, “Two-photon polymerization of titanium-containing sol-gel composites for three-dimensional structure fabrication,” *Appl. Phys. A*, vol. 100, no. 2, pp. 359–364, Jul. 2010.
- [141] Z.-B. Sun, X.-Z. Dong, S. Nakanishi, W.-Q. Chen, X.-M. Duan, and S. Kawata, “Log-pile photonic crystal of CdS-polymer nanocomposites fabricated by combination of two-photon polymerization and in situ synthesis,” *Appl. Phys. A*, vol. 86, no. 4, pp. 427–431, Jan. 2007.
- [142] R. R. Alfano and S. L. Shapiro, “Observation of self-phase modulation and small-scale filaments in crystals and glasses,” *Phys. Rev. Lett.*, vol. 24, no. 11, pp. 592–594, 1970.
- [143] R. R. Alfano, *The supercontinuum laser source (Second Edition): Fundamentals with updated references*, Springer., vol. 53, no. 9. Heidelberg, 2006.
- [144] Claude Rullière, *Femtosecond Laser Pulses*. New York, NY: Springer New York, 2005.
- [145] A. Maciejewski, R. Naskrecki, M. Lorenc, M. Ziolk, J. Karolczak, J. Kubicki, M. Matysiak, and M. Szymanski, “Transient absorption experimental set-up with

- femtosecond time resolution. Femto- and picosecond study of DCM molecule in cyclohexane and methanol solution,” *J. Mol. Struct.*, vol. 555, pp. 1–13, 2000.
- [146] S. Johnson and J. Joannopoulos, “Block-iterative frequency-domain methods for Maxwell’s equations in a planewave basis,” *Opt. Express*, vol. 8, no. 3, p. 173, 2001.
- [147] M. N. Kalasad, M. K. Rabinal, B. G. Mulimani, and G. S. Avadhani, “Temporal evolution of capped cadmium sulfide nanoparticles,” *Semicond. Sci. Technol.*, vol. 23, no. 4, p. 045009, Apr. 2008.
- [148] V. Q. Lam, S. Turrell, A. Martucci, M. Bouazaoui, and B. Capoen, “Synthesis and optical properties of MPTMS-capped CdS quantum dots embedded in TiO₂ thin films for photonic applications,” *J. Non. Cryst. Solids*, vol. 352, no. 30–31, pp. 3315–3319, 2006.
- [149] Y. Lin, J. Zhang, E. Kumacheva, and E. H. Sargent, “Third-order optical nonlinearity and figure of merit of CdS nanocrystals chemically stabilized in spin-processable polymeric films,” *J. Mater. Sci.*, vol. 39, no. 3, pp. 993–996, 2004.
- [150] M. Deubel, G. Von Freymann, M. Wegener, S. Pereira, K. Busch, and C. M. Soukoulis, “Direct laser writing of three-dimensional photonic-crystal templates for telecommunications,” *Nat. Mater.*, vol. 3, no. 7, pp. 444–447, 2004.
- [151] I. Staude, M. Thiel, S. Essig, C. Wolff, K. Busch, G. von Freymann, and M. Wegener, “Fabrication and characterization of silicon woodpile photonic crystals with a complete bandgap at telecom wavelengths,” *Opt. Lett.*, vol. 35, no. 7, pp. 1094–6, 2010.
- [152] C. Rullière, *Femtosecond Laser Pulses*. New York: Springer, 2005.
- [153] P. M. Johnson, A. F. Koenderink, and W. L. Vos, “Ultrafast switching of photonic density of states in photonic crystals,” *Phys. Rev. B - Condens. Matter Mater. Phys.*, vol. 66, no. 8, pp. 1–4, 2002.
- [154] P. Horodyská, P. Němec, D. Sprinzl, P. Malý, V. N. Gladilin, and J. T. Devreese, “Exciton spin dynamics in spherical CdS quantum dots,” *Phys. Rev. B - Condens. Matter Mater. Phys.*, vol. 81, no. 4, p. 045301, 2010.
- [155] M. Shui, X. Jin, Z. Li, J. Yang, G. Shi, Z. Nie, X. Wu, Y. Wang, K. Yang, X. Zhang, and Y. Song, “Investigation of nonlinear dynamics in CdS by time-resolved nondegenerate pump–probe system with phase object,” *J. Mod. Opt.*, vol. 58, no. 11, pp. 973–977, Jun. 2011.
- [156] V. I. Klimov, D. W. McBranch, C. A. Leatherdale, and M. G. Bawendi, “Electron and hole relaxation pathways in semiconductor quantum dots,” *Phys. Rev. B*, vol. 60, no. 19, pp. 13740–13749, Nov. 1999.
- [157] P. Tran, “Photonic-band-structure calculation of material possessing Kerr nonlinearity,” *Phys. Rev. B*, vol. 52, no. 15, pp. 10673–10676, 1995.
- [158] V. Lousse and J. P. Vigneron, “Self-consistent photonic band structure of dielectric

- superlattices containing nonlinear optical materials,” *Phys. Rev. E*, vol. 63, no. 2, p. 027602, 2001.
- [159] A. Huttunen and P. Törmä, “Band structures for nonlinear photonic crystals,” *J. Appl. Phys.*, vol. 91, no. 7, pp. 3988–3991, 2002.
- [160] T. G. Euser, A. J. Molenaar, J. G. Fleming, B. Gralak, A. Polman, and W. L. Vos, “All-optical octave-broad ultrafast switching of Si woodpile photonic band gap crystals,” *Phys. Rev. B*, vol. 77, no. 11, p. 115214, Mar. 2008.
- [161] Y. Liu, F. Qin, Z.-Y. Wei, Q.-B. Meng, D.-Z. Zhang, and Z.-Y. Li, “10 fs ultrafast all-optical switching in polystyrene nonlinear photonic crystals,” *Appl. Phys. Lett.*, vol. 95, no. 13, p. 131116, Sep. 2009.
- [162] P. J. Harding, T. G. Euser, and W. L. Vos, “Identification of competing ultrafast all-optical switching mechanisms in Si woodpile photonic crystals,” *J. Opt. Soc. Am. B*, vol. 26, no. 4, p. 610, Apr. 2009.
- [163] K. Hirose, Y. Liang, Y. Kurosaka, A. Watanabe, T. Sugiyama, and S. Noda, “Watt-class high-power, high-beam-quality photonic-crystal lasers,” *Nat. Photonics*, vol. 8, no. 5, pp. 406–411, 2014.
- [164] N. V. Triviño, R. Butté, J. F. Carlin, and N. Grandjean, “Continuous wave blue lasing in iii-nitride nanobeam cavity on silicon,” *Nano Lett.*, vol. 15, no. 2, pp. 1259–1263, 2015.
- [165] K. Hennessy, A. Badolato, M. Winger, D. Gerace, M. Atat Uuml Re, S. Gulde, S. F Auml Lt, E. L. Hu, and A. Imamo Gbreve Lu, “Quantum nature of a strongly coupled single quantum dot[cavity] system,” *Nature*, vol. 445, no. 7130, p. 896, 2007.
- [166] H. Altug, D. Englund, and J. Vučković, “Ultrafast photonic crystal nanocavity laser,” *Nat. Phys.*, vol. 2, no. 7, pp. 484–488, 2006.
- [167] M. H. Song, B. Park, S. Nishimura, T. Toyooka, I. J. Chung, Y. Takanishi, K. Ishikawa, and H. Takezoe, “Electrotunable non-reciprocal laser emission from a liquid-crystal photonic device,” *Adv. Funct. Mater.*, vol. 16, no. 14, pp. 1793–1798, 2006.
- [168] A. C. Scofield, S.-H. Kim, J. N. Shapiro, A. Lin, B. Liang, A. Scherer, and D. L. Huffaker, “Bottom-up photonic crystal lasers.,” *Nano Lett.*, vol. 11, no. 12, pp. 5387–5390, 2011.
- [169] S. H. Kwon, H. Y. Ryu, G. H. Kim, Y. H. Lee, and S. B. Kim, “Photonic bandedge lasers in two-dimensional square-lattice photonic crystal slabs,” *Appl. Phys. Lett.*, vol. 83, no. 19, pp. 3870–3872, 2003.
- [170] S. Kim, S. Yoon, H. Seok, J. Lee, and H. Jeon, “Band-edge lasers based on randomly mixed photonic crystals.,” *Opt. Express*, vol. 18, no. 8, pp. 7685–7692, 2010.
- [171] V. Reboud, J. Romero-Vivas, P. Lovera, N. Kehagias, T. Kehoe, G. Redmond, and C. M. Sotomayor Torres, “Lasing in nanoimprinted two-dimensional photonic crystal

- band-edge lasers,” *Appl. Phys. Lett.*, vol. 102, no. 7, 2013.
- [172] M. Lončar, T. Yoshie, A. Scherer, P. Gogna, and Y. Qiu, “Low-threshold photonic crystal laser,” *Appl. Phys. Lett.*, vol. 81, no. 15, pp. 2680–2682, 2002.
- [173] W. Cao, A. Muñoz, P. Palffy-Muhoray, and B. Taheri, “Lasing in a three-dimensional photonic crystal of the liquid crystal blue phase II,” *Nat. Mater.*, vol. 1, no. 2, pp. 111–113, 2002.
- [174] H. Yamada, T. Nakamura, Y. Yamada, and K. Yano, “Colloidal-crystal laser using monodispersed mesoporous silica spheres,” *Adv. Mater.*, vol. 21, no. 41, pp. 4134–4138, 2009.
- [175] K. Yoshino, S. Tatsuhara, Y. Kawagishi, M. Ozaki, a. a. Zakhidov, and Z. V. Vardeny, “Amplified spontaneous emission and lasing in conducting polymers and fluorescent dyes in opals as photonic crystals,” *Appl. Phys. Lett.*, vol. 74, no. 18, pp. 2590–2592, 1999.
- [176] M. N. Shkunov, Z. V. Vardeny, M. C. DeLong, R. C. Polson, A. A. Zakhidov, and R. H. Baughman, “Tunable, gap-state lasing in switchable directions for opal photonic crystals,” *Adv. Funct. Mater.*, vol. 12, no. 1, pp. 21–26, 2002.
- [177] L. K. Teh, C. C. Wong, H. Y. Yang, S. P. Lau, and S. F. Yu, “Lasing in electrodeposited ZnO inverse opal,” *Appl. Phys. Lett.*, vol. 91, no. 16, pp. 89–92, 2007.
- [178] F. Jin, L. Shi, M. Zheng, X. Dong, S. Chen, Z. Zhao, and X. Duan, “Lasing and Amplified Spontaneous Emission in a Polymeric Inverse Opal Photonic Crystal Resonating Cavity,” 2013.
- [179] “Seeking the Ultimate Nanolaser,” *Science (80-.)*, vol. 314, no. October, pp. 260–261, 2006.
- [180] A. Tandraechanurat, S. Ishida, D. Guimard, M. Nomura, S. Iwamoto, and Y. Arakawa, “Lasing oscillation in a three-dimensional photonic crystal nanocavity with a complete bandgap,” *Nat. Photonics*, vol. 5, no. 2, pp. 91–94, 2011.
- [181] W. W. Yu and X. Peng, “Formation of High-Quality CdS and Other II-VI Semiconductor Nanocrystals in Noncoordinating Solvents: Tunable Reactivity of Monomers,” *Angew. Chemie Int. Ed.*, vol. 41, no. 13, pp. 2368–2371, Jul. 2002.
- [182] Xiaogang Peng, Michael C. Schlamp, A. Andreas V. Kadavanich, and A. P. Alivisatos*, “Epitaxial Growth of Highly Luminescent CdSe/CdS Core/Shell Nanocrystals with Photostability and Electronic Accessibility,” *J. Am. Chem. Soc.*, vol. 119, no. 30, pp. 7019–7029, 1997.
- [183] W. W. Yu, L. Qu, W. Guo, and X. Peng, “Experimental Determination of the Extinction Coefficient of CdTe, CdSe, and CdS Nanocrystals,” vol. 125, no. 17, pp. 2854–2860, 2003.
- [184] I. Paradisanos, S. Germanis, N. T. Pelekanos, C. Fotakis, E. Kymakis, G. Kioseoglou,

- and E. Stratakis, “Room temperature observation of biexcitons in exfoliated WS₂ monolayers,” *Appl. Phys. Lett.*, vol. 110, no. 19, p. 193102, May 2017.
- [185] B. O. Dabbousi, F. V Mikulec, J. R. Heine, H. Mattoussi, R. Ober, K. F. Jensen, and M. G. Bawendi, “(CdSe) ZnS Core-Shell Quantum Dots : Synthesis and Characterization of a Size Series of Highly Luminescent Nanocrystallites,” vol. 9463, no. 97, pp. 9463–9475, 1997.
- [186] R. Xie, U. Kolb, J. Li, T. Basche, and A. Mews, “Synthesis and Characterization of Highly Luminescent CdSe-Core CdS/Zn 0.5 Cd 0.5 S/ZnS Multishell Nanocrystals,” *J. Am. Chem. Soc. Soc.*, vol. 127, no. 24, pp. 7480–7488, 2005.
- [187] H. Chang, K. Min, M. Lee, M. Kang, Y. Park, K. S. Cho, Y. G. Roh, S. Woo Hwang, and H. Jeon, “Colloidal quantum dot lasers built on a passive two-dimensional photonic crystal backbone,” *Nanoscale*, vol. 8, no. 12, pp. 6571–6576, 2016.
- [188] F. Raineri, A. M. Yacomotti, T. J. Karle, R. Hostein, R. Braive, A. Beveratos, I. Sagnes, and R. Raj, “Dynamics of band-edge photonic crystal lasers,” *Opt. Express*, vol. 17, no. 5, p. 3165, 2009.
- [189] H. Y. Lin, H. K. Fu, C. L. Cheng, Y. F. Chen, Y. S. Lin, Y. Hung, and C. Y. Mou, “Laser action in Tb(OH)₃/SiO₂ photonic crystals,” *Opt. Express*, vol. 16, no. 21, p. 16697, 2008.
- [190] E. N. Bodunov and A. L. Simões Gamboa, “Kinetics of Photoluminescence Decay of Colloidal Quantum Dots: Nonexponential Behavior and Detrapping of Charge Carriers,” *J. Phys. Chem. C*, vol. 122, no. 19, pp. 10637–10642, 2018.

Aknowledgements

Reaching the end, I would like to go back, to first page of this thesis where my name stands alone. From my point of view, the work presented in this thesis is not only mine, because nothing of these would have been realized without the contribution of a number of people. First of all I would like to thank my supervisors Prof. Maria Vamvakaki and Dr. Maria Farari, not only for their scientific guidance but also for standing by me ethically and emotionally. They were not just my supervisors but mentors for me and I feel very happy being part of their team.

Next, I would like to thank Dr. Ioanna Sakellari and Dr. Sotiris Droulias for the scientific guidance throughout my thesis. I would like also to thank Dr. Theodore Manouras for the fruitfull discussions we had all these years.

I would also like to thank my partener in life Dr. Elefterios Koufakis for standing next to me in our common route in obtaining our PhD titles and my family and friends for their emotional support.

Last but not least, I would like to thank my four leged family members, Tsitsi and Richard for filling my after work hours with joy!!